Impact of Distributed Battery Energy Storage on Electric Power Transmission and Distribution Systems

by

Fabian Calero

A thesis
presented to the University of Waterloo
in fulfillment of the
thesis requirement for the degree of
Doctor of Philosophy
in
Electrical and Computer Engineering

Waterloo, Ontario, Canada, 2021

Examining Committee Membership

The following served on the Examining Committee for this thesis. The decision of the Examining Committee is by majority vote.

Supervisor:	Claudio Canizares Professor, Department of Electrical and Computer Engineering, University of Waterloo
Co-Supervisor:	Kankar Bhattacharya Professor, Department of Electrical and Computer Engineering, University of Waterloo
Internal Member:	Mehrdad Kazerani Professor, Department of Electrical and Computer Engineering, University of Waterloo
Internal Member:	Mohamed Ahmed Adjunct Assistant Professor, Department of Electrical and Computer Engineering, University of Waterloo
Internal-External Member:	Michael Fowler Professor, Department of Chemical Engineering, University of Waterloo
External Examiner:	Jovica Milanovic Professor, Department of Electrical and Electronic Engineering, University of Manchester

Author's Declaration

I hereby declare that I am the sole author of this thesis. This is a true copy of the thesis, including any required final revisions, as accepted by my examiners.

I understand that my thesis may be made electronically available to the public.

Abstract

The penetration of Renewable Energy Sources (RES) in electricity grids has increased worldwide over the past decade because of their decreasing costs, especially of Photovoltaic (PV) and wind generation resources with government support for their deployment to counteract global warming effects. Indeed, nowadays, not only utility-scale, but small-scale RES connected at the distribution level are being installed by residential and industrial customers to improve their energy supply and costs. In this context, Energy Storage Systems (ESSs) can be used to facilitate the integration of RES into the grid; Battery Energy Storage Systems (BESSs) being a relatively matured and suitable storage technology for such applications. In particular, distribution systems in some jurisdictions are experiencing an increasing number of new installations of Distributed Energy Resources (DERs), including PV generation accompanied by BESSs, thus, transforming the traditionally passive utility grids into Active Distribution Networks (ADNs), whose operation has the potential to influence the transmission system upstream. Some issues associated with large quantities of DERs connected to ADNs are reduction of transmission level flexibility to accommodate changes at the distribution system, larger frequency deviations due to reduction of system inertia, and various other grid stability issues associated with DER converter interfaces. BESSs can help address some of these problems by providing grid services such as voltage control, oscillation damping, frequency regulation, and active and reactive power control. As a result, appropriate assessment of the integration of DERs on transmission grids, particularly BESSs, is necessary. In this thesis, the impacts of grid-scale and distributed BESSs connected at the distribution system level, on the transmission grid are studied, for which suitable models for steady-state and dynamic analyses are proposed. Thus, first, a dynamic average BESS model is proposed, which comprises a simplified representation of the battery cells to allow simulating the effects of battery degradation, a bidirectional buck-boost converter (dc-to-dc), a Voltage Source Converter (VSC), an ac filter, and associated controls. The decoupled dq-current control of the VSC enables independent control of the BESSs' active and reactive power injections, thus allowing their operation in several modes studied and improved in this work, namely, constant active and reactive power, constant power factor, voltage regulation, frequency regulation, oscillation damping, and a combination of the last two. The BESS average model is included within a commercial-grade software for power system analysis, validated against a detailed model that considers the high-frequency switching in the converters, and tested for different contingencies when connected to a benchmark system to demonstrate the effectiveness of a grid-scale BESS to provide the services stated earlier. In the second part of the thesis, in order to investigate the effects of distributed BESSs connected to ADNs, on the transmission grid, for dynamic electrical studies, an aggregated black-box BESS model

at the boundary bus of the transmission and ADN is proposed. ADN measurements of the aggregated response of the BESSs at the boundary bus with the transmission system are used to develop the aggregated black-box model, which is based on two Neural Networks (NNs), one for active power and the other for reactive power, with their optimal topology obtained using a Genetic Algorithm (GA). Detailed simulations are performed considering multiple BESSs connected to a CIGRE benchmark and located at a load bus of the 9-bus WSCC benchmark transmission network to generate training data for the NNs. Then, the test ADN is replaced by the proposed black-box model, with aggregated models of the loads and PV generation, demonstrating that the model can accurately reproduce the results obtained for trained and untrained events. The main conclusions of this work are that the inclusion of the proposed controllers for the BESS can significantly improve the contribution of both grid-scale and distribute BESSs to the stability of transmission grids. In addition, the need of including the dc-to-dc converter in the BESS model for dynamic studies is demonstrated, especially when degraded batteries are considered, due to the limitations this operating condition creates on the dc-to-dc operation and its associated controller. Finally, the proposed methodology used to develop the black-box model to represent the aggregated response of BEESs is proved to be robust, since this model is shown to accurately reproduce the behavior the aggregated response of the battery systems providing various grid services, not only for the events and associated data used to train the proposed NN-based models, but also for contingencies for which the models were not trained.

Acknowledgements

First of all, I would like to thank God for allowing me to carry out my doctoral studies in this prestigious university, for putting wonderful people in my path during these years, and for being my support when I needed it the most.

I would like to extend my deepest gratitude to Prof. Claudio Canizares and Prof. Kankar Bhattacharya for their extraordinary guidance and support during my doctoral studies at the University of Waterloo. It has been an honour for me to work under their supervision. They are and will always be referents of excellence, responsibility, hard work, and extraordinary values as human beings.

I want to thank my Ph.D. Committee members for their valuable comments and observations: Professor Mehrdad Kazerani and Dr. Mohamed Ahmed, from the Department of Electrical and Computer Engineering at University of Waterloo; Professor Michael Fowler, from the Department of Chemical Engineering at the University of Waterloo; and Professor Jovica Milanovich, from the Department of Electrical and Electronic Engineering at the University of Manchester.

My sincere thanks to my friends from the EMSOL lab: Amir, Baheej, Behnam, Bharat, Carlos, Chioma, Dario, Dante, David, Edson, Emin, Enrique, Fabricio, Hisham, Indrajit, Jean-Michell, Mauricio, Mariano, Matheus, Mostafa, Nafeesa, Nitin, Omar, Samuel, Sofia, Talal, and William. The moments shared during these years will be very valuable for me.

I am extremely grateful to my father Fabian, my mother Gladys, my sister Diana for their continuous encouragement, unparalleled love, help and support; and I would like to specially thank my brother Ivan, with whom I'm deeply indebted for his unconditional help and support during hard times. Finally, I am deeply grateful to the love of my life Romina for simply existing and being the best of my life.

I sincerely acknowledge the funding and support provided by the SENESCYT in Ecuador, the Canadian Natural Sciences and Engineering Research Council (NSERC), and the NSERC Energy Storage Technology (NEST) Network. I am also grateful to the Wind Energy Institute of Canada (WEICan) for hosting me and providing information for this work.

Dedication

To God, who deserves all the honor and glory forever and ever.

Table of Contents

List of Figures

List of Tables

List of Acronyms

ADN	Active Distribution Network
AGC	Automatic Generation Control
AI	Artificial Intelligence
BESS	Battery Energy Storage System
CAES	Compressed Air Energy Storage
DAE	Differential-algebraic Equations
DER	Distributed Energy Resource
DG	Distributed Generation
EMT	Electromagnetic Transient
ESS	Energy Storage System
FES	Flywheel Energy Storage
GA	Genetic Algorithm
HVDC	High Voltage Direct Current
IESO	Independent Electricity System Operator
IGBT	Insulated-gate Bipolar Transistor

ISO	Independent System Operator
MRG	Modularized Renewable Generator
MSE	Mean Squared Error
NARX	Nonlinear Autoregressive Exogenous
NN	Neural Network
OD	Oscillation Damping
ODE	Ordinary Differential Equations
PC	Constant Active Power
PCC	Point of Common Coupling
PFR	Primary Frequency Regulation
PHS	Pumped Hdyro Storage
PI	Proportional Integral
PLL	Phase-Locked Loop
POD	Power Oscillation Damping
PSS	Power System Stabilizer
PV	Photovoltaic
PWM	Pulse Width Modulation
RES	Renewable Energy System
RNN	Recurrent Neural Network
SC	Super Capacitor
SFR	Secondary Frequency Regulation
SMES	Super Conducting Magnetic Energy Storage
SoC	State of Charge
STATCOM	Static Synchronous Compensator

TES	Thermal Energy Storage
UDM	User Defined Model
VR	Voltage Regulation
VSC	Voltage Source Converter
WECC	Western Electricity Coordinating Council
WSCC	Western Electricity Coordinating Council

Nomenclature

Parameters

α	P load model exponent
β	Q load model exponent
$\boldsymbol{N}$	Vector of number of neurons per hidden layer
$\boldsymbol{N}_{\max}$	Vector of maximum number of neurons per hidden layer
$\boldsymbol{w}$	Vector of internal weights of the NN
$\mathscr{L}$	Number of time series used to train the BESS black-box model
ρ	Parameter that defines the level of white noise added to variable [p.u.]
C	Capacitance [F]
C_1, C_2	Dc-to-dc converter capacitors [F]
db_P, db_Q	Dead-band for frequency and voltage controllers
dP	Rate of change limit for active power
FL	Flags to set control modes
H	Inertia constant [s]
K_D	Steady-state frequency droop constant

K_{I_1}, K_{P_1} PI control gains of current limiter control

K_{I_2}, K_{P_2} PI control gains of duty-cycle control

K_{I_d}, K_{P_d} PI control gains of current control in d axis

K_{I_F}, K_{P_F} PI control gains for frequency control

$K_{I_{PLL}}$, $K_{P_{PLL}}$ PI control gains of PLL

K_{I_q}, K_{P_q} PI control gains of current control in q axis

$K_{I_{VR}}$, $K_{P_{VR}}$ PI control gains of voltage regulator

K_{Ipl}, K_{Ppl} PI control gains of PLL circuit

K_{osc} Oscillation damping gain

K_{SoC} SoC gain for energy integration [kWh]

K_w, T_w Washout filter gain and time constant in P control

L Dc-to-dc converter inductor [H]

M Total number of data points k per series

M_c Number of dc-to-dc converters in parallel per VSC

N_c Number of VSCs in parallel in a BESS

n_x Number of input past information used in NARX NN

n_y Number of output past information used in NARX NN

R Resistance [Ω]

R_{bat} Equivalent internal resistance of a battery bank [Ω]

R_f, L_f Resistance and inductance of filter and transformer [mΩ, mH]

S	Nominal apparent power of individual BESS [VA]
SoC	State of charge [kWh]
T_{L_1}, T_{L_2}	Time constant for POB lead block [s]
T_{LG_1}, T_{LG_2}	Time constant for POB lag block [s]
T_{lpf}	Time constant for V_{dc} filter [s]
T_P, T_{RF}	Time constant for measurement filters [s]
T_{RV}	Time constant for measurement filters [s]
T_s	Dc-to-dc converter switching period [s]
V_{bat}	Equivalent internal voltage of a battery bank [V]
V_{bat}, R_{bat}	Equivalent battery bank voltage and resistance [V, Ω]
V_{dc_b}	DC link nominal voltage [V]
V_{nom}	Terminal ac nominal voltage [V]
w	Neural Network weights
X	Number of hidden layers
X	Reactance [Ω]
X_T	Transformer Reactance [Ω]

Variables

$\boldsymbol{\varphi}$	Vector of nonlinear functions representing the right-hand side of differential equations
$\boldsymbol{\vartheta}$	Vector of nonlinear functions representing the right-hand side of algebraic equations

μ	Random variable modeled as uniformly distributed process
ω	Angular velocity [rad/s]
ϕ	Power factor angle [^{o}]
θ_s	PLL Angle [^{o}]
θ_s	Phase angle of the BESS terminal voltage [^{o}]
ξ	Predicted value error with respect to measurements
C_e	GA population in generation e
d	Duty ratio [p.u.]
$D_u\boldsymbol{\varphi} \mid_o$	Jacobian matrix of linearized vector function $\boldsymbol{\varphi}$ with respect to u
$D_u\boldsymbol{\vartheta} \mid_o$	Jacobian matrix of linearized vector function $\boldsymbol{\vartheta}$ with respect to u
$D_z\boldsymbol{\varphi} \mid_o$	Jacobian matrix of linearized vector function $\boldsymbol{\varphi}$ with respect to z
$D_z\boldsymbol{\vartheta} \mid_o$	Jacobian matrix of linearized vector function $\boldsymbol{\vartheta}$ with respect to z
$D_z\Phi \mid_o$	Jacobian matrix of the ODE system
f	Frequency [Hz]
I	Current [A]
I_{dc}	Dc link current [A]
I_L	Dc-to-dc converter's inductor current [A]
m	Modulation index
N	Number of neurons per layer
P	Active Power [W]

P_{BESS}	Aggregated active BESS power injection at the boundary bus [W]
P_{Bus}	Active power measurements at the boundary bus [W]
P_{eq_L}	Aggregated active load at the boundary bus [W]
$P_{eq_{PV}}$	Aggregated active PV power injection at the boundary bus [W]
P_{L_o}	Aggregated active load at distribution system bus level [W]
P_{PV_o}	Aggregated active PV power injection at distribution system bus level [W]
PV	Signal proportional to solar irradiance [p.u.]
Q	Reactive Power [VAr]
Q_{BESS}	Aggregated reactive BESS power injection at the boundary bus [VAr]
Q_{Bus}	Reactive power measurements at the boundary bus [VAr]
Q_{eq_L}	Aggregated reactive load at the boundary bus [VAr]
$Q_{eq_{PV}}$	Aggregated reactive PV power injection at the boundary bus [VAr]
Q_{L_o}	Aggregated reactive load at distribution system bus level [VAr]
Q_{PV_o}	Aggregated reactive PV power injection at distribution system bus level [VAr]
SW	Switch state $\{0, 1\}$
t	Time [s]
T_e	Electrical torque [Nm]
T_m	Mechanical torque [Nm]
u	Algebraic variable
V	Voltage [V]

V_{dc}	Dc-to-dc link voltage [V]
V_{in}	Voltage at the terminals of the battery pack [V]
x	NN input variable
y	NN output variable
z	State variable

Sub- and Super- scripts

$\check{}$	Predicted value
Δ	Variation
$\hat{}$	Per-unit value
$\bar{}$	Averaged value
$\_$	Reduced-resolution value
b	Base value
boost	Operation of dc-to-dc converter in boost mode
buck	Operation of dc-to-dc converter in buck mode
d	d axis
e	Index representing a generation in the GA
eq	Equivalent
g	Generator
h	Index of BESSs connected at the distribution system
i	Index of hidden layers in NNs

j	Distribution system bus index
k	Index of measured data points of the time series l used for validation only
l	Index of time series used in the black-box model training
LL	Lead lag
m	Mechanical
nom	Nominal value
o	Nominal
osc	Oscillation
P	Active Power
PQ	Constant PQ
Q	Reactive Power
q	q axis
r	Index of measured data points of the time series l
ref	Reference value for control variables
s	Terminals of the BESS
sys	System
t	Terminals of the VSC

Chapter 1

Introduction

1.1 Motivation

The penetration of Renewable Energy Systems (RESs) in electricity grids has increased worldwide over the past decade because of their decreasing costs, especially of solar and wind generation technologies, and in view of government support for the deployment of renewable generation projects to counteract global warming effects. In the early stages of development, only bulk RESs was economically feasible because of their high capital costs; however, nowadays small-scale RESs installations are being deployed by consumers to achieve energy resiliency and independence, which are some of the characteristic of future smart grids. The integration of RESs presents some challenges, especially those associated with intermittency. In this context, Energy Storage Systems (ESSs) can provide the flexibility to mitigate the effects of intermittent RESs, while also increasing the system efficiency with the proper utilization of the energy generated by these resources [1], [2]. Even though large-scale ESSs facilities of most technologies are still not viable economically [1], utility-scale, and especially medium- and small-scale applications are viable options for Battery Energy Storage Systems (BESSs). The dropping prices of lithium-ion battery packs, accompanied by the increasing interest of household owners, industry, and commercial customers on installing dependable small-scale RESs, solar Photovoltaic (PV) being the most common, connecting electric vehicles to the grid, and using smart loads, is boosting the deployment of BESSs to facilitate the integration of these Distributed Energy Resources (DERs) at the distribution level, in the context of Active Distribution Networks (ADNs) [3]. However, their widespread adoption and penetration introduces new challenges in the operation of distribution systems, such as bi-directional power flows, and protec-

tion coordination. Thus, several projects of tens of MWs connected either at transmission and distribution system levels are being planned and deployed worldwide, such as the 100-MW/120-MWh Hornsdale project in Australia, which is the world's largest lithium-ion battery installation, which will provide grid services such as frequency regulation and capacity firming [4].

As the penetration level of DERs, particularly BESS and PV generation, increases in the ADN, their operation will also influence the transmission system upstream [3], [5]. Some of the issues are [3]: decrease in grid stiffness, reduction of transmission flexibility to accommodate changes in the load at the distribution level, larger frequency deviations due to reduction of system inertia, and grid stability issues. However, ADNs have the potential of improving transmission operations if the operation of the two systems are coordinated, since some DERs, especially BESSs, are fast in nature and, thus, can provide services, such as frequency regulation, voltage control, and/or oscillation damping. Since BESS can help address some of these issues at the transmission level either directly connected at the transmission system or spread within the distribution systems, appropriate models are needed to better understand their impact and potential contributions.

The excessive computational burden involved in modeling an actual distribution grid with all its components, along with the transmission grid, for integrated systems studies, has motivated the use of aggregated models of distribution system components. For example, different approaches to develop equivalent models of Distributed Generation (DG) sources (solar, diesel, and wind) are reported in the literature [6–8], and extensive work has been reported on the development of load models [9, 10]. However, little research has been conducted on finding equivalent dynamic models for distributed BESS. As a result, this is an open area of research that needs to be investigated, considering the growing number of DERs, especially BESS, that would likely be required in the near future [4]. In order to study the role and impact of distributed BESSs on transmission systems, and in the absence of data from distribution systems with actual distributed BESSs connected to them, simulations of benchmark test systems can be used instead, for which suitable models that allow simulating BESS providing grid services, such as frequency regulation, are needed.

From the aforementioned discussion, the main objective of this thesis is to investigate and propose BESS models with adequate control features to provide grid services, and analyze their applications in transmission system dynamics, either when directly connected to the transmission system, or when operating as part of ADNs. For the latter, models to represent the aggregated response of small-sized residential installations and medium-sized BESS for commercial and industrial applications, will be developed based on measurements of electrical variables at the boundary bus between transmission and distribution, which

is an approximate but practical modeling approach.

1.2 Literature Review

In this section, a literature review on modeling, impact analysis, and aggregation of BESSs connected to transmission systems is presented. The scope of the BESS models and studies in this thesis is focused on those relevant for dynamic studies of power systems.

1.2.1 BESS Models and Studies for Utility-scale Applications

Most existing BESS models concentrate on representing the dynamics of the controllers, neglecting the Voltage Source Converter (VSC) and its limits. Also, the dc-to-dc converter that connects the VSC and the batteries, is normally represented as a voltage or current source. In [11], for example, a generic mathematical model of an ESS connected to the transmission grid is proposed, and a BESS is modeled as a STATCOM connected to a battery on its dc side, which is represented by a dc source in series with a resistor, both in parallel with a capacitor. The VSC that connects the BESS to the grid is represented as an average model. Thus, the dynamic response of the BESS is exclusively determined by the capacitor in the dc link between the battery and VSC, and PI controllers are used to regulate the dc link voltage and the ac terminal voltage of the VSC. However, this model does not allow control over the active or reactive power, and a dc-to-dc converter to control the charge and discharge of the battery is not considered.

In [12], a BESS is also modeled as a STATCOM with a storage unit that allows exchange of active power with the grid, and which is used to enhance the transient stability and oscillation damping of a test power system. The VSC, which is connected to the main grid through an RL filter, is modeled as a current source, with its d- and q-axis components represented by differential equations. However, this model assumes a constant dc link, thus neglecting the dc-to-dc converter dynamics. Furthermore, the proposed passivity-based control requires formulating the test system, including the BESS, as a port-Hamiltonian model, which makes it impractical to study the BESS connected to a large test system.

In [13], a generalized average ESS model is developed, which can be parametrized to behave as a BESS, and used for voltage and angle stability analyses. This generic ESS model considers a VSC whose dc side can be supplied by any dc source, such as a battery bank, a Super Capacitor (SC), or another VSC. Furthermore, the ESS is modeled by a set of linear and Differential-algebraic Equationss (DAEs), whose structure is independent

of the storage technology. Decoupled controls for active and reactive power output and State of Charge (SoC) control are implemented. However, the proposed generic controls do not allow simultaneous operational modes of the BESS, such as frequency regulation and oscillation damping, and the dc-to-dc converter and its controller are not modeled in detail.

A similar average model is discussed in [14], where a BESS connected to an infinite bus is considered to study the effects of SoC and battery aging, demonstrating that reduced internal battery voltages can lead to instability in the dc-to-dc converter and the BESS. However, although the dc-to-dc converter is studied in this work, it is not modeled connected to the VSC, and is rather represented as a resistive load at the dc-to-dc converter terminals. Also, the VSC controls are not included, and the BESS is not tested connected to a power system.

Researchers in [15] used a modified version of the generic RESs models reported in [16], to model a BESS for dynamic simulations in power system studies. These models have been adopted by the Western Electricity Coordinating Council (WECC), and are widely used in research and by industry [17]. The control strategy of this model was tested in [18], and validated with real data in [15]. The BESS model in [17] comprises three modules of a so-called second-generation generic RESs: energy converter model (REGC_A), electrical-control model (REEC_C), and plant controller (REPC_A). A current control strategy for the VSC is modeled in the REPC_A, which allows the BESS to provide frequency regulation, constant PQ control, constant power factor control, and voltage regulation with droop characteristic. Also, a current control limiter is incorporated in REPC_A (referred to as REPC_C), which prevents the BESS from operating overloaded by limiting the current that can be drawn from the VSC, whereas an SoC logic control limits the current, in the event that the storage is completely charged or discharged. An alternative SoC control logic was proposed in [19] for these models. The control strategies of [17] are tested in [18], while the accuracy of model response is compared to real measurements in [15]. In [20], modules REGC_A, REEC_C, and REPC_A are replaced by more accurate modules REGC_C, REEC_D, and REPC_C respectively. However, the WECC models neglect the dc-to-dc converter, which does not allow to properly simulate the dynamic response of a BESS when its battery cells are degraded. Furthermore, the models do not explicitly include oscillation damping control, and Secondary Frequency Regulation (SFR) capability is also not considered. Furthermore, the simplified current control used in REPC_C does not model the existing coupling between the d- and q-axis VSC voltages and currents, neither the limits for modulation indexes, both of which can be relevant during transients.

A BESS model is presented and tested in [21] to improve frequency and voltage stability of a power grid, supported by a STATCOM. PI-lead and lead/lag regulators are proposed

for the BESS, and their effectiveness is compared with traditional PI-based controllers in a multimachine system. The battery bank is modeled as a dc voltage source and an internal resistance, where the SoC of the battery is a function of battery current. Independent control branches for frequency and voltage regulation are used, which act on active and reactive power controllers that generate reference current signals in the current controller. An additional controller uses the SoC signal to limit the BESS charging/discharging capability. This work, however, does not consider the dc-to-dc converter, the provision of multiple services simultaneously such as frequency regulation and oscillation damping, and used a detailed 3-phase VSC model instead of an average one.

In [22], a control strategy to improve the voltage regulation of the dc-link and dynamic performance of a BESS is presented, considering a reduced-size capacitor at the dc-link. An average dynamic model of a BESS is defined based on averaging techniques for both ac/dc and dc-to-dc converters. The duty ratio of the dc-to-dc converter is controlled through a feed-back/feed-forward control, which contributes to the reduction of the dc-link voltage variations to improve the BESS performance. However, as in [14], the VSC and dc-to-dc converters are treated separately and not integrated into a single BESS model, and controls for frequency, oscillation damping, and ac voltage regulation are not considered.

Some BESS dynamic models have been proposed for microgrids, which due to their intrinsic unbalance condition require three-phase and detailed representations. For example, in [23], detailed and approximate three-phase BESS models, including average models, are proposed and compared through dynamic simulations when connected to a benchmark microgrid. The proposed average model considers the battery, buck/boost converter, and VSC converter; however, it does not consider the provision of multiple services simultaneously, such as frequency regulation and oscillation damping. On the other hand, highly simplified dynamic BESS models have been proposed for frequency regulation studies, as in [24–27]. For example, in [27], a BESS is represented by as first-order transfer function including two control loops, one for PFR and a derivative component to provide virtual inertia in power systems with a significant number of inverter-based generators. Similarly, researchers in [28] model a BESS as a first-order dynamic system including limits, to study its application for oscillation damping control. However, the oversimplifications of these approximate model do not allow their complete representation of the actual BESSs, nor to investigate their limitations during transients.

Researchers in [29], introduce a BESS model for power system stability studies, which is used to improve the torsional damping of a synchronous generator. The system modeled, considers a battery bank directly connected to the dc side of a line-commutated inverter, which is interfaced to the main grid through a transformer that acts as a filter. The inverter's power injections are modeled by a set of steady state equations, with its dynamics

represented by a first-order transfer function. The battery bank is modeled as a dynamic Thevenin's equivalent, similar to the one described in [30]. A lead-lag controller is proposed to regulate the BESS' active and reactive power. The synchronous generator speed signals along with the inverter's terminal voltage are used to determine the BESS' operating point. This system, however, unlike most modern BESSs based on VSC, is based on a line-commutated converter, thus providing only one degree of freedom for control, which has several disadvantages, including not allowing independent PQ control.

Since the scope of this thesis is on the effects of the BESS transmission grid, only balanced single-phase average BESS models will studied. On the other hand, as the BESS' power injections to the grid increases, the results from average models start to deviate from those obtained with more accurate ones that consider the effects of switching. One of the main reasons for these differences is that the limits in the control system are reached faster in detailed models due to switching. Therefore, an assessment of the equivalence of the detailed and average BESS models is necessary, especially for utility-scale applications in which the operation of the BESS can impact the system. Even though extensive modeling of BESS is covered in the literature, few works, including some previously reviewed in this section, study the differences between approximate models, such as average models, with the detailed ones in the context of transmission system operator in [23], for example, detailed and approximate BESS models for microgrid applications are compared through dynamic simulations when connected to a benchmark microgrid. In [31], a validation of generic WECC BESS models is carried out with respect to a 3-phase detailed model connected to an infinite bus. However, the dynamics of the bi-directional buck-boost converter and its controllers are not considered in either of this work. In [32], an average model of a BESS which includes the dc-to-dc converter dynamics is compared with a detailed model. However, the dc-to-dc converter control does not take into consideration the limits for the inductor current; the BESS is tested for step changes in the power reference only (for these comparisons); the effects of limits on the accuracy of the two models are not examined; and the BESS models are not demonstrated in a grid context.

1.2.2 Aggregated BESS Models

Methods to develop aggregated models for traditional generating units, electric motors, and other types of loads are widely available in the existing literature (e.g., [9,33–35]), whereas aggregated models of power-electronic based generation and ESSs are less common, and still under investigation. Aggregated models of ADNs for transmission system studies have been proposed in [6] and [36], where equivalent gray-box models of ADNs are discussed, based on active and reactive power measurements at the point of connection with the

transmission system. These equivalent models comprise a converter-connected generator and a composite load model in parallel, which can successfully reproduce the results of a detailed model; however, these models do not allow changes in the operating points of generating units within the ADNs and, furthermore, BESSs are not considered.

In [37], a state-space equivalent of a distribution system connected to a transmission grid is studied, whose parameters are obtained from measurements of active and reactive power, and voltage and frequency at the boundary bus. This aggregated model is based on traditional generating units, i.e., steam, hydro and diesel. An aggregated gray-box model of ADNs comprising several microgrids with BESSs for frequency stability studies is proposed in [5]. The model is based on first-order transfer functions, the parameters of which are obtained using Prony analysis on measurements of active power at the ADN boundary bus and the upstream grid, and a clustering approach based on similar responses of the microgird in the ADN. However, only inverter-based and synchrnonus generators are considered in the ADN, and multiple transfer functions representing clusters of generators within the gray-box model are required.

More simplified models have been studied, such as the one in [38], where the impact of considering DERs, such as ESS or DGs, in aggregated distribution systems at transmission-level buses for transient stability studies is investigated. In this work, a grey-box model that comprises a High Voltage Direct Current (HVDC) system supplied by an infinite bus is proposed to represent the aggregated effect of BESSs. However, the authors do not discuss the aggregation process or the effectiveness of the proposed model.

A methodology to coordinate geographically dispersed DERs, including ESSs and DGs, in distribution systems is presented in [39]. The proposed methodology aims to control the operation of individual DERs, such that they can contribute to voltage and frequency regulation, and also damp the system low-frequency oscillations. The authors demonstrated through simulations that, due to their strategic location close to the load and fast response, these DERs could better improve operating conditions of transmission systems with traditional resources such as large generators. Even though aggregation of resources at the distribution level and their impact or the transmission operations are discussed in this work, aggregated models for these DERs are not investigated.

The impact of DG and BESS on a distribution system are examined in [40] using an 8-bus feeder. The stability of the system is evaluated as a function of the maximum rotor speed deviation of the DGs for different penetration levels. The battery pack of the BESS is modeled as a steady-state RL circuit, whose parameters are a function of the SoC and current injected/absorbed by the battery. Simulations show that stability is improved when the BESS is installed in the system with higher DG penetration levels. However,

the dynamics of the BESS are neglected, and the model only focuses on the battery pack component, while the dc-to-dc converter, VSC, and controls are not considered.

Black-box models based on Neural Networks (NNs) have also been used to represent equivalent ADNs. For example, in [41], a Recurrent Neural Network (RNN) black-box model is proposed to represent a distribution system connected to a transmission grid; however, only fuel cells and microturbines are considered as DERs, and the aggregated model is developed considering only voltage disturbances at the boundary bus with the transmission system. In [42], RNNs are used to model part of a transmission system, the NN black-box model is connected to the transmission gird at three different points, using measurements of the voltages at each boundary point as inputs, and yielding current-phasor injections as outputs; however, the system modeled is based on rotating machines only.

1.2.3 Discussion

Based on the aforementioned literature review, it can be highlighted that most of the previously reported BESS models for dynamic power system studies, neglect the dc-to-dc converter, its associated controllers, and the battery bank. Such assumptions are justified because of their large computational burden; however, during transients or when the battery cells have been degraded due to ageing, modeling the dc-to-dc converter dynamics is essential, as these can cause instabilities in the dc-link voltage, thus affecting the VSC and the BESS [32]. Furthermore, sudden drops in the dc-link voltage during transients, combined with large power injections in the ac side, might force the VSC modulation indices to reach their limits thus affecting the BESS. Therefore, to study the dynamics operating conditions of such on a BESS, as in the case of transient stability and voltage and frequency regulation analyses, proper representation of the VSC, dc-to-dc converter, and their associated controls is important in a BESS model; this is one of the contributions of this thesis. In this context, the average BESS models investigated must be compared against detailed models, which considers the high-frequency effect of the converters' switches, to validate their dynamic response, and also identify their limitations.

Another drawback of existing BESS models and controls is their lack of capability to provide simultaneous services, such as frequency regulation and oscillation damping, which would permit to fully explore and demonstrate the BESS potential when connected to a power grid. Also, the use of BESS for frequency regulation services has been limited to PFR, although the potential of bulk BESS facilities to provide Secondary Frequency Regulations (SFRs) is considerable; in fact, this has drawn the attention of several Independent System Operators (ISOs), including the Ontario's Independent Electricity System Operator (IESO), which has contracted BESS capacity to follow regulation signals proportional

to the Automatic Generation Control (AGC) signal that is sent to conventional generating units [43].

In terms of studies performed, only a few papers examine the impact of small- and medium-scale BESS connected to distributions systems, on the transmission systems; mainly because of the complexities involved in representing distribution systems for transmission grid studies. In order to address these shortcomings, aggregated models can be used; however, none of the aforementioned works have examined the aggregation of BESS, which are different from other DERs in that they can act as loads and generators. Furthermore, the dynamic response of a BESS to contingencies can be substantially different from the typical behaviour of a rotating-machine based generation, due to their fast response to contingencies. Therefore, one of the main contributions of this thesis is to propose aggregated models of BESSs in ADNs for transmission grid studies. Since, as discussed in some of the afromentioned works, aggregated gray-box models have the limitation of mostly being effective to reproduce single operating points of the dispersed DERs, black-box models will be used here, as these are able to capture more complex nonlinear behavior such as multiple operating points and device limits.

1.3 Research Objectives

Based on the literature review and discussions, the following are the main objectives of the research presented in this thesis:

- Propose, validate, and demonstrate an average BESS model comprising a battery bank, dc-to-dc converter, VSC, and ac filter, and present novel controls strategies for frequency and voltage regulation, oscillation damping, constant PQ operation, and constant power factor. The proposed models should be compared with detailed simulations, which consider the switching effects of the converters. Moreover, they should be suitable for small-, medium-, and utility-scale power system applications, and parametrizable to simulate new or existing BESS facilities, in which the degradation of the battery cells need to be considered.

- Demonstrate the importance of modelling the dc components of BESS, especially for utility-scale facilities connected to transmission systems, providing services such as frequency regulation, voltage control, and transient stability.

- Propose, develop, and demonstrate an NN-based black-box model, optimizing its topology using Genetic Algorithms (GAs), that can reproduce the aggregated be-

haviour of distributed BESSs providing different services, i.e., frequency regulation, oscillation damping, constant power injections, and voltage regulation.

- Illustrate the impact of distributed BESSs in a benchmark ADN on a benchmark transmission system, for different grid contingencies.

1.4 Thesis Outline

The rest of this thesis is organized as follows:

- Chapter 2 discusses the fundamentals of BESSs and their components, and presents an overview of the Artificial Intelligence (AI) tools used to develop the black-box models. An overview of the electrical system studies that are performed to study BESS in a grid context are also discussed.

- Chapter 3 presents the novel formulation and derivations of the proposed BESS average model. New converter controls are also proposed, and the implementation of the model in a power system simulation software package is discussed. A validation of the proposed BESS model based on a detailed model is presented, and multiple system studies and comparisons with respect to existing models considering bulk BESS in transmission systems are shown and discussed.

- Chapter 4 discusses a transmission-system-level aggregated model of BESS connected at the distribution grid level for transmission system studies, based on two Neural Networks (NNs), one for active power and another for reactive power, with their optimal topology obtained using a Genetic Algorithm (GA). The accuracy, performance, and validation of the model are demonstrated through detailed dynamic simulations of benchmark transmission and distribution interconnected systems.

- Chapter 5 summarizes the main conclusions and contributions of this thesis, and outlines the scope possible future work.

Chapter 2

Background Review

In this chapter, a typical configuration of a grid-scale BESS is presented, with its individual components analyzed in detail. AI-based tools to develop black-box models are also discussed, as these will be used to propose a model of aggregated BESSs model at the distribution grid level for transmission system dynamic analyses. Finally, an overview of the studies required for the analysis of the grid services a BESS can provide, such as improvement of system stability and frequency regulation, is presented.

2.1 Energy Storage Systems

Energy storage refers to the process of converting energy from one form to another, and storing it through various methods for later use. A variety of energy storage technologies are currently available, which can be classified as: mechanical (Pumped Hdyro Storage (PHS), Compressed Air Energy Storage (CAES), and Flywheel Energy Storage (FES)), electrochemical (conventional rechargeable batteries and flow batteries), electrical (capacitors, Super Capacitor (SC), and Super Conducting Magnetic Energy Storage (SMES)), thermochemical (solar fuels), chemical (hydrogen storage with fuel cells), and Thermal Energy Storage (TES) (heat and cold storage) [2]. The main features of the most common ESSs, with the exception of BESS which is discussed in more detail later in this section, are the following [2, 43, 44]:

- PHS: It is a mature energy storage technology with large energy capacity. It consists of two water reservoirs separated vertically. Usually, water is pumped to the higher

during off-peak demand hours reservoir where it is stored, and released for power generation during peak hours. The amount of stored energy depends on the height difference between the two reservoirs and the total volume of water stored.

- CAES: During periods of low demand, the surplus of electricity can be used to operate a reversible motor/generator unit, which drives a compressor to inject air into a storage vessel (either an underground cavern or above ground tanks). The energy is stored in the form of high pressure air, which is released and heated with gas in a diabatic system to be used in a gas turbine to produce electricity. The heat produced in the compression stage can be stored and used in a recuperator unit to preheat the air from the cavern in an adiabatic system, to eliminate the need for gas air heating.

- FES: This technology comprises a flywheel and a reversible electrical generator/motor connected to the grid through a power electronic unit, plus a vacuum chamber where the flywheel spins to reduce air friction. Electricity consumed or generated accelerates or decelerates the flywheel, respectively, by means of a generator/motor system. The stored energy is a function of the rotating speed of the flywheel and its angular momentum.

- SC: This ESS uses two carbon electrodes which are isolated from one another through a porous membrane, immersed in an electrolyte, which allows ionic flow between the electrodes. The function of the membrane is to prevent the occurrence of short circuits between the electrodes. The energy is stored in the form of static charge on the surfaces of the electrolyte and the two conducting electrodes. New designs of SCs with high efficiency are based on nano materials.

- SMES: It is based on a power-conditioning system, a superconducting coil, and a refrigeration system. The energy is stored as magnetic field when a dc current flows through the superconductive coil. To increase the efficiency of the process, liquid helium or liquid nitrogen are used to cool down the superconducting coil below the critical superconducting temperature. Because of the use of superconducting materials in the coil, such as mercury or vanadium, which operate at a very low temperature, almost zero resistance is encountered by the current flowing through the coil, making this technology almost lossless.

- TES: This technology is based on storing thermal energy by cooling or heating different mediums in enclosures for thermal (heating or cooling) or power generation purposes. It is composed of a storage medium in a reservoir, a built-in refrigeration/heating system, pumps, piping, and their respective controls. Depending on

the range of operating temperatures, these can be classified into low-temperature TES (e.g., aquiferous low-temperature TES and cryogenic energy storage) and high-temperature TES (e.g., latent, sensible, and concrete thermal energy storage).

Due to their fast response and relatively large energy storage capacity, some of the aforementioned ESSs have the potential to enhance the operation of power systems by, for example, damping the intermittency of wind or solar generation by exchanging active and reactive power with the system; providing fast response for frequency regulation while charging or discharging; and providing load leveling services. In Figure 2.1, the most common sizes and application domains for different ESS technologies and their corresponding system domains are summarized.

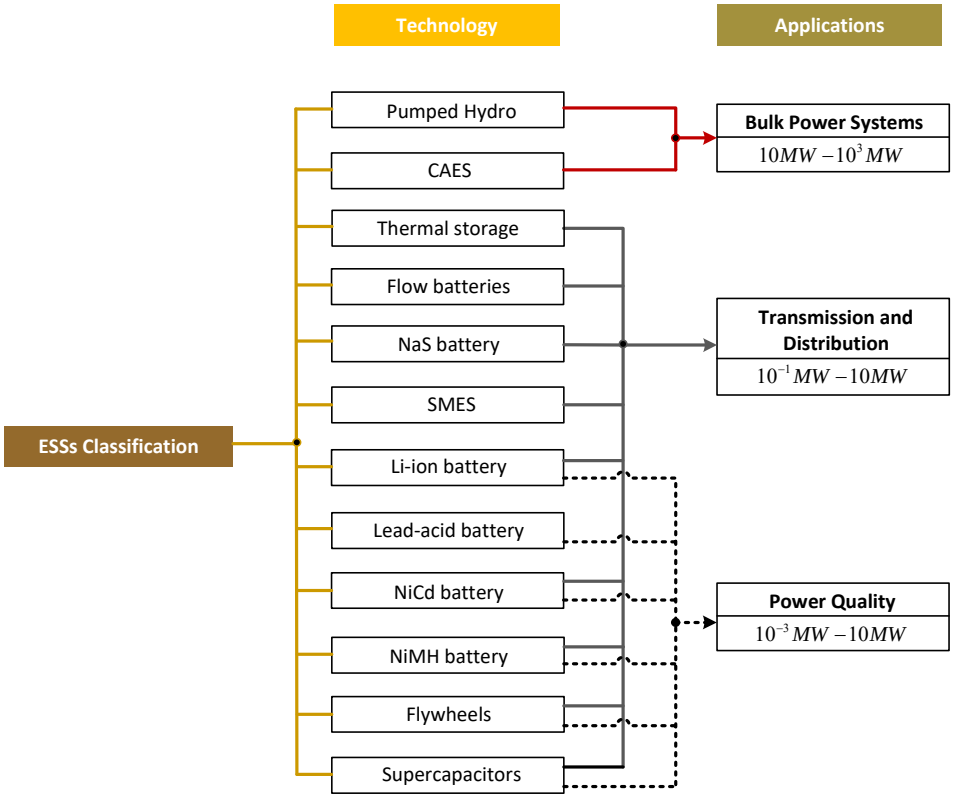

Figure 2.1: Typical energy storage technologies sizes and application domains [44]

2.2 Battery Energy Storage Systems

In BESS, electrical energy is converted into chemical energy and stored in electrochemical cells. Power-electronic converters are used to connect low-voltage battery arrays to the dc side of a VSC, which transforms the dc power to ac, and vice versa, depending on the direction of power flow. By properly controlling the converter switches, the battery cells can be charged and discharged, thus allowing the BESS to exchange active power with the grid, while reactive control is possible by charging and discharging a capacitor in the dc link. A filter is connected between the ac terminals of the VSC and the power grid, to reduce the harmonics injected, thus improving the power quality. A common configuration of a BESS for power system applications is depicted in Figure 2.2. Note that since the VSC can control two variables independently (two degrees of freedom), and that in a BESS the dc link voltage can vary with the charging/discharing power, the dc-to-dc converter is necessary to add a third degree of control. Hence, active and reactive power, and the dc link voltage can be independently regulated, thus allowing four quadrant operation with the BESS.

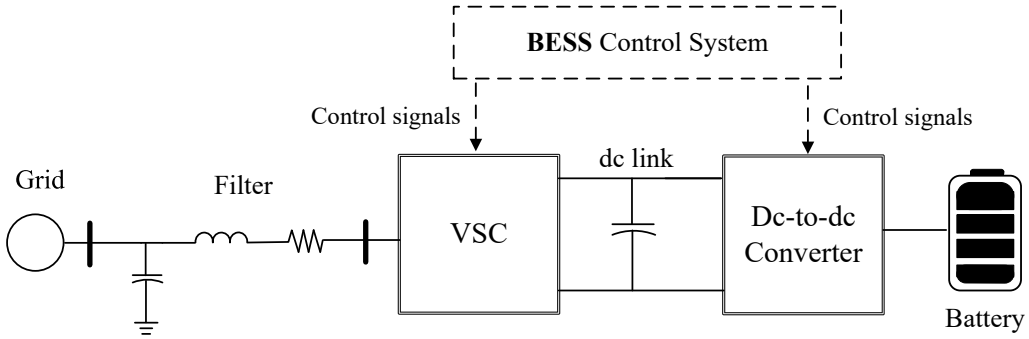

Figure 2.2: Schematic representation of BESS.

Applications of bulk and more the common distributed BESS in power systems to facilitate RES integration and/or deferral of capital investment (at the generation, transmission, and distribution level) include peak shaving, load leveling, load shifting, power quality management, spinning reserve, frequency regulation, and emergency backup power [45]. The type of batteries used depends on the application, and its choice is influenced by economic and technical aspects of each type. The most commonly used batteries for BESS and their corresponding characteristics are summarized in Table 2.1 and 2.2 [2].

The main components and control strategies of the BESS are discussed next. The converter topologies discussed will concentrate on those used on practical BESS installations

Table 2.1: Technical characteristics of BESS.

Technology	**Daily self-discharge [%]**	**Lifetime [years]**	**Discharge efficiency [%]**	**Cycle efficiency [%]**	**Response time**
Lead-acid	0.1	5-15	85	70-80	ms
Li-ion	0.1-0.3	5-15	85	90-97	ms
NaS	Almost zero	12-20	85	75-90	-
NiCd	0.03-0.6	5-10	75-82	65-75	<1/4 cycle
VRB	Small	5-10	60-70	65-75	<1/4 cycle
ZnBr	Small	10-15	60-70	65-75	<1/4 cycle

Table 2.2: Technical and economical characteristics of BESS.

Technology	**Suitable storage duration**	**Discharge time at power rating**	**Power capacity cost [$/kW]**	**O&M Cost [$/kW/yr]**	**Maturity**
Lead-acid	min-days	sec-hours	300-600	50	Mature
Li-ion	min-days	min-hours	1,200-4,000	-	Mature
NaS	long term	sec-hours	1,000-3,000	80	Commercialized
NiCd	min-days	sec-hours	500-1,500	20	Commercialized
VRB	hrs-months	sec-24h+	600-1,500	70	Commercialized
ZnBr	hrs-months	sec-10h+	700-2,500	-	Commercialized

at utility-scale levels.

2.2.1 Battery Banks

In BESS, individual battery cells are arranged in banks, connected in series and parallel, to achieve higher power ratings and produce the desired voltage at the dc side of the VSC. Each cell is composed of an anode and a cathode with an electrolyte (solid, liquid or viscous), which are able to convert electricity into chemical energy and vice versa [2].

In circuit simulations, the battery banks are usually modeled by standard electrical components, such as resistors, capacitors, inductors, and voltage and current sources, to represent the aggregated electrical behaviour of the battery cells connected in arrays. Accordingly, three categories of models are identified: Thevenin, impedance, and run-time-

based as depicted in Figure 2.3 [30].

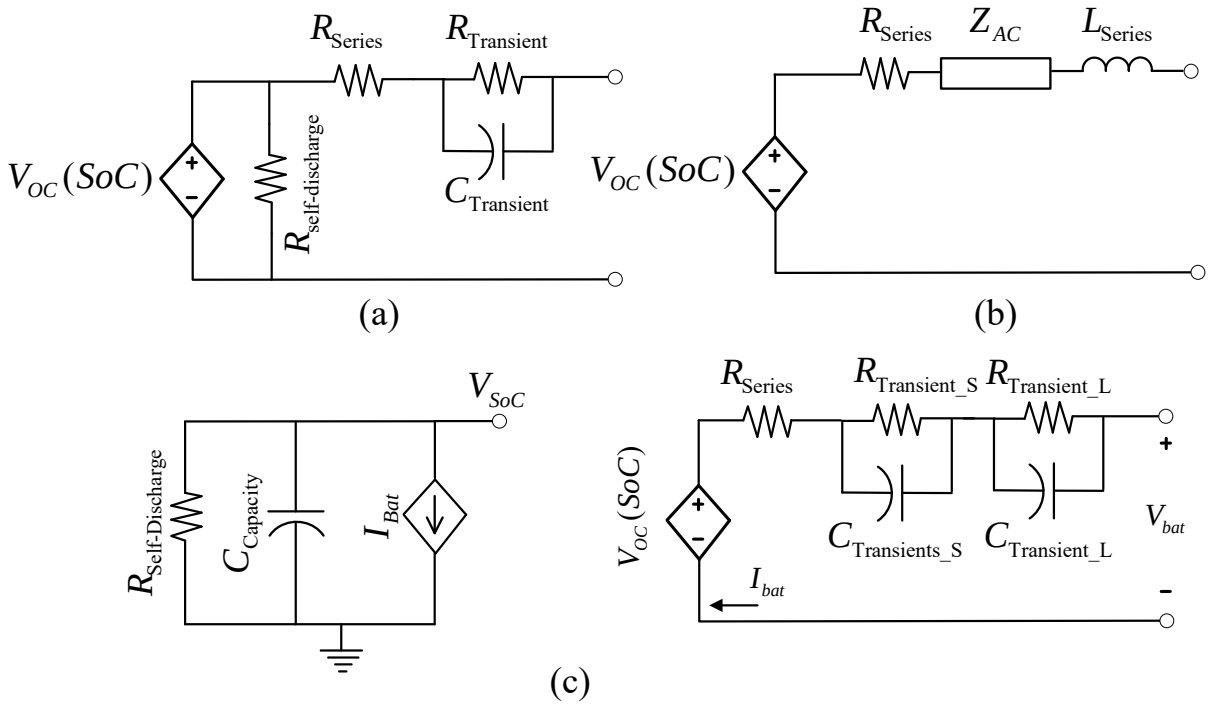

Figure 2.3: Battery models: (a) Thevenin, (b) impedance, and (c) run-time-based [30].

The Thevenin model, which is suitable to represent transient phenomena in the batteries, comprises a voltage source, representing the open-circuit battery voltage, connected in series with a resistor that models the internal battery losses, and an RC parallel branch representing the capacitance effect between two parallel plates and the contact resistance [46]. In impedance based models, a frequency dependent element is used to capture a wide range of frequency spectra in the battery's response, as opposed to the fixed circuit parameters used in the Thevenin and run-time-based models. Finally, run-time-based models, which are based on more complex circuit representations, incorporate the effects of the battery run-time on its performance, by considering a self-discharging resistor in parallel with a capacitor, representing the charge stored in the battery, which is discharged by a fixed current source, as depicted in Figure 2.3(c).

In most grid-level BESS models that consider the dc-to-dc converter, the battery bank model is a simplified version of the Thevenin equivalent, for example, the RC branch is neglected, resulting in a series resistive circuit [14, 23, 47], or further simplified as a fixed

voltage source only [13, 46, 48]. In this thesis, a controllable voltage source in series with a variable resistor will be used, which can be parametrized to simulate battery degradation due to aging [14].

2.2.2 Dc-to-dc Converters

Dc-to-dc converters are power-electronic based circuits that allow to change the magnitude of a dc-voltage input into a desired dc-voltage at the output, as transformers would do in ac systems. There are different types of dc-to-dc converters available in the literature [49], with the choice depending on the required application. In BESS, the dc-to-dc converter must allow bi-directional power flow to charge and discharge the batteries; therefore, a bi-directional Buck-Boost dc-to-dc converter is commonly used in BESS [48], as depicted in Figure 2.4.

This converter has two quadrants of operation; to change the direction of the power, the current I_{dc} has to change its direction while the voltage V_{dc} remains constant. In Figure 2.4, the battery bank is connected at the low-voltage side of the converter V_{in}, while the higher-voltage side V_{dc} feeds the dc link that connects this converter and the VSC, which is discussed later. Some relevant operational characteristics of the bi-direction buck-boost dc-to-dc converter are: V_{dc} must be larger than V_{in} all the time; the two switches S_{buck} and S_{boost} receive complementary signals for their operation; the direction of power flow depends on the duty cycle of the switches; the battery charges when the converter operates in buck mode, and discharges when operates in boost mode. In BESS, the dc-to-dc converter can be used to regulate the voltage at the dc link or control the charging/discharging active power of the battery bank.

Usually, the rating of the dc-to-dc converter is less than that of the VSC in large BESS facilities. Hence, multiple dc-to-dc converters are connected in parallel to match the VSC power rating, as illustrated in Figure 2.5 [48].

2.2.3 Voltage Source Converters

The VSC transforms dc voltage into ac voltage when operating as inverter, and ac to dc voltage when operating as rectifier, thus allowing the interchange of power between dc and ac sources. For BESS, three-phase two-level VSCs have been commonly used, and their basic configuration is shown in Figure 2.6. Switches in the same leg receive complementary signals to avoid short circuits if both operate at the same time, and since these usually allow

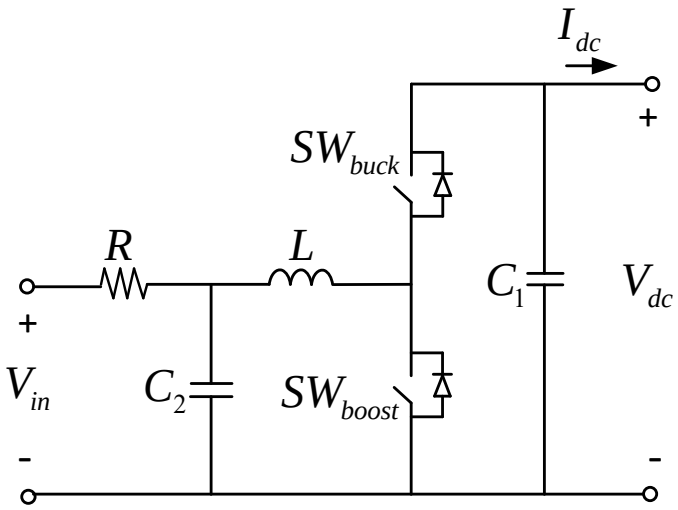

Figure 2.4: Electrical circuit of bi-directional buck-boost converter.

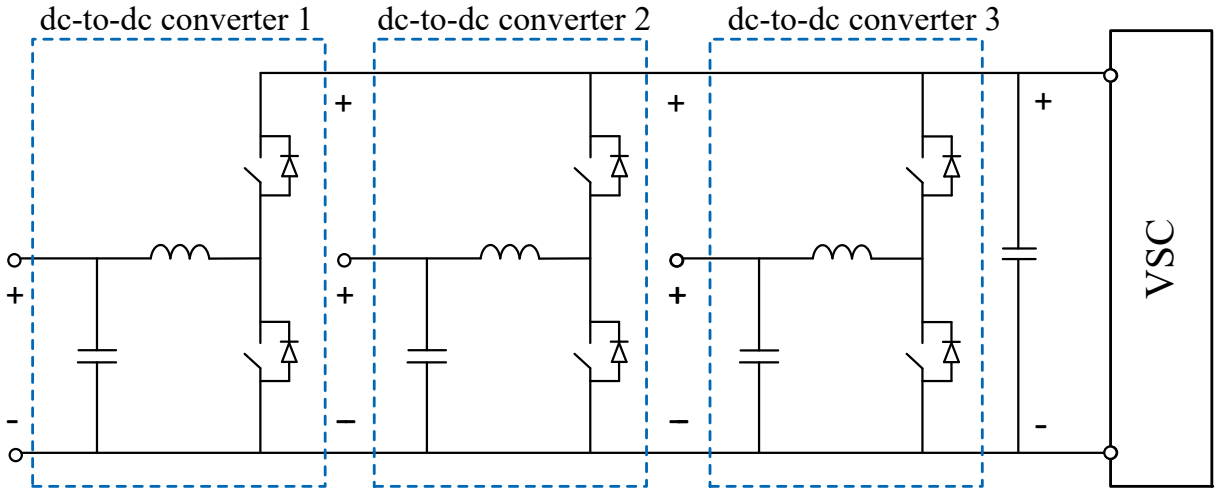

Figure 2.5: Parallel dc-to-dc converters connected to the dc link of a VSC.

current flow in one direction only, anti-parallel diodes are used to allow current circulation in the opposite direction when the switches are on.

The fundamental component of the terminal voltage of each phase of the VSC is typically controlled by a Pulse Width Modulation (PWM) technique, which sends control signals to the switches by comparing three sinusoidal modulating phase signals $v_{control_{abc}}$,

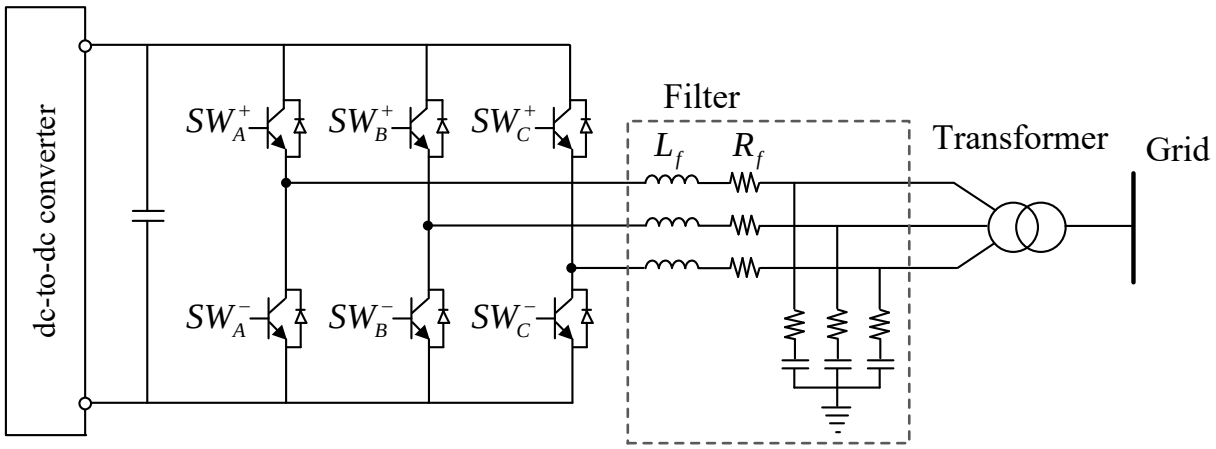

Figure 2.6: Three phase VSC.

whose phase (shifted 120^o each) and frequency are the same as the desired output voltages, with a high-frequency triangular carrier signal v_{tri}, as illustrated in Fig. 2.7. The ratio of the amplitude of the two signals, $\check{v}_{control}/\check{v}_{tri}$ is called the modulation index m. Whenever $v_{control} > v_{tri}$, a signal is sent to operate the corresponding switches. The frequency of the carrier signal determines the amount of harmonics in the output voltages; hence, although high frequencies are easier to filter, these are not desirable for large power applications, as these also result in higher switching losses.

Active and reactive power control with the VSC can be accomplished by regulating the amplitude and phase of the modulating phase signals $v_{control_{abc}}$. The reactive power control is possible through the capacitor in the dc link, which in combination with the dc-to-dc converter, allow the BESS to operate in all quadrants of the P-Q plane, known as four-quadrant operation [50]. In BESS, a current control logic is commonly used to regulate P and Q through the VSC, leaving the regulation of the dc link voltage to the dc-to-dc converter [14, 23].

For large power applications, as the ones investigated in this thesis, identical VSC units can be connected in parallel to achieve the overall BESS power rating, as shown in Figure 2.8 [1]. The VSC is connected to the grid through LC filters or simply through a transformer, whose inductance acts as a filter, as depicted in Figure 2.2.

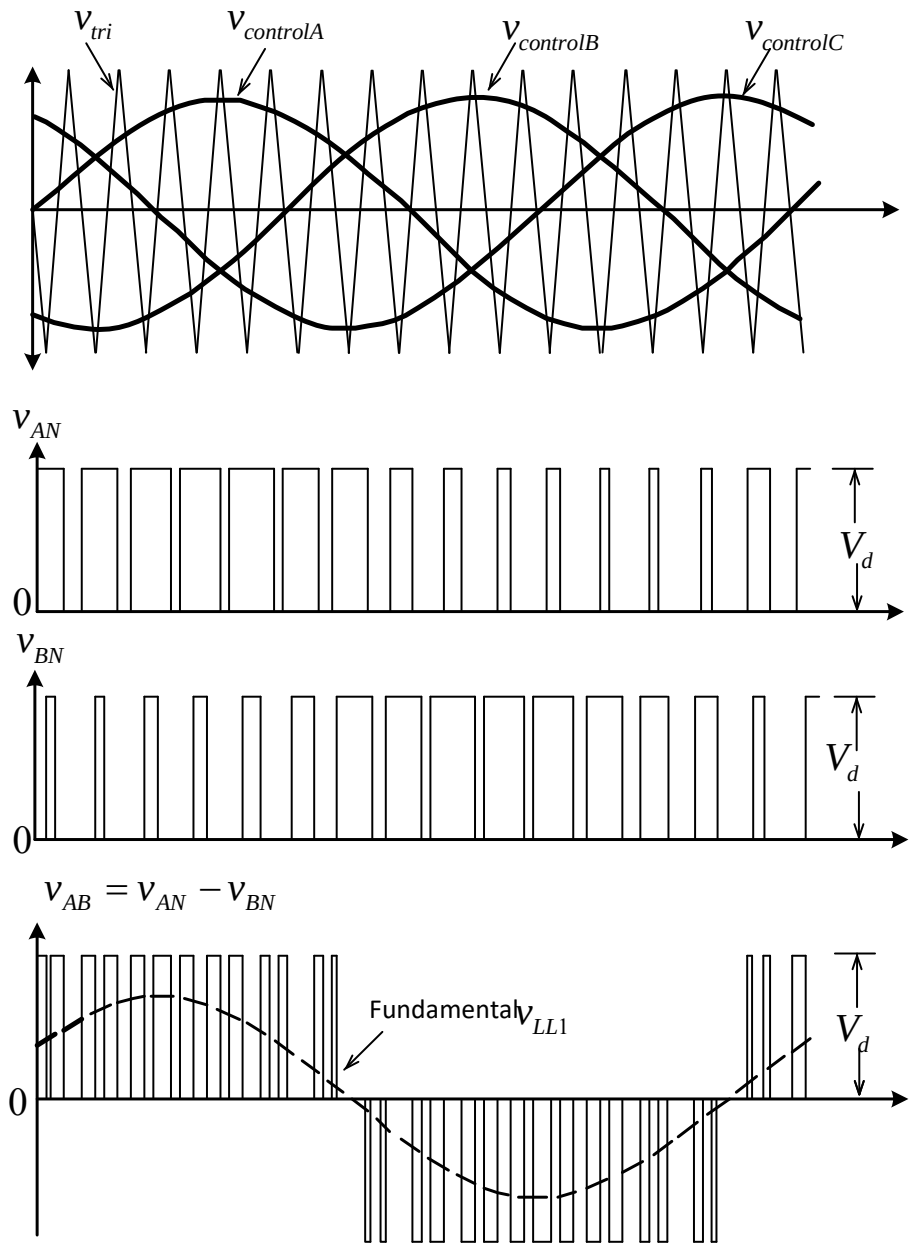

Figure 2.7: Pulse width modulation technique VSC.

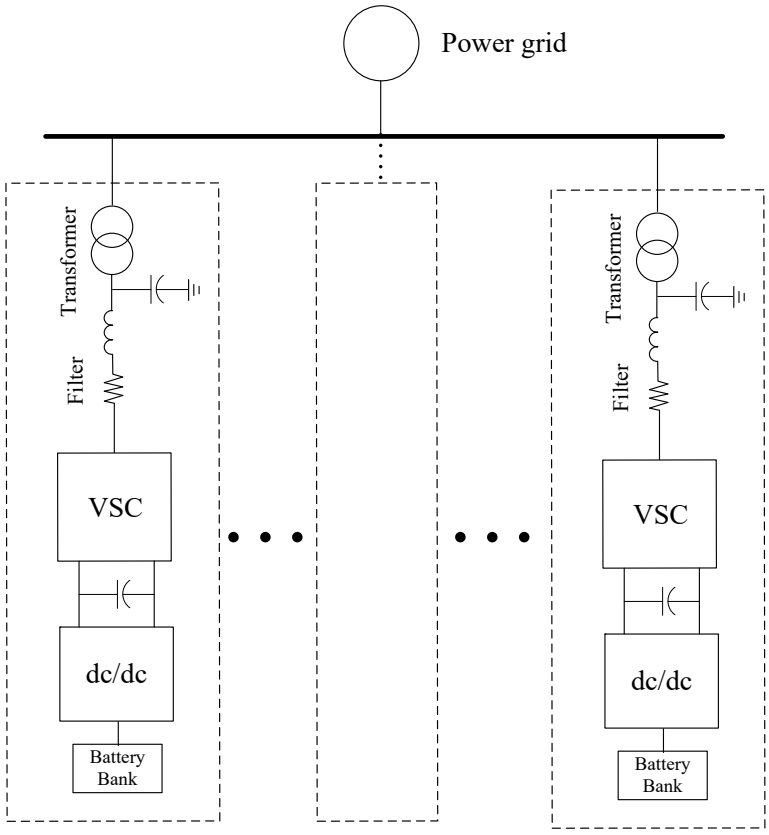

Figure 2.8: Parallel connection of VSCs in a BESS.

2.3 AI Tools for Black Box Models

AI can be defined as the science of making machines do things that would require intelligence if done by humans [51]. Some tools and theories that demonstrate such capacity are NNs, support vector machines, and evolutionary computing, all of which can be used to solve problems that are either difficult to model or cannot be solved by traditional techniques. In general, AI tools learn to recognize and reproduce patterns or behaviours of the system to be modeled, based on actual observations known as training data. The AI tools are also able to predict the system response for which they were not trained; such desirable property is known as generalization.

AI tools, have proved to be effective in several areas, including intelligent control, black box modelling, parameter estimation, nonlinear optimization, to name a few. In this thesis,

AI will be used to develop dynamic black box models of aggregated BESS, for which RNNs are particularly effective, whereas GA will be applied to find the optimal black-box model topology. These tools are discussed next.

2.3.1 Artificial Neural Networks

Black-box models based on NNs are widely utilized to represent highly non-linear complex systems, as in the case of measurement-based aggregated models. These NN models map inputs and outputs, based on a connectionist structure that aims to resemble the structure of a human brain, i.e., multiple nodes (neurons) interconnected with each other exchanging information [51]. The basic processing unit in a NN is the neuron, which is characterized by a set of input connections affected by a vector of weights that represent the state of the NN and a bias term (b), as depicted in Figure 2.9, with its main feature being its learning capability that is accomplished by weight adjustments. The summation of the weighted inputs are mapped in each neuron by nonlinear functions called activation functions ψ, resulting in an output which is usually a value between 0 and 1, or -1 and 1.

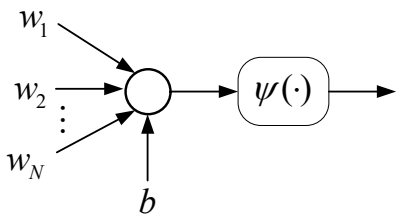

Figure 2.9: Basic neuron configuration.

The neurons are structured in layers, with the input and output layers handling the input and output signals of the NN, and one or multiple hidden layers connecting the input and output layers. The most common structure is the feedforward NN, in which the neurons' outputs from one layer are fed as inputs of the neurons in the next layer, so that the information flows in one direction only. Other types of NNs include RNNs, where neurons from different layers are connected regardless of their relative position, i.e., the outputs of the neurons can be part of the inputs of the neurons of any layer, thus forming loops and adding memory capability to the NN. One type of RNN is the Nonlinear Autoregressive Exogenous (NARX) NN, discussed next.

One effective and practical method to develop aggregated black-box models is the measurement-based system aggregation. In this method, simulation or real-time data is

used to train a NN model, whose weights (parameters) are adjusted until the NN outputs properly match the available measurements, based on an iterative process that uses the model's estimation errors as the main criteria for the weight adjustments (e.g. [52]), as depicted in Figure 2.10. In this context, NARX NNs topology is particularly effective to represent dynamic systems, as it is the case of aggregated BESS. In this type of NN, the estimated output is represented as a function of past measurements of the system to be replicated, and feedback of past measurements of the expected outputs (open-loop architecture), as follows [52]:

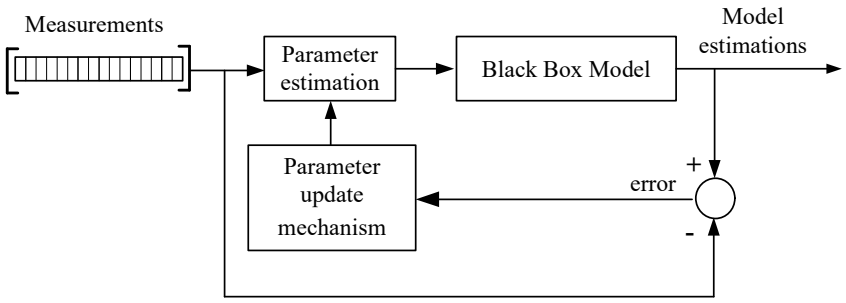

Figure 2.10: Measurement-based black box model for aggregation.

$$\check{y}_t = G\begin{pmatrix} y_{t-1}, y_{t-2}, ..., y_{t-n_y}, \\ x_t, x_{t-1}, x_{t-2}, ..., x_{t-n_x} \end{pmatrix} \tag{2.1}$$

or past estimated outputs (close-loop architecture):

$$\check{y}_t = G\begin{pmatrix} \check{y}_{t-1}, \check{y}_{t-2}, ..., \check{y}_{t-n_y}, \\ x_t, x_{t-1}, x_{t-2}, ..., x_{t-n_x} \end{pmatrix} \tag{2.2}$$

where G is the NN mapping function; $\check{y}_t$ is the predicted NN output at time t; x_t and y_t are actual past values of inputs and outputs of the time series to be reproduced, respectively; and n_x and n_y are the number of input and output past information (or delays), respectively. The function G has the trained weights as parameters, which are adjusted based on the procedure depicted in Figure 2.10.

2.3.2 Genetic Algorithms [51]

GA are motivated from the biological process of evolution and the survival-of-the-fittest concept. Indeed, the concept of evolution is applied to find optimal solutions for nonlinear optimization problems. The main differences with respect to traditional optimization techniques is that GAs are not restricted to differentiable objective functions, and that the search algorithm is stochastic, allowing a broader range of possible solutions. As a result, GAs are more likely to yield a closer, although not necessarily precise, solution for global optima.

The main steps in GA start with the definition of the population of individuals; different populations may produce different solutions to the problem. The population is evaluated through a fitness function that resembles the capacity of animals to survive in a specific habitat, which rewards populations that produce results closer to the desired solution, and penalize them otherwise. The individuals that produce satisfactory solutions survive to the next generation (selection); this process is known as the survival of the fittest. The survived individuals form the base for the reproduction (cross over and mutation of the chromosomes) for the following generation, which results in new individuals that share characteristics from each parent.

GAs can be used as part of the training process of NNs to find the optimal weights, or to obtain the optimal NN topology. The latter will be applied in this thesis to optimize the topology of the Black-box aggregated model of BESSs.

2.4 Power System Stability and Control

Power system stability is defined as "the property of power system that enables it to remain in a state of operating equilibrium under normal operating conditions and to regain acceptable state of equilibrium after being subjected to a disturbance" [9], [53].

The stability problem can be classified into three categories, which are defined based on key variables of the power systems: angle stability, frequency stability, and voltage stability. A more detailed classification is presented in Figure 2.11 based on [9], [53]. This classification considers the nature of the resulting mode of instability, as observed from a particular system variable (voltage, angle, or frequency), the size of the disturbance, and/or time-frame of the phenomena.

Rotor or angle stability refers to the capability of synchronous machines of an interconnected power system to remain in synchronism after being subjected to a disturbance.

Thus, a system is stable if it is able to react to such disturbances by maintaining/restoring the equilibrium between the electromagnetic torque and mechanical torque of each synchronous machine. This type of stability is mainly influenced by fast electromechanical phenomena; however, it is also affected by the slower dynamics associated with the mechanical components and controls of power generation plants. Thus, angle stability can be sub-classified as:

- Small-disturbance stability, which is the ability of the system to maintain the synchronism under small disturbances, and is usually associated with undamped or weakly damped low frequency oscillations in the system.
- Large-disturbance or transient stability, which is related to the ability of the system to remain stable after a severe disturbances such as short circuits.

Voltage stability can be studied from two perspectives, long term and short term. The former addresses issues related to insufficient reactive power reserves in the system, to preserve steady-state voltages at all buses due to load increments and violation of generators' limits. On the other hand, the latter is more concerned with the inability of the system to quickly supply reactive power in response to large disturbances, such as loss of generation, line contingencies, and system faults.

Frequency stability is based on the principle of balancing generation and demand. This type of stability focuses on the ability of a system to maintain the frequency within acceptable margins when a disturbance affects the balance between load and generation. Frequency instability may also result in the form of sustained frequency swings, leading to tripping of generating units and/or loads because of inadequate equipment responses, poor coordination of control and protection devices, or insufficient generation reserves.

2.4.1 System Stability Studies

Different techniques are used to evaluate the stability of power systems, which depend on the type of stability problem to be analyzed. For small-disturbance stability, the preferred method is eigenvalue analysis, which requires finding the complex eigenvalues of a linearized model of the system, and determine whether any of them are located near the imaginary axis or on the right-hand side of the imaginary axis; if that is the case, the system is considered lowly damped or unstable since modes with low or positive exponentials with respect to time, will appear in the time-domain expressions of some system variables as sustained or undamped oscillations, respectively. The linearization of the system is

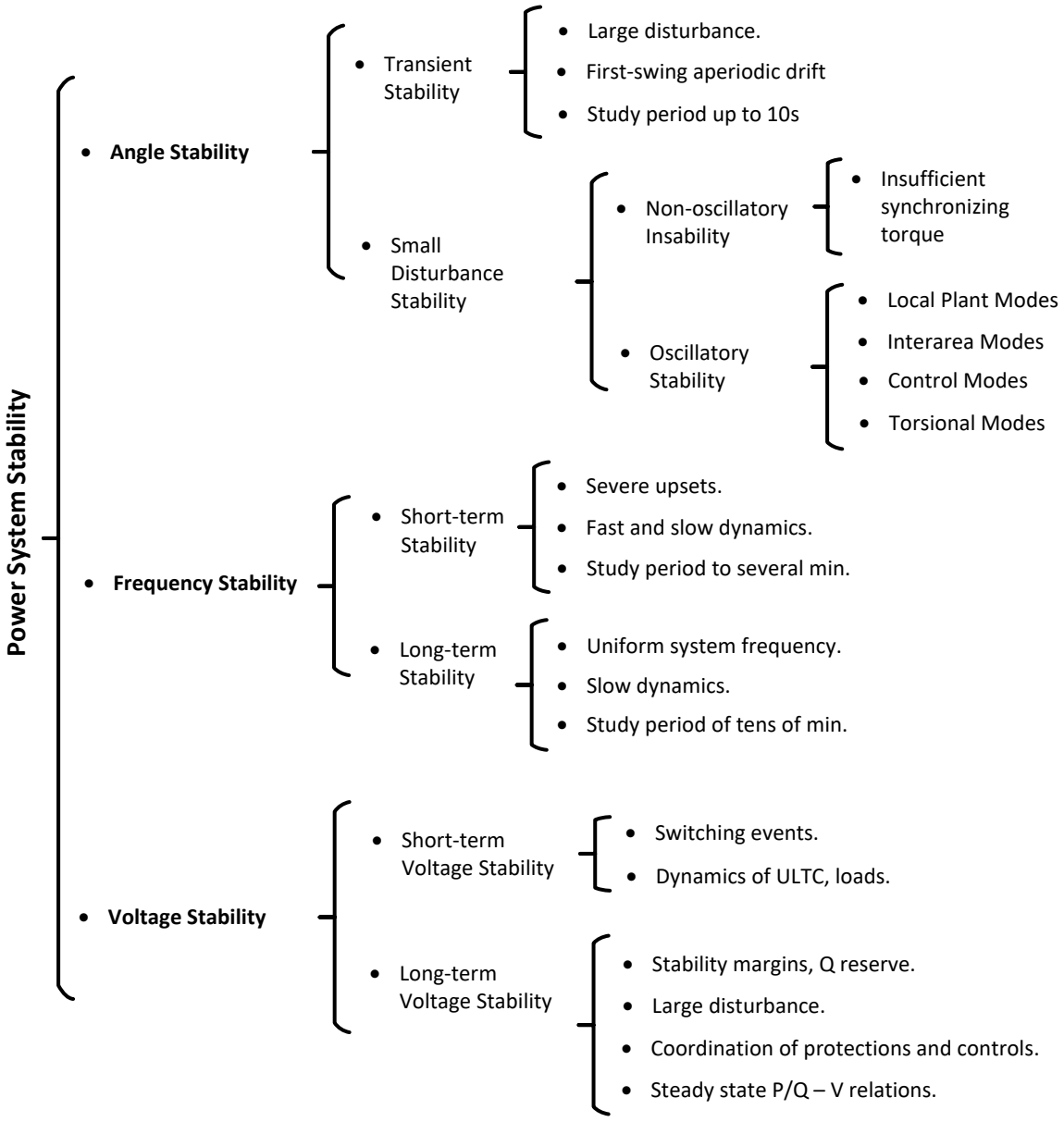

Figure 2.11: Classification of power system stability according to [9], [53].

performed around a nominal operating point of a Differential-algebraic Equations (DAE)

system of the form:

$$\dot{\boldsymbol{z}} = \boldsymbol{\varphi}(\boldsymbol{z}, \boldsymbol{u}) \tag{2.3}$$

$$\mathbf{0} = \boldsymbol{\vartheta}(\boldsymbol{z}, \boldsymbol{u}) \tag{2.4}$$

where $\boldsymbol{z}$ is the vector of state variables; $\boldsymbol{\varphi}$ is a vector of nonlinear functions representing the right-hand side of differential equations, $\boldsymbol{u}$ is a vector of algebraic variables, and $\boldsymbol{\vartheta}$ is a vector of algebraic functions representing algebraic equations. The linearization requires to find the Jacobian matrices of the system of differential and algebraic equations by evaluating the derivatives of $\boldsymbol{\varphi}$ and $\boldsymbol{\vartheta}$, with respect of the state $\boldsymbol{z}$ and algebraic $\boldsymbol{u}$ variables at the operating point $(\boldsymbol{z}(0), \boldsymbol{u}(0))$, which is defined by $\boldsymbol{\varphi}(\boldsymbol{z}(0), \boldsymbol{u}(0)) = 0$ and $\boldsymbol{\vartheta}(\boldsymbol{z}(0), \boldsymbol{u}(0)) = 0$. The linearized model can be expressed as a system of Ordinary Differential Equations (ODE) system of the form:

$$\Delta\dot{\boldsymbol{z}} = D_z\Phi \mid_o \Delta\boldsymbol{z} \tag{2.5}$$

$$D_z\Phi \mid_o = D_z\boldsymbol{\varphi} \mid_o - D_u\boldsymbol{\varphi} \mid_o D_u\boldsymbol{\vartheta} \mid_o^{-1} D_z\boldsymbol{\vartheta} \mid_o \tag{2.6}$$

where $D_z\Phi \mid_o$ is the Jacobian of the ODE system, and $D_z\boldsymbol{\varphi} \mid_o$, $D_u\boldsymbol{\varphi} \mid_o$, $D_u\boldsymbol{\vartheta} \mid_o$, and $D_z\boldsymbol{\vartheta} \mid_o$ are the respective Jacobian matrices of the linearized DAE system. The eigenvalues of $D_z\Phi \mid_o$ are used to analyze the small-signal stability of the system. Power flow analysis is used as the based to obtain the system operating point or equilibrium point.

In this thesis, the focus of the stability problem when BESSs operate connected to a power grid will be on the transient stability domain. For this purpose, the preferred technique to study transient stability is time domain simulations. This requires the definition of suitable models for the system components, and the use of numerical integration techniques, such as the trapezoidal method, to obtain numerical solutions of the differential equations of the models. This approach allows capturing the non-linearity of the component models and controller actions, which is an advantage over alternative approximate methods, such as the Equal Area Criterion or the use of Lyapunov functions.

2.4.2 Frequency Regulation

Frequency regulation refers to the control actions performed on generators and other grid participants, such as ESS, to adjust their power injections to maintain a continuous balance between generation and demand. When such imbalances occur, the rotors of generators, which store kinetic energy, tend to accelerate or decelerate depending on the size and

nature of the imbalance (e.g., loss of load, generating trips, faults, etc.), changing their speed and, thus, the frequency of the voltage generated at their local buses. The speed deviation of individual generating units can be calculated as follows [9]:

$$\frac{d\hat{\omega}_r}{dt} = \frac{1}{2H}\left(\hat{T}_m - \hat{T}_e - K_D\hat{\omega}_r\right) \tag{2.7}$$

where $\hat{\omega}_r$ is the rotor speed in p.u.; $\hat{T}_m$ and $\hat{T}_e$ are the mechanical and electrical torques of the machine in p.u., respectively; K_D is a coefficient to represent damping torque in p.u.; and H is the inertia constant of the machine in MWs/MVA. A further approximation of this equation considers electrical and mechanical power instead of torques. Notice that in (2.7), the per-unit rotor speed is equivalent to the frequency $\hat{f}$ in p.u. The total system frequency deviation $\Delta\hat{f}$ can be approximated by adding the inertia constant of all rotating machines and neglecting the electrical system as follows:

$$\frac{d\Delta\hat{f}}{dt} = \frac{1}{2H_{sys}}\left(\Delta\hat{P}_m - \Delta\hat{P}_L - D\Delta\hat{f}\right) \tag{2.8}$$

where $\hat{f}$ is the system frequency in p.u.; $\hat{P}_m$ is the total system generation in p.u.; $\hat{P}_L$ the total system load in p.u.; D is the load damping factor in p.u., and H_{sys} is the total system inertia in s. In (2.8), the speed at which the frequency changes due to changes in load or generation depends on the system inertia; therefore, systems of large inertia are desirable for frequency control purposes.

When the frequency deviates from its nominal value, most generators are equipped with a proportional control that uses a feedback of the rotor speed in the governor path, to adjust their mechanical power in proportion to the magnitude of the frequency deviation and gain known as the regulation characteristic R, with 1/R representing the droop. This control action action is referred as PFR, and its main objective is to arrest the frequency change, and also distribute the frequency regulation requirements among all generators in proportion of their size. Once the frequency has been stabilized at a value different from its nominal, a secondary control action is performed by some generators, which operate on Automatic Generation Control (AGC), to bring the frequency back to its nominal value. SFR is performed by integrating the speed deviation in an additional PI controller that adjusts the power reference of generators, as shown in Figure 2.12. Tertiary control is also possible, which aims to restore the system to its initial conditions, ensuring also reserves.

ESSs and particularly BESSs are suitable to provide PFR and SFR services, due to their fast time response. In this thesis, the use of BESS to provide regulation services is investigated, assuming distributed and bulk BESSs connected in power grids.

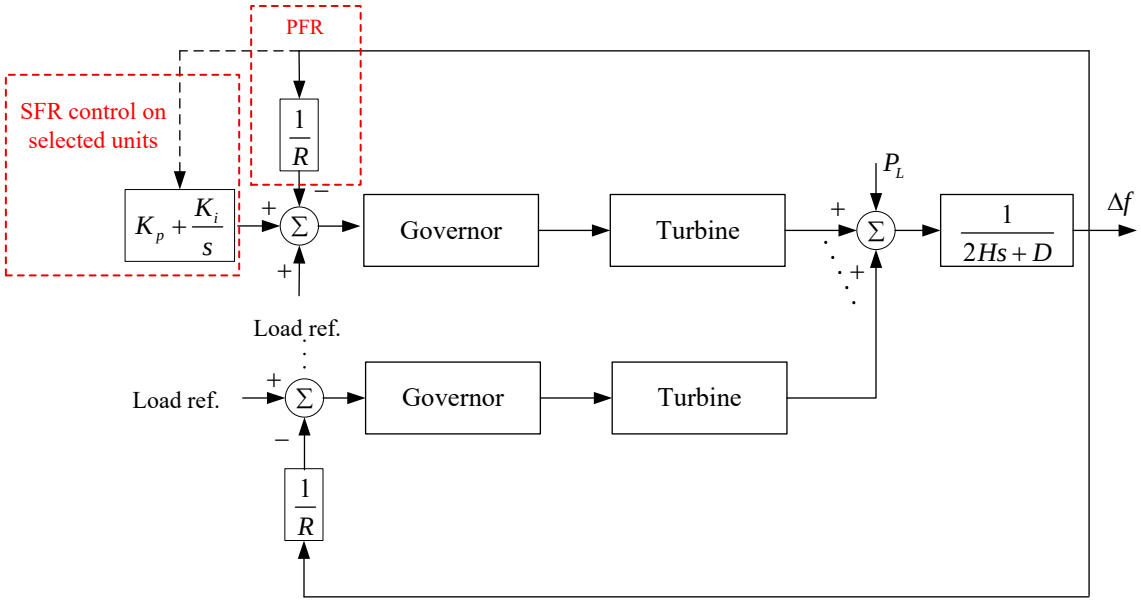

Figure 2.12: Primary and secondary frequency control in generators [9].

2.5 Summary

In this chapter, the main background topics related to this thesis were covered. Thus, an overview of ESS and the different storage technologies were presented. Also, a typical topology and main components of BESS were described. Then, an overview of the main methods and tools that will be used to develop the proposed black-box aggregate BESS models were presented, including AI-based tools such as NN, NARX NN, and GA. Finally, the concept of system stability (voltage stability, transient stability and frequency stability) and frequency regulation were discussed, which are relevant to the electrical studies performed for BESS in the subsequent chapters.

Chapter 3

Dynamic Modelling of Battery Energy Storage Systems and Their Controls

In the first part of this chapter, an average BESS model is developed, including a control strategy that allows it to provide several grid services and operate in different modes, namely frequency regulation, oscillation damping, constant active and reactive power, constant power factor, voltage regulation, and a combination of these. In the second part, the proposed models are used to study them in test systems. Thus, the average model is first validated against the detailed model, when connected to an infinite bus for step changes in power injections, and also when several medium-size BESS are distributed in the load buses of the WSCC 9-bus benchmark test system, while providing frequency regulation. Finally, the validated average model is used to simulate a bulk BESS facility to demonstrate its potential to provide grids services, including voltage and frequency regulation, and oscillation damping, for different levels of degradation of the battery cells. The need for considering the dc-to-dc converter in the model is demonstrated here, considering the impact of aged batteries on the stability of the system. The simulations also allow to show the benefits of BESS with the control systems proposed in this thesis.

3.1 Models of BESS Components

A BESS comprises several electrochemical cells connected in different configurations, bidirectional buck-boost converters (dc-to-dc converter), VSCs (dc-to-ac converter), filters at

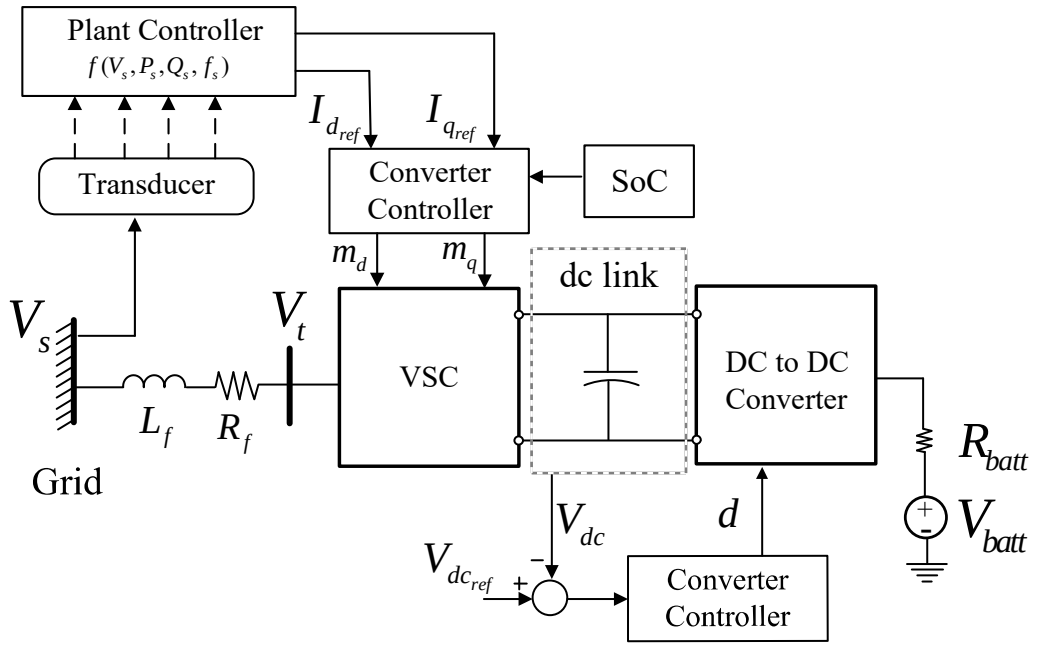

Figure 3.1: Block diagram of the BESS complete model for each VSC and dc-to-dc converter.

the Point of Common Coupling (PCC) to the grid, as discussed in Section 2.2, plus the respective controls for each converter [54], as depicted in Figure 3.1. As illustrated in Figure 3.2, a large scale BESS is modeled as N_c identical VSCs connected in parallel sharing the same amount of active and reactive power [1]. Each individual VSC has its own filter, and is fed at its dc side by M_c equally-sized dc-to-dc bi-directional buck-boost converters connected in parallel, which share the converter's power [48]. Note that since this thesis concentrates on average models, which neglects the switching effects of the converters, the dc-to-dc converters in Figure 3.2 are not interleaved.

The models and controls of the VSC, presented next, are developed for one of the N_c VSCs; hence, the total power of the BESS is equal to the output power of one VSC multiplied by N_c. Likewise, the active power supplied by each dc-to-dc converter is equal to the BESS power divided by the multiplication of N_c and M_c. The model proposed here is a single-line fundamental-frequency equivalent model with a dq reference frame controller that can be readily integrated in power system simulation packages for dynamic studies.

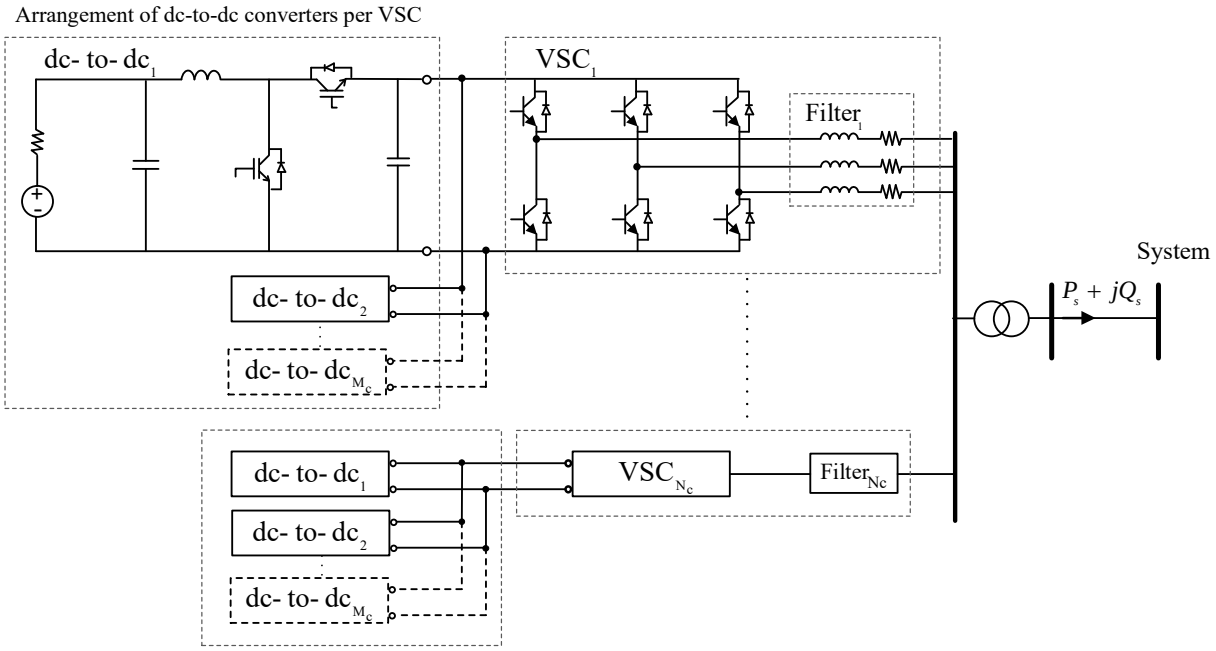

Figure 3.2: BESS topology.

3.1.1 Battery Bank

The battery bank module comprises battery cells connected in series and parallel to achieve the desired voltage and power at each dc-to-dc converter. Here, a simple model comprising a voltage source V_{bat} in series with a resistor R_{bat} is considered [14], [55], as illustrated in Figure 3.1. These two parameters have been used in [14] for dynamic studies, and are hence used here to approximately represent battery degradation due to aging, where a low battery voltage and large resistance signify a degraded battery.

3.1.2 Dc-to-dc Converter Model

An average model per switching period of the bi-directional buck-boost converter depicted in Figure 3.3, is considered. When this converter operates in boost mode (discharging mode), the magnitude of the current I_{dc} representing the VSC load at its terminals is positive, and is negative when it operates in buck mode (charging). The duty ratios d and d_{buck} of the boost SW_{boost} and buck SW_{buck} switches, respectively, are controlled by complementary signals, i.e., $d + d_{buck} = 1$. Finally, it is assumed that the converter's inductor

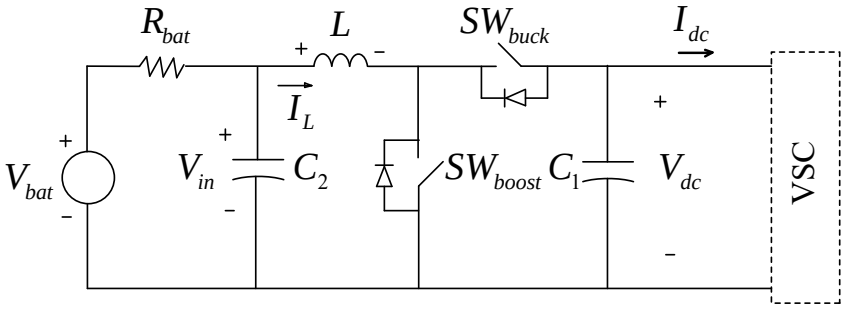

Figure 3.3: Bi-directional buck-boost converter circuit [56].

L always operates in continuous conduction mode. Thus, the average per-switching period of the bi-directional buck-boost converter can be obtained as follows, for the converter operating in boost mode (discharging), based on [56]:

When $SW_{boost} = 1$ (on) and $SW_{buck} = 0$ (off), the converter behaves as illustrated in Figure 3.4(a). The battery bank charges the capacitor C_2 and inductor L, while the capacitor C_1 discharges to supply the load current I_{dc}. As the inductor charges during $0 < t \leq dT_s$, its current grows linearly as shown in Figure 3.4(c). Hence, for $0 < t \leq dT_s$ and $d_{buck}T_s < t \leq T_s$, the resulting state-space model of the converter is:

$$\frac{d}{dt}\begin{bmatrix} V_{in} \\ V_{dc} \\ I_L \end{bmatrix} = \begin{bmatrix} -\frac{1}{C_2 R_{bat}} & 0 & -\frac{1}{C_2} \\ 0 & 0 & 0 \\ \frac{1}{L} & 0 & 0 \end{bmatrix} \begin{bmatrix} V_{in} \\ V_{dc} \\ I_L \end{bmatrix} + \begin{bmatrix} \frac{1}{C_2 R_{bat}} & 0 \\ 0 & -\frac{1}{C_1} \\ 0 & 0 \end{bmatrix} \begin{bmatrix} V_{bat} \\ I_{dc} \end{bmatrix} \tag{3.1}$$

When $SW_{boost} = 0$ (off) and $SW_{buck} = 1$ (on), the converter behaves as illustrated in Figure 3.4(b). In this mode, during $dT_s < t \leq T_s$, the inductor sees the negative voltage $V_{in} - V_{dc}$ at its terminals ($V_{in} < V_{dc}$), and thus discharges, as shown in Figure 3.4(c). The capacitor C_2 discharges, while C_1 charges from the inductor current. Hence, for $dT_s < t \leq T_s$ and $0 < t \leq d_{buck}T_s$, the resulting state-space model of the converter is:

$$\frac{d}{dt}\begin{bmatrix} V_{in} \\ V_{dc} \\ I_L \end{bmatrix} = \begin{bmatrix} -\frac{1}{C_2 R_{bat}} & 0 & -\frac{1}{C_2} \\ 0 & 0 & \frac{1}{C_1} \\ \frac{1}{L} & -\frac{1}{L} & 0 \end{bmatrix} \begin{bmatrix} V_{in} \\ V_{dc} \\ I_L \end{bmatrix} + \begin{bmatrix} \frac{1}{C_2 R_{bat}} & 0 \\ 0 & -\frac{1}{C_1} \\ 0 & 0 \end{bmatrix} \begin{bmatrix} V_{bat} \\ I_{dc} \end{bmatrix} \tag{3.2}$$

where the parameters and variables are defined in the Nomenclature section. Calculating the average per switching period T_s of (3.1) and (3.2), since on average $\dot{\tilde{\boldsymbol{z}}} = d\ \boldsymbol{\vartheta_1}(\boldsymbol{z}) +$

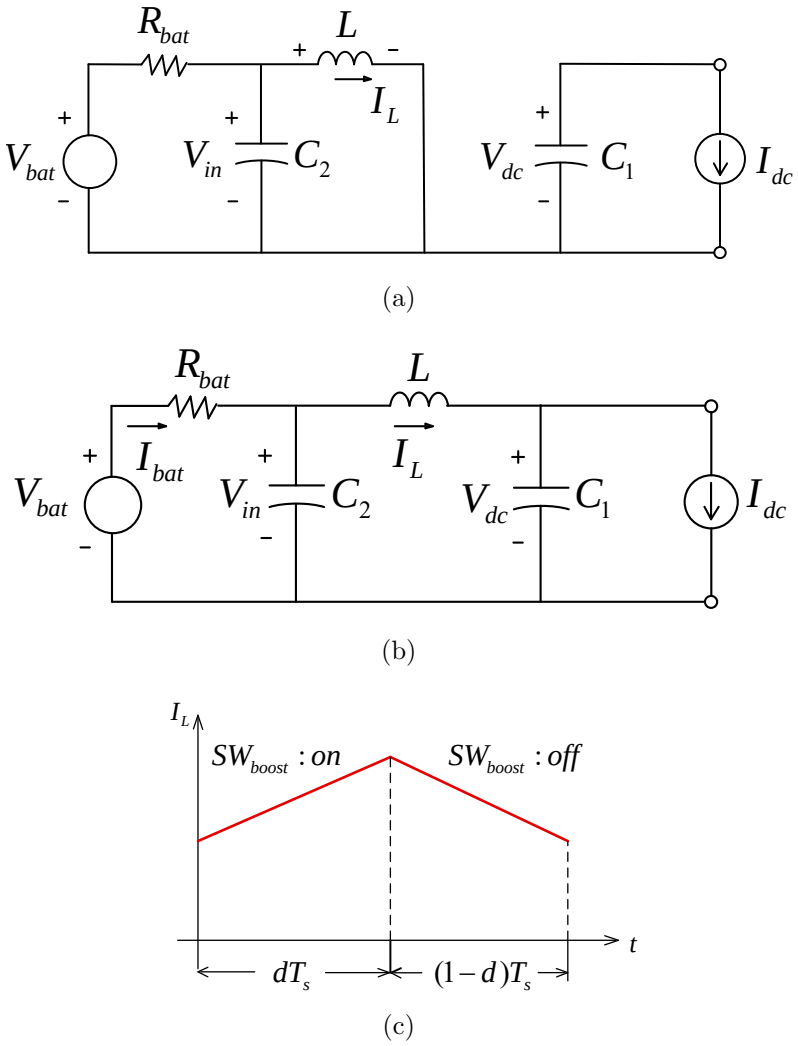

Figure 3.4: Equivalent bi-directional buck-boost converter when operating in boost mode and (a) SW_{boost}=1, (b) SW_{boost}=0, and (c) inductor current.

$(1-d)\boldsymbol{\vartheta_2}(\boldsymbol{z})$, where $\boldsymbol{z} = [V_{in}\ \ V_{dc}\ \ I_L]^T$, and $\boldsymbol{\vartheta_1}$ and $\boldsymbol{\vartheta_2}$ are the right-hand-side of (3.1) and (3.2), respectively, it follows that:

$$\dot{\overline{V}}_{in} = -\frac{1}{C_2 R_{bat}}\overline{V}_{in} - \frac{1}{C_2}\bar{I}_L + \frac{1}{C_2 R_{bat}}V_{bat} \tag{3.3}$$

$$\dot{\overline{V}}_{dc} = \frac{1-d}{C_1}\bar{I}_L - \frac{1}{C_1}I_{dc} \tag{3.4}$$

$$\dot{\bar{I}}_L = \frac{1}{L}\overline{V}_{in} - \frac{1-d}{L}\overline{V}_{dc} \tag{3.5}$$

where the bar on top of a variable signify an average value. Assuming a lossless VSC and neglecting the ac filter losses, I_{dc} can be calculated as follows:

$$I_{dc} = \frac{P_s}{N_c M_c \overline{V}_{dc}} \tag{3.6}$$

where P_s is the power injected by the BESS. Note that the same model can be used when the converter operates in buck mode (charging), the only difference being that I_{dc} is a negative current, as active power flows from the VSC to the dc-to-dc converter to charge the batteries.

3.1.3 Voltage Source Converter Model

The dq components of the peak phase-to-ground terminal voltage V_t of a pulse-width modulated three-phase full bridge VSC, at fundamental frequency, can be calculated as [57]:

$$V_{t_d} = \frac{1}{2}m_d\overline{V}_{dc} \tag{3.7}$$

$$V_{t_q} = \frac{1}{2}m_q\overline{V}_{dc} \tag{3.8}$$

where V_{t_d} and V_{t_q} are the d- and q-axis components of V_t; m_d and m_q are the d- and q-axis of the VSC's modulation index m; and $\overline{V}_{dc}$ is obtained from the dc-to-dc converter average model discussed in Section 3.1.2. The dynamics of the filter, including the step-up transformer connecting the VSC to the electrical grid, can be modeled by the following dq equations [57]:

$$L_f\dot{I}_d = V_{t_d} - V_{s_d} - R_f I_d + \omega_o L_f I_q \tag{3.9}$$

$$L_f \dot{I}_q = V_{t_q} - V_{s_q} - R_f I_q - \omega_o L_f I_d \tag{3.10}$$

where I_d and I_q are the direct- and quadrature-axis components of the peak value of the current injected by the VSC to the grid, respectively; ω_o is the nominal angular frequency in rad/s; V_{s_d} and V_{s_q} are the d- and q-axis components of the voltage V_s at the PCC; L_f and R_f are the inductance and resistance of a first-order filter and transformer used to connect the VSC to the grid Figure 3.1.

Assuming a lossless converters and filter, the total active and reactive power injected by the N_c converters can be calculated as follows, considering that the decoupled dq control forces $V_{s_q} = 0$:

$$P_s = \frac{3}{2} I_d V_{s_d} N_c \tag{3.11}$$

$$Q_s = -\frac{3}{2} I_q V_{s_d} N_c \tag{3.12}$$

From (3.6) and (3.11), the current flowing through the dc link of the VSC can be calculated as a function of the d-axis component of the current injected by the BESS, as follows:

$$I_{dc} = \left(\frac{3 V_{s_d}}{2 M_c \bar{V}_{dc}} \right) I_d \tag{3.13}$$

3.2 Controls

A two-level hierarchical control strategy for the BESS is proposed in this thesis. In the first level, referred here as plant controller, the set points for the BESS' active and reactive power injections are calculated, which are then equally split and passed to N_c individual identical modules in the second level, each comprising a VSC, its current controller, and M_c dc-to-dc converters associated with each of the N_c corresponding VSCs, as depicted in Figure 3.5. Hence, a single average VSC with its current control is modeled to represent all VSCs connected in parallel, as well as a single dc-to-dc converter with its control represents the parallel dc-to-dc converters, whose loading is defined by (3.6). In the end, the total BESS active and reactive power are calculated using (3.11) and (3.12). The VSCs are controlled to regulate the active and reactive power injected, whereas the dc-to-dc converter regulates the dc link voltage.

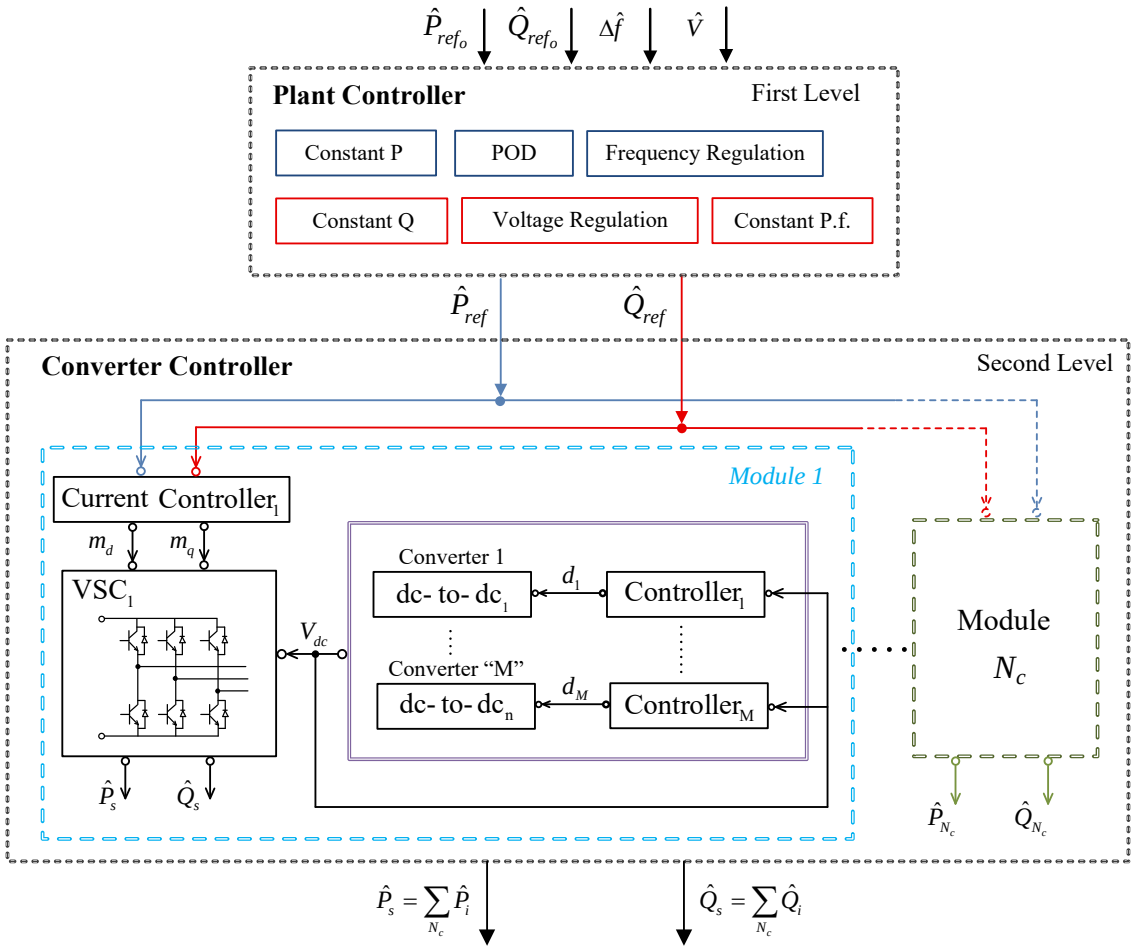

Figure 3.5: Proposed two-level hierarchical control for BESS in p.u.

3.2.1 Plant Controller

The plant controllers depicted in Figures 3.6 and 3.7 provide the active and reactive power references to the current controller, depending on the operation mode of the BESS, i.e., frequency regulation, voltage support, etc. The models proposed in this section are in principle based on those presented in [17] and [20], but with the following considerable differences: the proposed models allow the BESS to provide oscillation damping, secondary frequency regulation, and voltage regulation, or a combination of these; and only two flags FL_P and FL_Q are used to choose the BESS operational mode, as opposed to the five flags used in [20].

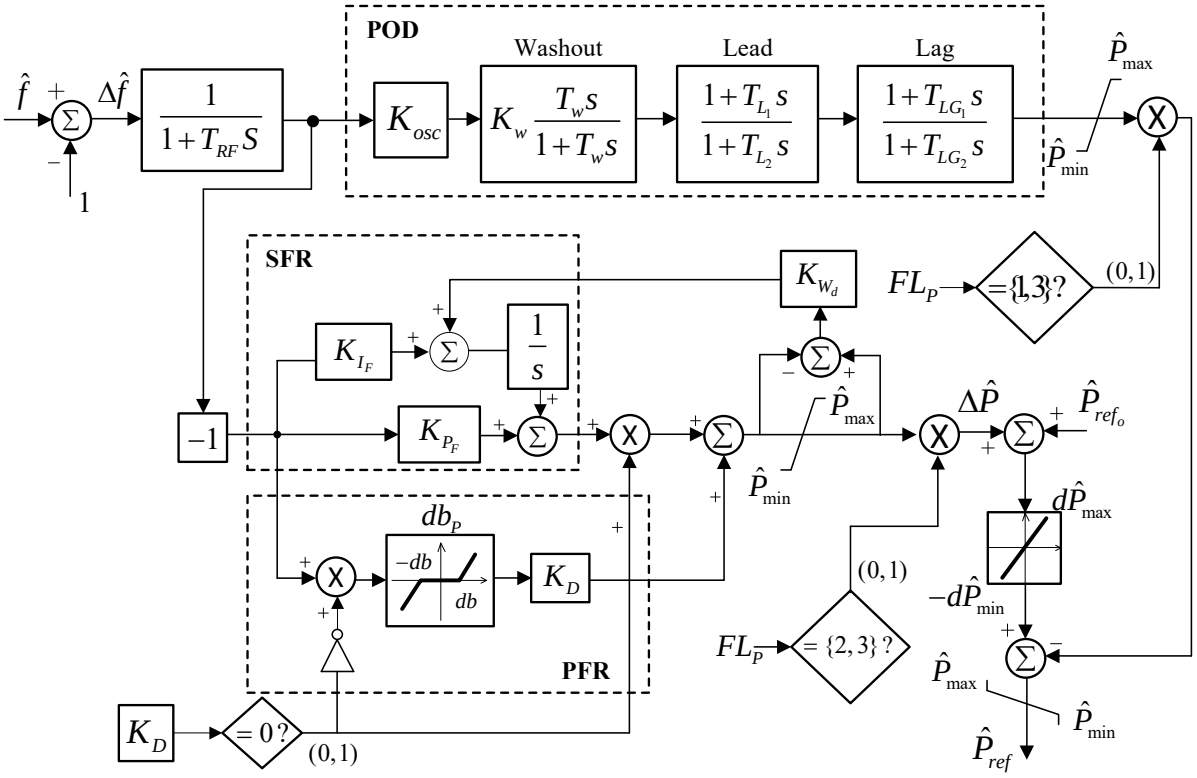

Figure 3.6: Proposed control for constant P, damping oscillation, frequency regulation, and/or damping oscillation plus frequency regulation.

Active Power Control

The active power controller allows the BESS to provide frequency regulation, oscillation damping, and constant active power; in this last mode of operation, the BESS can follow a power reference, which can be specified independently. Unlike the models in [17] and [20], besides a constant frequency droop control, the model proposed here allows SFR. Two main control branches are proposed in the active power controller depicted in Figure 3.6: one for frequency regulation and another for the Power Oscillation Damping (POD) control. $\widehat{P}_{ref}$ is the power reference in p.u. of the BESS nominal power S_b, which is passed to the current controller discussed later, and is equal to the summation of the initial active power reference $\widehat{P}_{ref_o}$ obtained from the solution of the power flow, plus the incremental powers $\pm\Delta\widehat{P}$ coming from the frequency regulation and oscillation damping control branches. A

rate-of-change limiter is used in the frequency-regulation control path to limit the operation of the BESS when providing frequency regulation.

Both the frequency regulation control and the POD control use the p.u. measured frequency signal $\Delta\hat{f}$ as input. A first-order transfer function with time constant T_{RF} models a frequency transducer, which acts as a filter for high frequency $\hat{f}$ p.u. values. The POD control allows the BESS to add damping torque to the system, by injecting active power in phase with $-\Delta\hat{f}_{osc}$ [58], the latter being the target undamped system's frequency component, due to generators oscillating. This control branch comprises a gain K_{OSC}, a washout filter, and a lead-lag compensator. The lead-lag blocks can be tuned to compensate for the phase shifts introduced by dynamic components in the active power control path, between the input signal $\Delta\hat{f}$ and the output power at the BESS terminals $\Delta\hat{P}_s$, at the target frequency, i.e., frequency filter, washout filter, and current control (discussed later). The gain K_{osc} is used to adjust the contribution of POD in the BESS output power, and the washout filter, which is a high-pass filter, prevents the POD from operating during a sustained frequency deviation, and not interfering with frequency regulation control. Limits are added at the end of the POD branch to restrict its contribution to the BESS total active power.

The frequency regulation control allows PFR and SFR through two sub-branches connected in parallel. The PFR branch includes a dead-band to reduce the sensitivity of the controller, and a droop gain K_D. The SFR control is based on a PI controller, with proportional gain K_{P_F} and integral gain K_{I_F}, the latter acting to drive the frequency $\Delta\hat{f}$ to zero. An anti-windup controller is considered in this model to prevent the integrator of gain K_{I_F} to accumulate error when the controller limits $\hat{P}_{\max}$ or $\hat{P}_{\min}$ are reached, by feeding back to the input of the integrator block, a signal proportional (gain K_{W_d}) to the difference of the SFR controller's output after and before limits.

In constant active power mode, the input $\hat{P}_{ref_o}$ can be modified externally to follow a signal, and be passed as the actual power reference $\hat{P}_{ref}$ to the current controller. The rate-of-change limiter block constrains the BESS dynamic response when providing frequency regulation or constant active power but does not affect the POD control, to avoid interfering with its tuning, which is very sensitive to blocks adding a phase lag in its path to the BESS output. Note that the proposed active power control structure allows simultaneous operation of frequency regulation, oscillation damping, and constant active power modes, since each controller branch is treated separately and added at a summing point. Maximum and minimum limits $\hat{P}_{\max}$ and $\hat{P}_{\min}$ are included in the plant controller path, before $\widehat{P}_{ref}$ is passed to the current controller.

The control logic for the active power, presented in Figure 3.6, is commanded by FL_P

as shown in Table 3.1. Thus, when $FL_P = 0$, $\widehat{P}_{ref} = \widehat{P}_{ref_o}$ and the oscillation damping and frequency regulation branches are disabled; $\widehat{P}_{ref_o}$ is set externally to operate the BESS at a desired active power level.

Table 3.1: Active Power Modes

FL_P	Mode
0	Constant P
1	POD
2	PFR and SFR
3	POD, PFR, and SFR

The POD controller is active when $FLGP = 1$, changing $\widehat{P}_{ref}$ by $\pm\Delta\widehat{P}$ as required to damp the low-frequency oscillations in the system. For $FL_P = 2$, the frequency regulation branch is active, while the oscillation damping branch is inactive. The SFR control is active when $K_D = 1/R = 0$, and inactive when $K_D \neq 0$. Finally, for $FL_P = 3$, the oscillating damping branch and the frequency regulation branch are activated at the same time, allowing the simultaneous operation of the BESS in both modes.

Reactive Power Control

Three operational modes are available for reactive power control, which are independent from the operational modes of the active power control, and implemented through selector blocks that operate based on the value of the reactive power flag FL_Q as shown in Table 3.2. Maximum and minimum limits on $\widehat{Q}_{ref}$, $Q_{\max}$ and $Q_{\min}$, respectively, are included in the controller path, before $\widehat{Q}_{ref}$ is passed to the current controller. In constant power

Table 3.2: Reactive power modes of operation

FL_Q	Mode
0	Constant Q
1	Constant power factor
2	Voltage regulation

factor mode, the BESS automatically adjusts its reactive power based on its active power output, so that its power factor remains constant. For this purpose, the reactive power reference $\widehat{Q}_{ref}$ is calculated as the multiplication of the initial ratio $\widehat{Q}_{ref_o}/\widehat{P}_{ref_o}$ times the

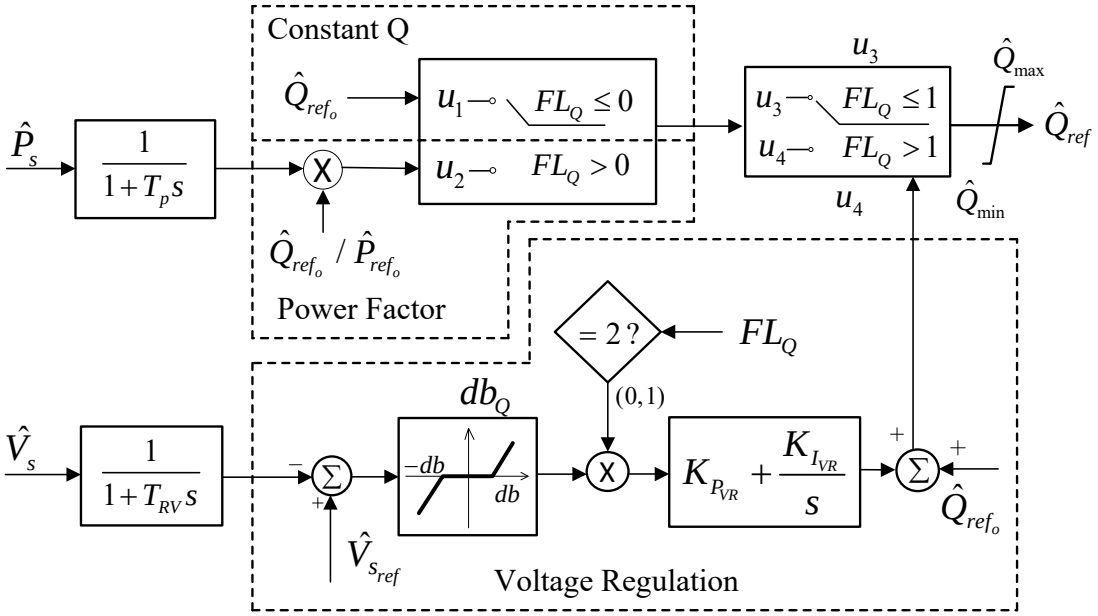

Figure 3.7: Proposed control for constant Q, constant power factor, or voltage regulation.

measured $\widehat{P}_s$, where these are calculated at the initialization of the BESS model, thus ensuring that the initial power factor is maintained by changing $\widehat{Q}_{ref}$ as $\widehat{P}_s$ changes. A power transducer, modeled as a first-order transfer function with time constant T_P, is considered for the measured active power. In constant Q mode, $\widehat{Q}_{ref}$ is equal to $\widehat{Q}_{ref_o}$, which can be varied to operate the BESS at a desired reactive power output.

Finally, voltage regulation at the terminals of the BESS can be provided by a second branch in the reactive power controller. The voltage regulation controller compares a measured terminal voltage $\widehat{V}_s$ to a reference value $\widehat{V}_{s_{ref}}$, and the difference is input to a PI controller to control the voltage at the PCC bus. A deadband block is used to reduce the sensitivity of the controller to small voltage deviations. By properly choosing the controller gains $K_{P_{VR}}$ and $K_{I_{VR}}$, this can be set to operate in droop mode ($K_{I_{VR}} = 0$ and $K_{P_{VR}} \neq 0$), or to regulate the voltage at the a desired value ($K_{I_{VR}} \neq 0$); the droop mode is useful when the BESS operates in parallel with other voltage regulating devices, such as generators.

3.2.2 Current Controller

The VSC is controlled using a decoupled dq current control which is presented in Figure 3.8. A Phase-Locked Loop (PLL) circuit, presented in Figure 3.9 provides a reference angle θ such that the q component of the voltage at the PCC with the electrical grid is zero, i.e., $V_{s_q} = 0$; this allows the decoupling of the active and reactive power injected to the grid. Alternatively, a PLL circuit that has V_{s_q} as input to the summing joint that feeds the error to the PI in Figure 3.9 could be used; however, that option was discarded in this thesis, due to the additional block required to calculate the q-axis component of V_s, since the maximum number of blocks allowed for the model implementation is reached for the average BESS model proposed here (Section 3.3.1). Thus, the dq p.u. quantities are calculated as follows:

$$\widehat{V}_{s_d} = \widehat{V}_s \cos\left(\theta_s - \theta\right) \tag{3.14}$$

$$\widehat{V}_{s_q} = \widehat{V}_s \sin\left(\theta_s - \theta\right) \tag{3.15}$$

$$\hat{I}_d = \hat{I} \cos\left(\theta_s - \theta - \phi\right) \tag{3.16}$$

$$\hat{I}_q = \hat{I} \sin\left(\theta_s - \theta - \phi\right) \tag{3.17}$$

$$\phi = \tan^{-1}\left(\frac{Q_s}{P_s}\right) + \begin{cases} 0 & \text{if } P_s \geq 0 \\ \pi & \text{if } P_s < 0 \end{cases} \tag{3.18}$$

where θ_s and $\widehat{V}_s$ are the angle and p.u. value of the voltage at the PCC bus; $\hat{I}$ is the p.u. current injected by one of the N_c converters; P_s and Q_s are the active and reactive power injected by the BESS into the grid; and ϕ is the power factor angle. The bases for the p.u. calculations in the dq reference frame are as follows:

$$V_b = \sqrt{\frac{2}{3}} V_{nom} \tag{3.19}$$

$$I_b = \sqrt{\frac{2}{3}} \frac{S_b}{N_c V_{nom}} \tag{3.20}$$

The objective of the current controller is to adjust the modulation index m_d and m_q, to control the VSC's terminal voltage $\widehat{V}_t$ and angle θ_t, such that the BESS injected powers $\widehat{P}_s$ and $\widehat{Q}_s$ are equal to $\widehat{P}_{ref}$ and $\widehat{Q}_{ref}$, which are used to calculate $\hat{I}_{d_{ref}}$ and $\hat{I}_{q_{ref}}$. Since the decoupled control forces $V_{q_s} = 0$, the reference currents in dq components can be calculated

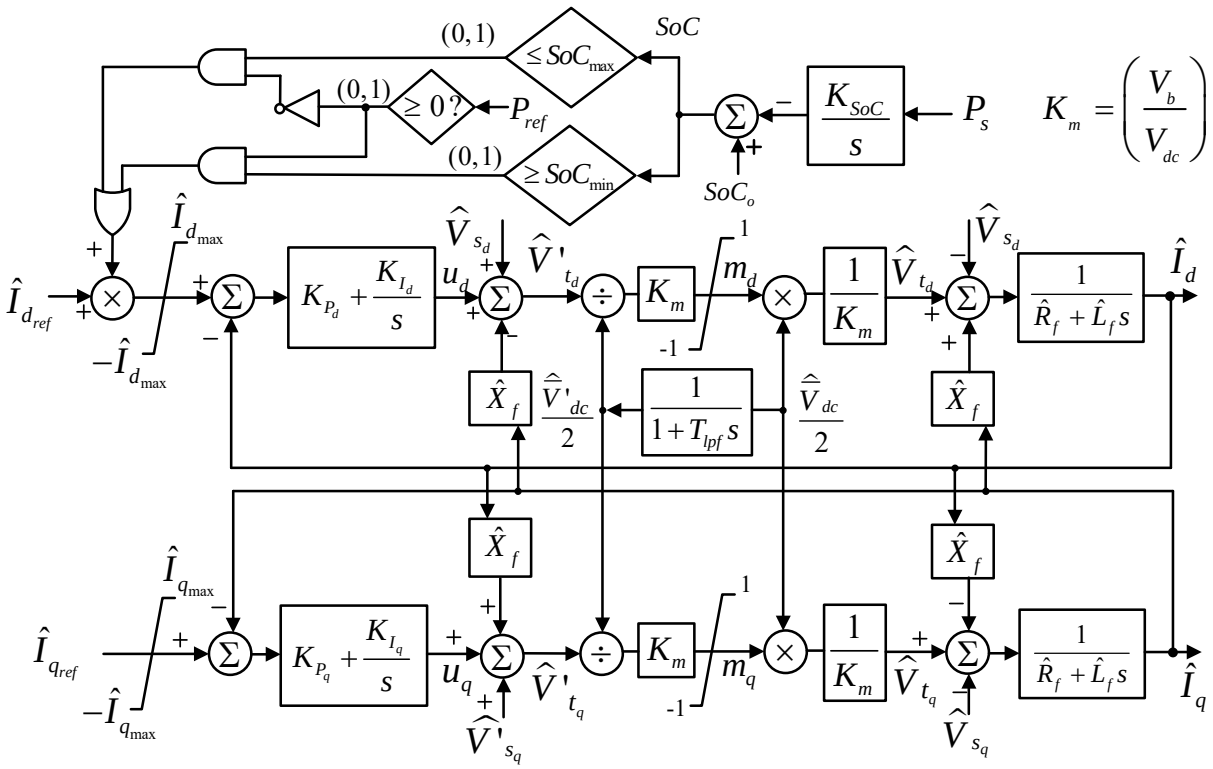

Figure 3.8: Current controller in dq-frame for VSC including the effect of SoC on d-axis current.

as follows, from (3.11) and (3.12):

$$\hat{I}_{d_{ref}} = \frac{\widehat{P}_{ref}}{\widehat{V}_{d_f}} \tag{3.21}$$

$$\hat{I}_{q_{ref}} = -\frac{\widehat{Q}_{ref}}{\widehat{V}_{d_f}} \tag{3.22}$$

Where $\widehat{V}_{d_f}$ is the measurement of $\widehat{V}_d$. The currents $\hat{I}_d$ and $\hat{I}_q$ are compared with $\hat{I}_{d_{ref}}$ and $\hat{I}_{q_{ref}}$ respectively, and the error is passed through PI controllers, the output of which are the variables u_d and u_q. In order to calculate the desired VSC terminal voltages $\widehat{V}'_{t_d}$ and $\widehat{V}'_{t_q}$, feed forward compensation for the filter-plus-transformer inductances and grid voltages $\widehat{V}_{s_d}$ and $\widehat{V}_{s_q}$, which couple the d- and q- axes (see (3.9) and (3.10)), are added to the control signals u_d and u_q; these are used to calculate the VSC modulation indeces in the dq axes,

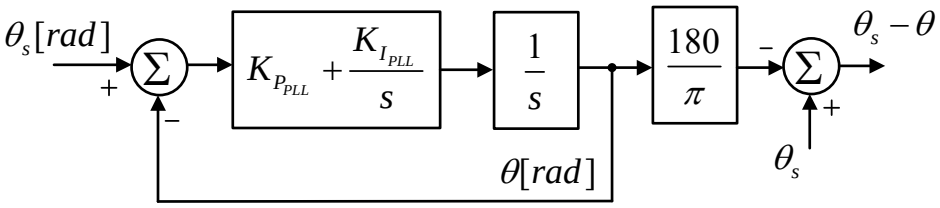

Figure 3.9: Phase locked loop control [59].

m_d and m_q, as follows:

$$\widehat{V}'_{t_d} = u_d - \widehat{X}_f \hat{I}_q + \widehat{V}_{s_d} \tag{3.23}$$

$$\widehat{V}'_{t_q} = u_q + \widehat{X}_f \hat{I}_d + \widehat{V}_{s_q} \tag{3.24}$$

$$m_d = 2\left(\frac{V_b}{V_{dc_b}}\right)\frac{\widehat{V}'_{t_d}}{\widehat{\overline{V}}'_{dc}} \tag{3.25}$$

$$m_q = 2\left(\frac{V_b}{V_{dc_b}}\right)\frac{\widehat{V}'_{t_q}}{\widehat{\overline{V}}'_{dc}} \tag{3.26}$$

where $\widehat{X}_f$ is the reactance of the filter in p.u., the variable $\widehat{\overline{V}}'_{dc}$ is the measured dc link voltage in p.u. and V_{dc_b} is the nominal dc link voltage. The voltage measurement for the dc link is modeled as a low-pass filter with time constant T_{lpf}, so as to eliminate the high-frequency ripple in the dc link [32].

The current converter control logic recommended in [17] for BESS is used here to ensure the BESS operates within its allowed SoC range, as depicted in Figure 3.10. The SoC of the BESS is calculated in Figure 3.8 as the integration of the active power P_s over time, where K_{SoC} is the gain conversion, and SoC_o is the initial SoC. According to the proposed logic, when the SoC is larger than $SoC_{\max}$ and the BESS is operating in charging mode ($\widehat{P}_{ref} < 0$), $\hat{I}_{d_{ref}}$ is forced to zero to prevent the BESS from further charging. On the other hand, if the SoC is less than the $SoC_{\min}$ and the BESS is operating in discharging mode

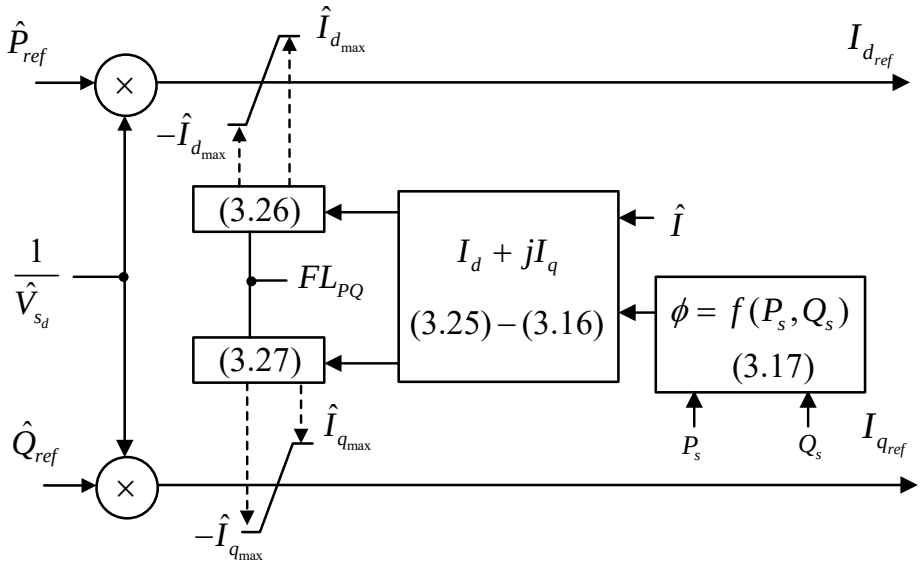

Figure 3.10: Current Limiter.

($\widehat{P}_{ref} > 0$), the $\hat{I}_{d_{ref}}$ is also forced to zero to prevent the BESS from further discharging. If neither of these conditions hold, then $\hat{I}_{d_{ref}}$ passes through to the converter, operating normally. The following limits are imposed on $\hat{I}_{d_{ref}}$ and $\hat{I}_{q_{ref}}$, as proposed in [17], to prevent the BESS from exceeding its rated power:

$$\hat{I}_{d_{max}} = \begin{cases} 1 & \text{if } FL_{PQ} = 1 \\ \sqrt{1 - \hat{I}_q^2} & \text{if } FL_{PQ} = 0 \end{cases} \tag{3.27}$$

$$\hat{I}_{q_{max}} = \begin{cases} 1 & \text{if } FL_{PQ} = 0 \\ \sqrt{1 - \hat{I}_d^2} & \text{if } FL_{PQ} = 1 \end{cases} \tag{3.28}$$

When $FL_{PQ} = 1$, the BESS operates in P priority mode, and when $FL_{PQ} = 0$, it operates in Q priority mode. In the P priority mode, the q current limit is smaller than the d current limit, thus providing more P and less Q outputs, and the opposite in Q priority mode.

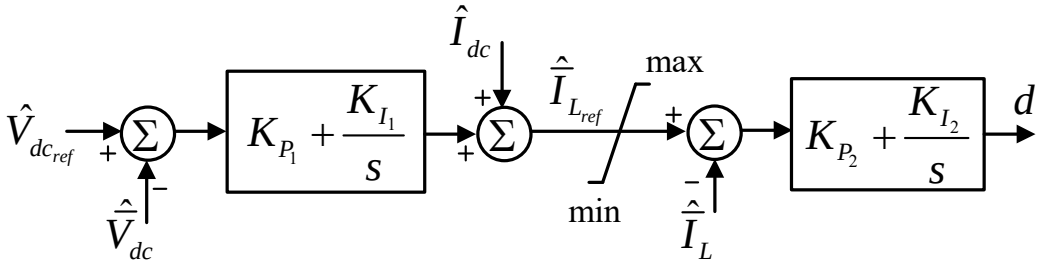

Figure 3.11: Dc-dc converter controller.

3.2.3 Dc-to-dc Converter Controller

The dc-to-dc controller is presented in Figure 3.11. Two PI control blocks are used in cascade, the first compares the dc link voltage with a reference value, and its output (current through C_1) is added to $\widehat{I}_{dc}$, which is calculated using (3.13)) to obtain a reference current thorough the inductor L, which is checked for limits and then is compared with the actual $\widehat{I}_L$. The error of the second summation is passed through the second PI block, the output of which is the duty cycle of the boost switch d. This control prevents the inductor L from being overloaded, which is especially important when the batteries are degraded.

3.2.4 Comparison with Existing Controllers

The proposed control strategy for active and reactive power is primarily based on [17] and [20], where the models discussed and validated with actual data are intended for bulk applications and practical utility-scale studies. The concepts of plant controller, current controller, energy converter model, and their interactions, discussed in [17], are adopted here as plant level controllers. However, the following controllers used within these high level blocks, providing services associated with active and reactive power, are novel contributions, vis-á-vis the controllers discussed in [17] and [20]:

- The POD controller, which includes a transducer to measure frequency and associated limits to prevent battery overloading.
- The SFR, which includes an anti-wind-up control to improve the dynamic response of the BESS when it has reached limits.
- The dq current controller in Section 3.2.2.

- The dc-to-dc converter and associated controls.
- Besides the normal operating modes associated with active power, namely, frequency regulation, oscillation damping, and constant active power, the proposed P control logic allows simultaneous operation in frequency regulation and POD.
- The reactive power controller is simpler, but allows operation of the BESS in the same operating modes, i.e., voltage regulation, constant reactive power, and constant power factor mode.
- The proposed control logic requires less flags.

3.3 Implementation of BESS Model

In this section, the implementation of the average BESS model, proposed in Section 3.1, using a commercial power system analysis software package is discussed. Since the proposed model is validated against detailed simulations, which include the switching effects of the converters, a detailed version of the model was also implemented using Mathworks Simulink®.

3.3.1 TSAT Phasor Model

PowerTech's DSATools® is the commercial software suitable to perform power system analysis, which was used to implement and study the BESS models proposed in this thesis. This package allows to perform dynamic simulations, and provides specific tools to evaluate all forms of stability (transient, voltage, small-signal, and frequency) in power systems. In addition, models can be added to its library, which is convenient as multiple BESS are simulated, to develop the aggregated BESS models, which need to be validated, tested and studied in sample systems. Furthermore, this is a commercial software package that is being used by the Ontario's IESO; as a result, the models developed using this software can be readily used to study Ontario's grid.

The simulations were performed using TSAT®, which is part of the DSATools® power system software package [60]. All BESS models proposed and used in this thesis were implemented as a template User Defined Model (UDM), which allows to readily parametrize the BESS. The base structure used in the UDM is the Modularized Renewable Generator (MRG), which is made available in TSAT® to model renewable generators, such as wind

or photovoltaic farms, but can be modified to implement a BESS. Three of the five sub-modules available in the MRG were used to realize the BESS model depicted in Figure 3.5, i.e., Generator/Converter module, Electrical Controller, and Plant Controller. The Plant Controller module contains the plant controller proposed in Section 3.2.1. The Electrical Controller module includes the current controller, dc-to-dc converter model, and dc-to-dc converter controller, and VSC; thus, it has $\hat{P}_{ref}$ and $\hat{Q}_{ref}$ as inputs, and $\hat{P}_s$ and $\hat{Q}_s$ as outputs. Finally, the Generator/Converter module acts as an interface between the MRG and the grid, thus changing the bases of $\hat{P}_s$ and $\hat{Q}_s$ to a common grid power base.

The model proposed captures most of the relevant dynamics of the dc- and ac- side, that may cause instability to the BESS operation under certain circumstances, which were not properly represented by the models in [17] and [20]. Furthermore, since average models are considered for the converters in the studies performed here, the simulation times are much faster than in detailed models, which require smaller time-steps to capture the high-frequency operation of the converter's switches.

3.3.2 Simulink® Detailed Model

A detailed three-phase BESS model equivalent to the average model proposed in Section 3.1 was implemented in Mathworks' Matlab® and Simulink®, as illustrated in Figure 3.12. In this model, all converter's circuit elements were represented by physical models available in the Simulink's Simscape® library, such as resistors, capacitors, inductors, Insulated-gate Bipolar Transistors (IGBTs) (used as switches), diodes, voltage sources, etc., and the transformer, with its windings' series resistance, leakage reactance, and a magnetization branch, connecting the filter and the PCC. The control systems were implemented using standard available blocks, such as PI blocks, gains, summing blocks, etc. Furthermore, although the control systems remain the same as in the average model, the following modifications were necessary: high-frequency carrier signals to control the switches; three modulating signals with amplitudes m_a, m_b, and m_c, as opposed to the two used in the average model; control and carrier signals for the dc-to-dc converter control; and Park's transformation blocks to convert dq quantities into abc quantities and vice-versa.

The BESS model considers a single VSC and three dc-to-dc converters connected at the dc side. Moreover, the time step required for convergence in detailed simulations is much smaller than that in the average model; thus, a time step of $10\mu s$ was used in the detailed simulations of the BESS in this thesis.

Other advantages of using Mathworks' Matlab® and Simulink®, besides allowing modeling of detailed models, include providing additional tools to perform complementary anal-

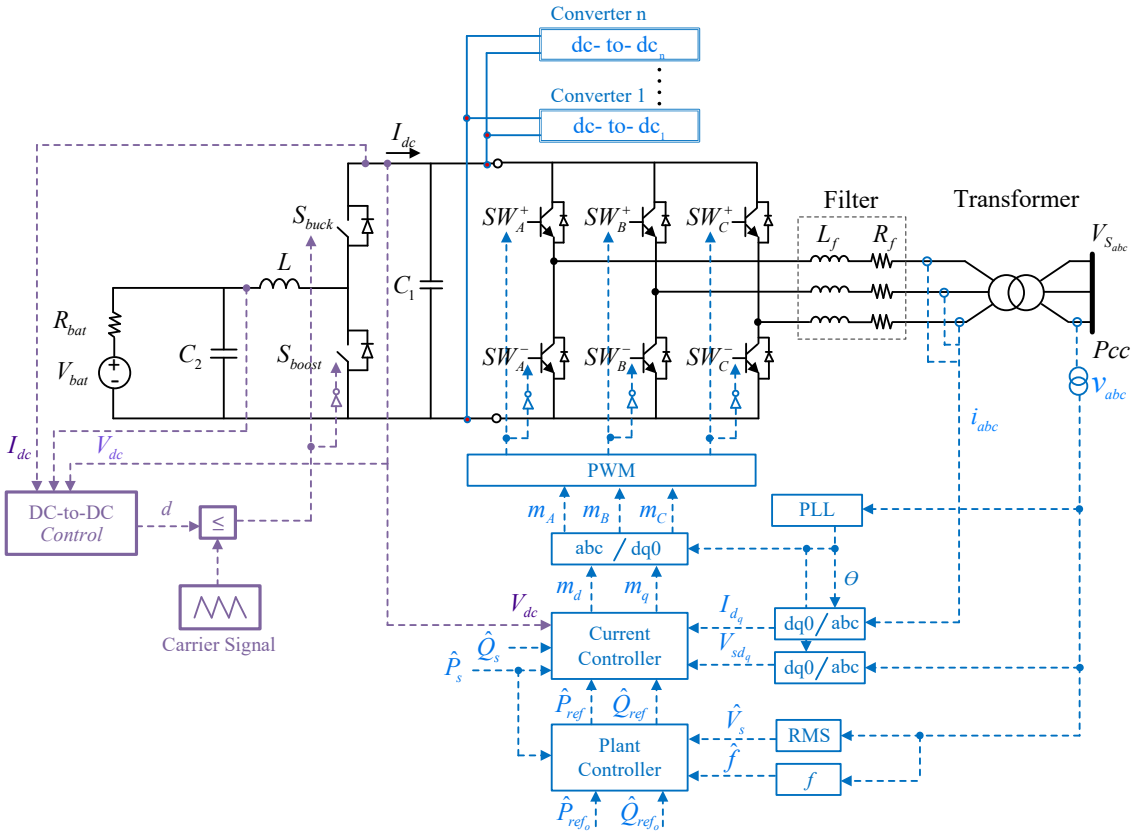

Figure 3.12: Detailed BESS model implemented in Simulink.

ysis, such as system identification, or deploy NNs, optimization, etc., which facilitate the integration of models and techniques proposed in this thesis for power systems.

3.4 BESS Model Validation

In this section, a comparison between the detailed and average BESS models, discussed in Sections 3.1 and 3.2, is presented. Thus, the BESS is first simulated connected to an infinite bus to study its dynamic response to step changes in the power reference and to system disturbances, for both detailed and average models; in this analysis, the limitations of the average model with respect to the detailed model are highlighted. Then, as an application of the models, distributed BESS connected to the load buses of the WECC 9-

bus benchmark test system from [61] are studied for the provision of frequency regulation, comparing the detailed and average BESS models, and demonstrating that average models are less accurate when BESS limits are reached. It is also shown that, given their fast response, the frequency regulation of the system can be considerably improved by small-sized BESSs at load buses, which have the additional advantage of improving the load voltages, due to the capability of BESS to regulate voltage, as well.

3.4.1 BESS Configuration and Model Parameters

A 1.5 MVA/2 MWh BESS is considered in this thesis, which is based on an existing facility of Wind and Energy Canada (WeiCAN) [62]. This facility comprises a 1.5 MVA VSCs supplied by three equally-sized dc-to-dc converters, only two of which are currently active, thus giving the facility a net output power of 1 MW. The main BESS parameters were obtained from this facility, including the step-up transformer's impedance, which raises the voltage from 480 V to 13.8 kV, the filter impedance, the VSC rating, and dc-to-dc converter parameters and ratings. The impedance of the step-up transformer is added to the filter impedance in the model, for simplicity.

For the battery bank, battery cells of 4.8 Ah, 4.0 V, and 25 mΩ [63], operating at 0.7C, were arranged in series and parallel to match the low-voltage nominal side of the dc-to-dc converter and its power rating of 500 kW, as depicted in Figure 3.13, which resulted in an equivalent circuit with $V_{bat} = 500$ V and $R_{bat} = 0.01$ Ω as parameters. Note that the BESS model does not keep track of the SoC in the battery bank model, but in the current controller, as depicted in Figure 3.8. In addition, the battery bank model does not consider the effect of SoC on V_{bat} or R_{bat}; however, the SoC is used in the current controller to stop the BESS charging when the battery cells are fully charged, modeled as $SoC = SoC_{\max}$, or to stop discharging when it is fully discharged, i.e., $SoC = SoC_{\min}$.

All the BESS's PI controllers were tuned by trial and error to obtain adequate dynamic responses. Switching frequencies of 8 kHz and 2 kHz were used in the detailed model for the dc-to-dc converter and VSC, respectively. The model parameters are summarized in Table 3.3, where the parameter values for the POD controller are described in detail later in Section 3.5.3.

3.4.2 BESS Connected to an Infinite Bus

The BESS connected to an infinite bus through a step-up transformer, as depicted in Figure 3.14, rises the voltage from 13.8 kV at the terminals of the BESS to 230 kV, at

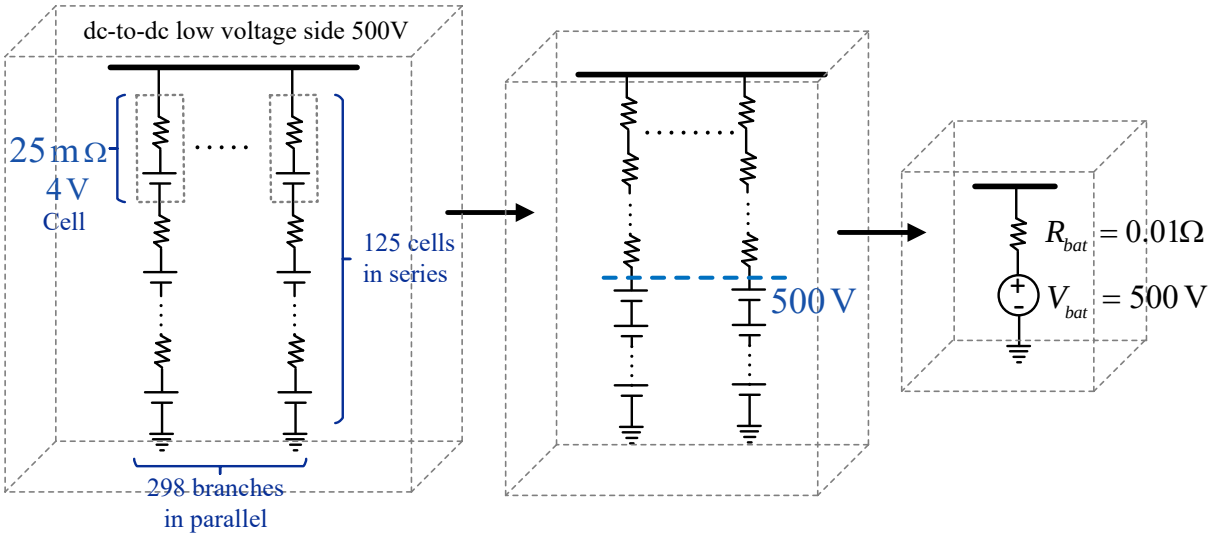

Figure 3.13: Battery bank's equivalent circuit.

Table 3.3: 1.5 MVA BESS Parameters

Generator Converter					
Parameter	Value	Parameter	Value	Parameter	Value
S_b[MVA]	1.5	V_{nom}[V]	480	V_{dc_b}[V]	900
K_D	500	K_{I_F}	2000	K_{P_F}	3000
K_W	1	T_W[sec]	0.031	T_{L_1}[sec]	0.1
T_{L_2}[sec]	0.068	T_{LG_1}[sec]	0	T_{LG_2}[sec]	0
T_P[sec]	0.02	T_{RV}[sec]	0.02	T_{RF}[sec]	0.02
db_P	0.0001	$K_{I_{VR}}$	150	$K_{P_{VR}}$	35
$dP_{\max}$	0.5	K_{osc}	2552	$K_{I_{pl}}$	1400
$K_{P_{pl}}$	60	$L_f[mH]$	0.05449	$R_f[m\Omega]$	2
T_{lpf}[sec]	0.008	K_{I_d}	0.07164	K_{P_d}	0.839098
K_{I_q}	0.07164	K_{P_q}	0.839098	N_c	1
M_c	3	$R_{bat}[\Omega]$	0.01	V_{bat}[V]	500
L[H]	0.0003	C_1[F]	0.033	C_2[F]	0.0051
K_{I_1}	296.4157	K_{P_1}	8.2048	K_{I_2}	65.5791
K_{P_2}	0.2567	db_Q	0.0001		

the transmission level. The grid is represented by the impedance $Z_{eq} = R_{eq} + jX_{eq}$, which

is the Thevenin's impedance of the WSCC 9-bus test system at Bus 6. The detailed and simplified BESS models are simulated in Matlab's Simulink® for some grid contingencies, and their dynamic response compared.

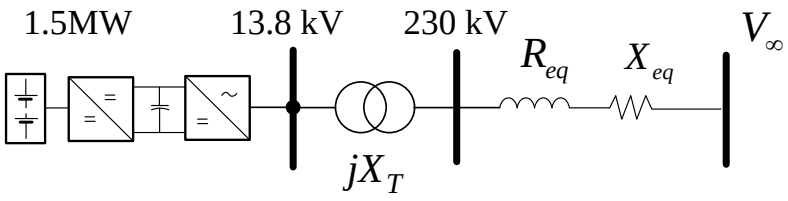

Figure 3.14: BESS connected to an infinite bus trough a step-up transformer.

In the simulated case, the BESS operates in constant PQ mode, i.e., following P_{ref} and Q_{ref}, with step changes in P_{ref} and Q_{ref}. Thus, at $t = 0$s, the BESS is supplying 0.1 MW and 0.1 MVAr, and the following sequence of changes in $\{t, P_{ref}\}$ are simulated: {2s, 1.5 MW}, {6s, -1.5 MW}, and {9s, 1.5 MW}; and in $\{t, Q_{ref}\}$: {3.5s, -0.5 MVAr} and {7.5s, 0.5 MVAr}. Simultaneously, a reduction of 50% in the Thevenin impedance was effected at $t = 3.5$s, followed by a three-phase short-circuit at $t = 7s$ at the point of connection, which is cleared after 50ms. The latter sequence of events allows testing the response of the BESS for extreme conditions.

The results of the simulations are presented in Figures 3.15 to 3.22. As expected, the BESS response is very fast, being able to remain stable after the short circuit, and switch from almost full discharging at 1.5 MW to full charging in less than 1 second. Indeed, a rate-of-change limit of $d\hat{P}_{\max} = \pm 1$ p.u./s was used in the active power control to demonstrate the model functionality, thus the active power injection takes around 1s to reach steady state in Figure 3.15. Notice the effectiveness of the current controller to decouple the BESS active and reactive power injections, which is an advantage to effectively provide independent active- and reactive-power associated services, as also demonstrated later. Also, the large transient in P at around $t = 7s$, observed in Figure 3.15, which momentarily drives the BESS from charging to discharging, creates a sudden change in the dc-to-dc converter load, thus producing also the large transients in the dc link voltage shown in Figure 3.17, which is quickly regulated by the dc-to-dc converter controller. This transient performance can be improved by a more detailed tunning of the controllers' PIs, and/or increasing the size of the dc link capacitor.

Observe that for most of the simulation time, the average and detailed models yield similar results, thus validating the proposed BESS average model. However, some differences arise during the short circuit, from $t = 7s$ to $t = 7.05s$, where larger reactive power

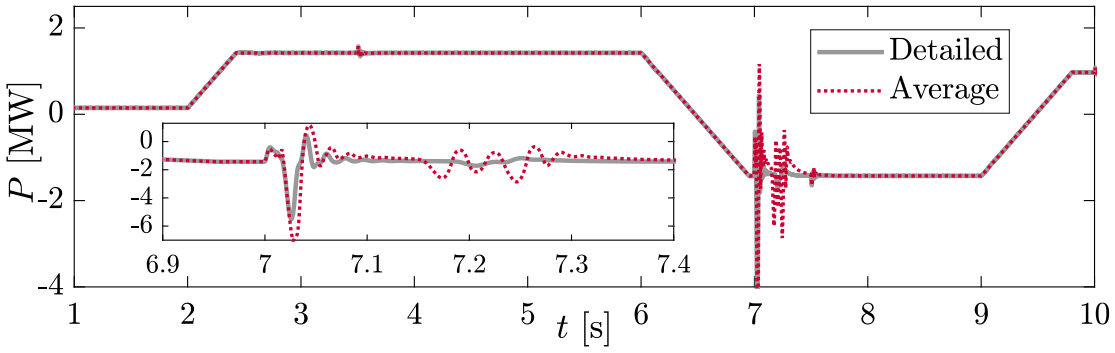

Figure 3.15: BESS active power injected.

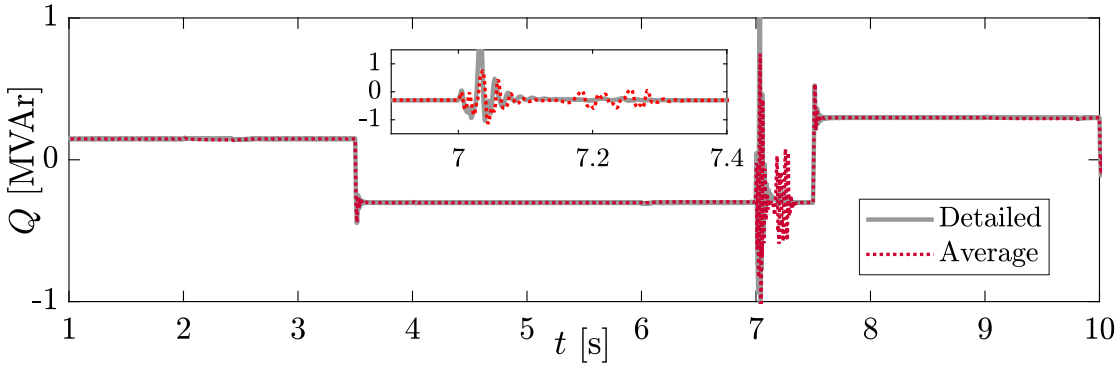

Figure 3.16: BESS reactive power injected.

excursions are observed in Figure 3.16. In this case, the transients of V_{dc} and I_L during the fault in the detailed model are larger than those in the average model, especially in I_L. This forces m_d and $I_{L_{ref}}$ to reach their limits faster in the detailed model, which along with the intrinsic ripple of the detailed model's variables, influence the response of the converters' controllers thereafter; particularly, the integral components of the PI controllers, which accumulate error, end up producing different dynamic response of the controlled variables several milliseconds after the first transients.

The most significant differences between the average and simplified model can be observed during the short-circuit, between $t = 7$s and $t = 7.5$ s. For example, the inductor current I_L presents a much larger value in the detailed model, also switching to positive values, as observed in the amplified subplot in Figure 3.19. This activates the inductor-current limiter feature of the dc-to-dc controller, and thus creates a difference in the dclink

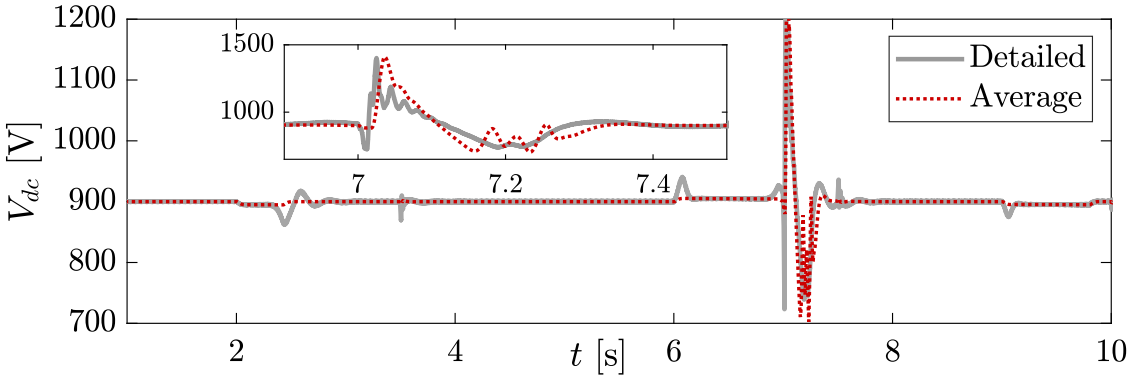

Figure 3.17: Dc-to-dc converter's dc link voltage.

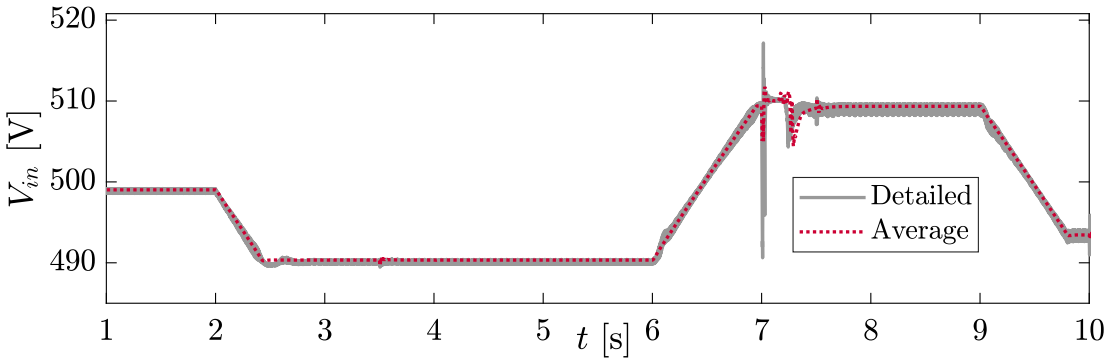

Figure 3.18: Dc-to-dc converter's low-voltage side input voltage.

voltage with respect to the average model (e.g., the small oscillations at around 7.2 s, observed in the average model, are not evident in the detailed model), which propagates to the rest of the model variables. Indeed, the large positive current excursion in I_L during the short-circuit has a resetting effect in the second PI of the dc-to-dc converter controller of the detailed model, which, in the case of the average model, only integrates errors due to negative I_L currents, as observed in the inductor current reference $I_{L_{ref}}$, presented in the subplot in Figure 3.20. The the dc-to-dc converter variables, i.e., V_{dc}, V_{in} and I_L are presented in Figures 3.17, 3.18, and 3.19, respectively. Note that the average model follows the same trend as the detailed model. When the BESS active power increases at $t = 2$s and $t = 9$s, more current is drawn from the battery pack, which results in a larger voltage drop in the internal battery resistor R_{bat}, and, thus, a lower voltage V_{in} (Figure 3.19), and a larger current flowing through the inductor, as depicted in Figure 3.19. When the BESS

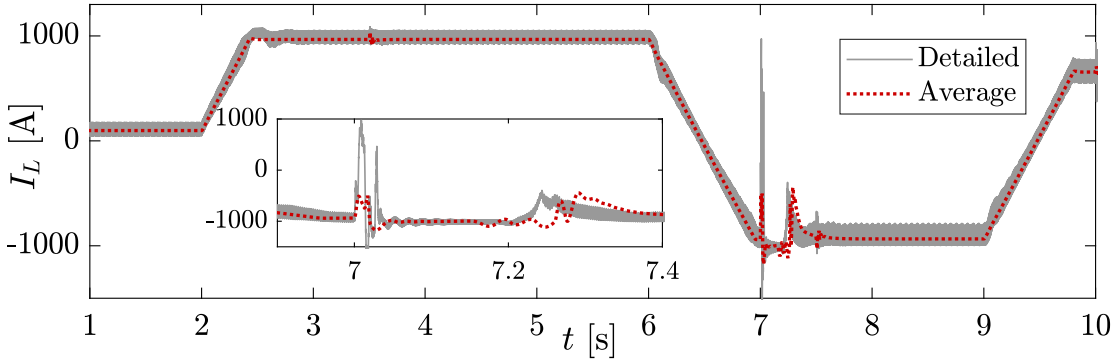

Figure 3.19: Dc-to-dc converter's inductor current.

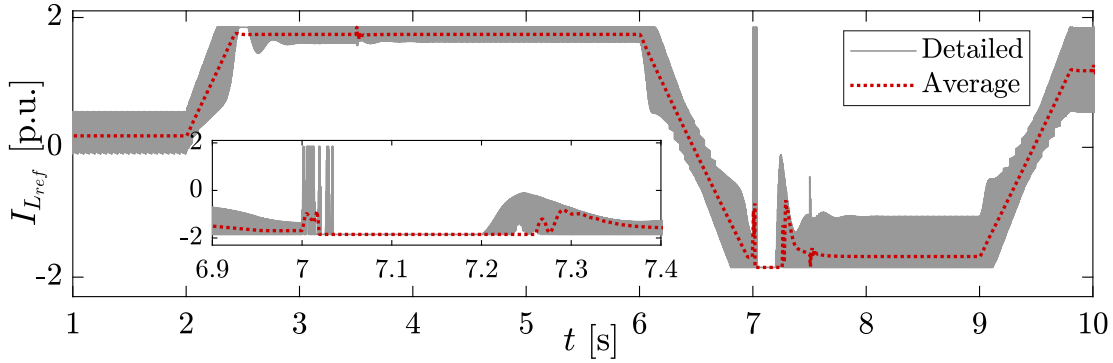

Figure 3.20: Dc-to-dc converter's inductor reference current $I_{L_{ref}}$.

changes its operation to charging mode, at $t = 6$s, the opposite occurs with V_{in}, which now increases, whereas I_L becomes negative. On the other hand, the dc link voltage is maintained constant by the dc-to-dc controller, as illustrated in Figure 3.17. Small transients are observed in the detailed model only, at the times when either P or Q change or reach a new value, i.e., at $t = 2$s, $t = 4$s, $t = 6$s, $t = 9$s, and $t = 10$s.

Finally, the VSC's modulation indices are presented in Figures 3.21 and 3.22. The signal m_d which controls P, follows the active power curve, while m_q follows Q. Observe that, when P changes, the controller slightly adjusts m_q to keep Q constant, because of the fact that the dq axes are weakly coupled in the filter connecting the VSC and the grid, as indicated in (3.9) and (3.10). Also, during the short circuit, both m_d and m_q reach their limits, due to the sudden dc link voltage change.

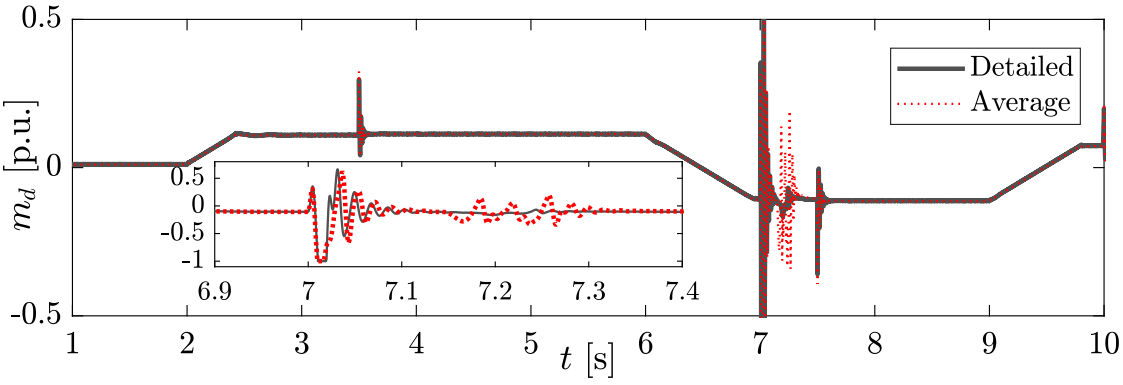

Figure 3.21: VSC's d-axis modulation index.

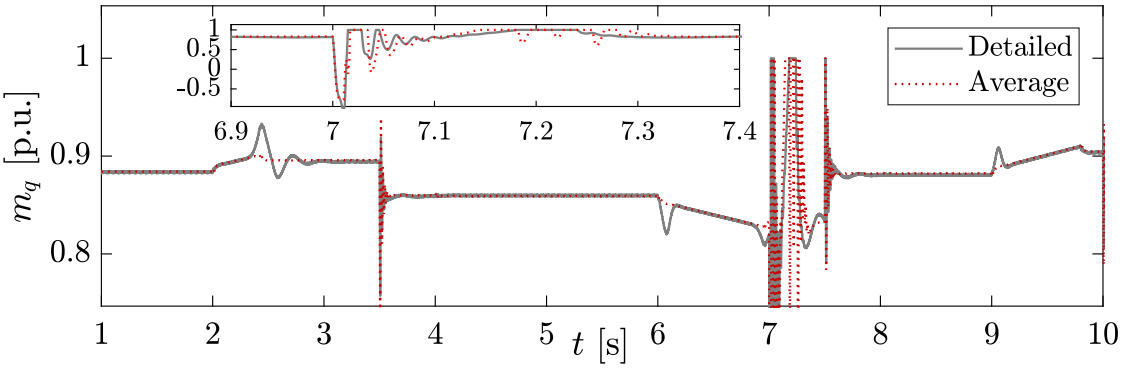

Figure 3.22: VSC's q-axis modulation index..

3.4.3 Impact of Distributed BESS on Transmission Systems

In this section, the detailed and average BESS models are compared in a grid context. Hence, three 1.5 MW BESS are connected in parallel at each load bus in the WSCC 9-bus test system [61], as depicted in Figure 3.23. This test system is similar to the one used in [17] and [20] to validate the WSCC model, with parameter values extracted from [61, 64], and comprises three synchronous generators of which the one connected at Bus 1 is a hydro generator while the generators connected to Bus 2 and 3 are steam units; the governors for each unit are based on [9] and are capable of providing PFR. The IEEE type DC1A excitation system with PSS were used for the three generators [64]. A three-phase version of the WSCC 9-bus was modeled in Matlabl's Simulink® for the detailed simulations.

The objectives of this test case are to demonstrate the equivalence of the detailed and

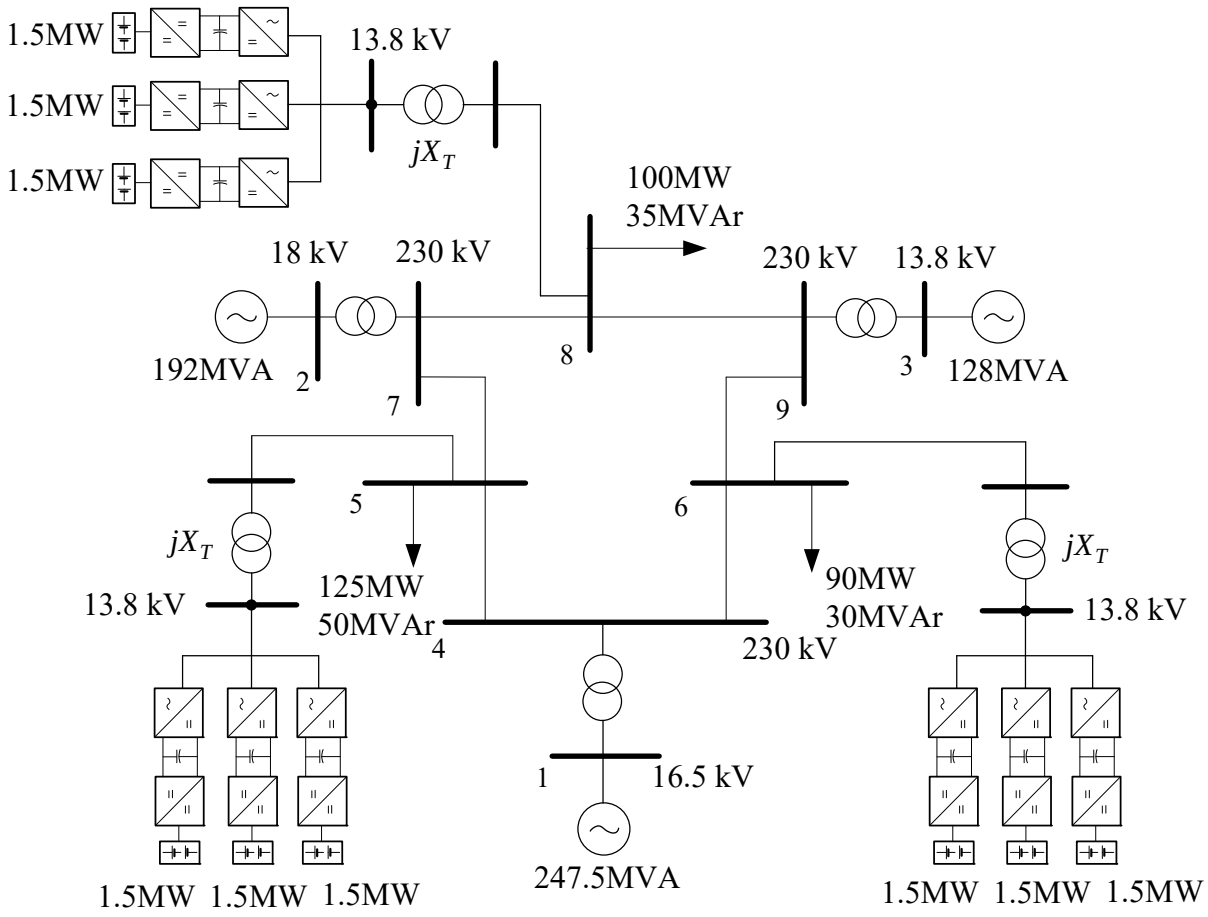

Figure 3.23: BESS connected to a modified WSCC 9-bus test system.

simplified models for practical dynamic grid studies, and study the potential of relatively small, utility scale BESSs connected at the distribution level to improve the operation of transmission systems. The active power controllers of the 9 BESSs connected at the load buses are set to provide PFR, while the reactive power controllers are set to provide constant Q. In this case, the BESSs are not coordinated by any centralized authority, but rather operate as distributed entities, thus measuring the frequency and voltage at local buses. Note that the total BESS power represents 2.4% of the system installed capacity and around 4 % of the total load. To test and compare the models, at $t = 3$ s, the set point of the governor of the generator at Bus 1 is reduced by 30 %, remaining in that condition thereafter. The same controller parameters are used in the detailed and average models.

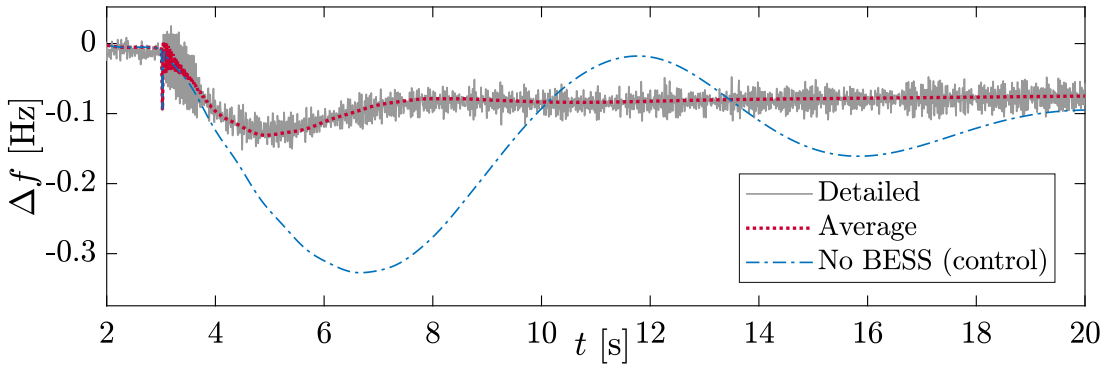

Figure 3.24: Frequency deviation at Bus 6.

Simulation Results

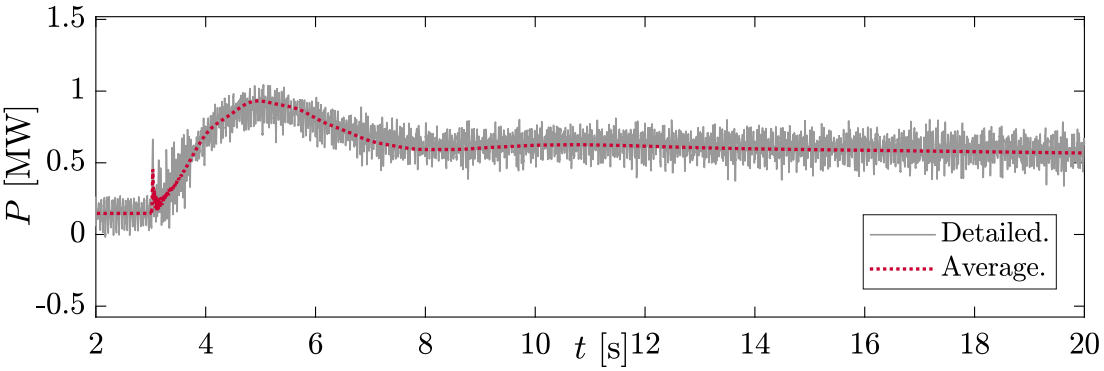

Figure 3.25: BESS active power injection at Bus 6.

The plot of the frequency deviation of one of the BESSs connected at Bus 6 is presented in Figure 3.24. For the purpose of comparison, a case in which the BESS operate in constant PQ mode is also plotted, referred in the figure as "No BESS control", thus leaving the frequency regulation task to the conventional generators. It is observed that, as soon as the contribution of generator 1 decreases at $t = 3s$, the frequency starts to drop. It takes around 20 s for the conventional generators to stabilize the frequency when the BESSs do not contribute to regulate frequency, which also results in a large initial frequency excursion of -0.32 Hz. On the other hand, when the BESSs help, the frequency regulation is significantly improved. In this case, as soon as the frequency starts to deviate, the frequency control commands the BESSs to rapidly increase their power injections, thus supplying the

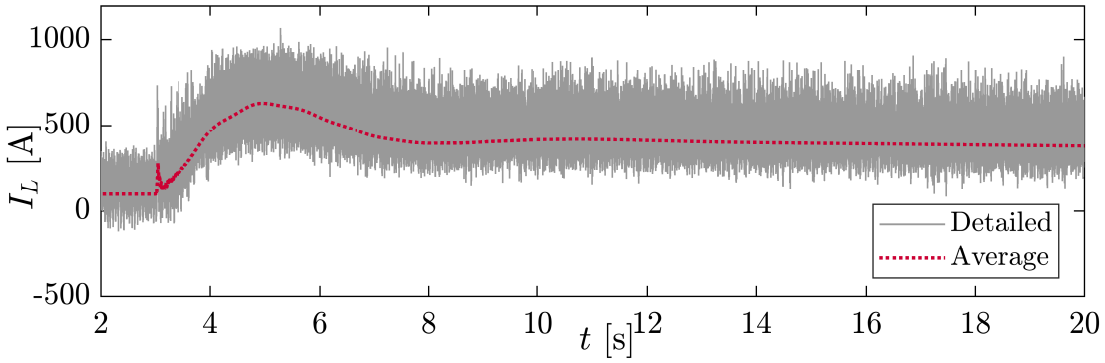

Figure 3.26: Inductor current in one dc-to-dc converter of the BESS at Bus 6.

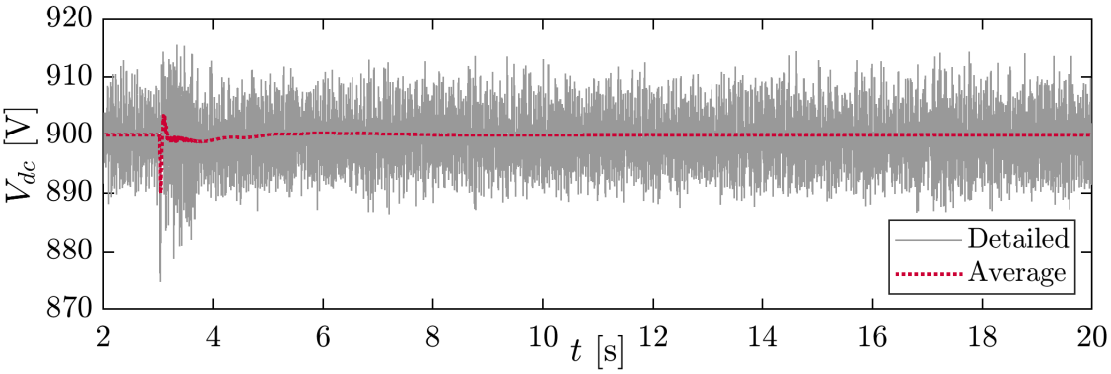

Figure 3.27: BESS dc-link voltage at Bus 6.

local loads, which reduces the system net load and the electrical torque experienced by the rotors of the conventional generators. As a result, the frequency stabilizes in less than 4 s, and presents a much smaller initial excursion, i.e., frequency drops down to -0.13 Hz. Notice that this was achieved with relatively small BESS capacity with fast active power being injected into the grid, as observed in Figure 3.25. This suggests that distributed BESSs with appropriate control capabilities and connected at the distribution level, have the potential to impact the transmission system operation.

Figures 3.26, 3.27, and 3.28 present the inductor current I_L, dc link voltage V_{dc}, and battery bank terminal voltage V_{in}, respectively, for the detailed and average models of the BESS connected at Bus 6. Note that all these variables show the same trend, the only difference being in the ripple content in the detailed model variables, thus proving their equivalence. It should be mentioned that the ripple of P and f at Bus 6 can be improved

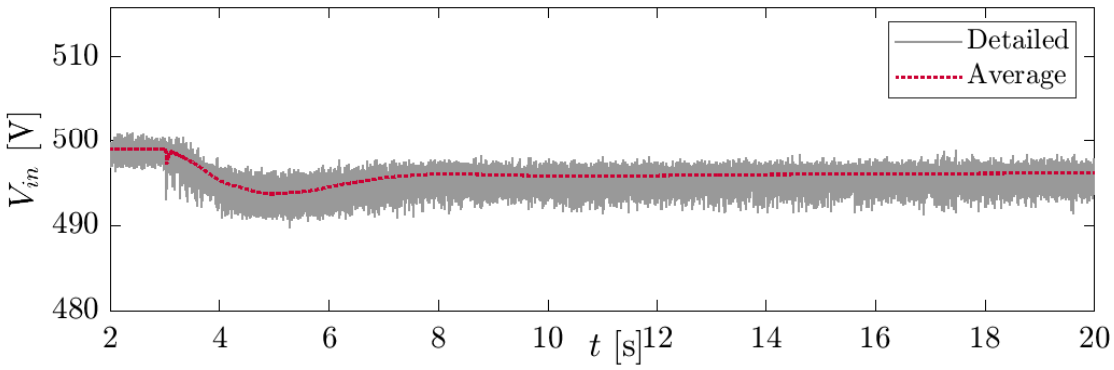

Figure 3.28: BESS battery bank output voltage at Bus 6.

by changing the ac filter design, which could also include a capacitor; since this thesis concentrates on average models, a simplified L-R filter has been used, whose parameters were obtained from an existing facility of similar size.

3.5 Impact of Bulk BESS on Transmission Systems

In this section, the proposed average BESS model, already validated against detailed simulations, is used to study the impact of utility-scale BESSs on the transmission system. These studies allow to explore the complete functionality of the proposed controls, allowing assessing the capability of the BESS to provide grid services such as frequency regulation, oscillation damping, and voltage regulation.

The simulations were performed using TSAT®. As discussed in Section 3.3.1, the proposed BESS model and controls were implemented as a UDM, which facilitates parametrization. A time step of .101ms was necessary for the simulations in TSAT® to ensure convergence of the dc-to-dc converter, which represents a trade-off between accuracy and simulation time. The model proposed is able to capture most of the relevant dynamics on the dc and ac side, which may bring instability to the BESS operation, which are not properly represented by models proposed in [17] and [20]. On the other hand, since average models are considered for the converters in the model proposed here, the simulation times are much faster than in detailed models, which require smaller time-steps to capture the high-frequency response of the converter's switches.

3.5.1 Test System

The proposed BESS model was added to the WSCC 9-bus test system [61], as depicted in Fig. 3.29. The transmission system parameters are the same as those described in Section 3.4.3. Due to the inertia constants and low damping coefficients, the test system has intrinsically low damping; hence, oscillations tend to occur when the system is disturbed. Therefore, the generator PSSs were properly tuned to guarantee at least 5% damping in all modes of oscillation.

A 45 MW BESS is used in the simulations, which is of a similar size as the BESS used in [13] for the same WSCC system, so that the BESS can help with the frequency regulation in this system. The model parameters are the same as in Table 3.3 in these studies, with the following changes: $dP_{\max} = 0.99$ p.u./s [31], S_b=45 MVA, and $N_c = 30$. The BESS is initially injecting 20 MW at Bus 10, which is connected to Bus 5 through a step-up transformer with a turn ratio of 13.8/230 and 0.0586 p.u. reactance. All the BESS's PI controllers were tuned by trial and error to obtain adequate dynamic responses.

3.5.2 Study Cases

The following four BESS different models were considered in the simulations for comparison purposes, which are summarized in Table 3.4:

- Complete Model: Corresponds to the proposed BESS discussed in Sections 3.1, 3.2, and 3.3. This model considers a battery bank, dc-to-dc converter, VSC, and the ac filter, and associated controls, and depicted in Fig. 3.1.
- Degraded Model: This is similar to the Complete Model, but the battery bank's resistance R_{bar} and voltage V_{bat} are increased and reduced, respectively, to model the degradation due to aging of the battery cells. Hence, based on [14], $V_{bat} = 400$ V and $R_{bat} = 0.025$ Ω, are used to model degradation, which represent a 33 % reduction with respect to their base values.
- Simplified Model: This model is similar to the Complete Model but the battery bank, the dc-to-dc converter, and its controls are removed, leaving a fixed dc voltage source feeding the dc side of the VSC at its nominal value.
- WECC Model: This corresponds to the model proposed in [17] and updated in [15, 20].

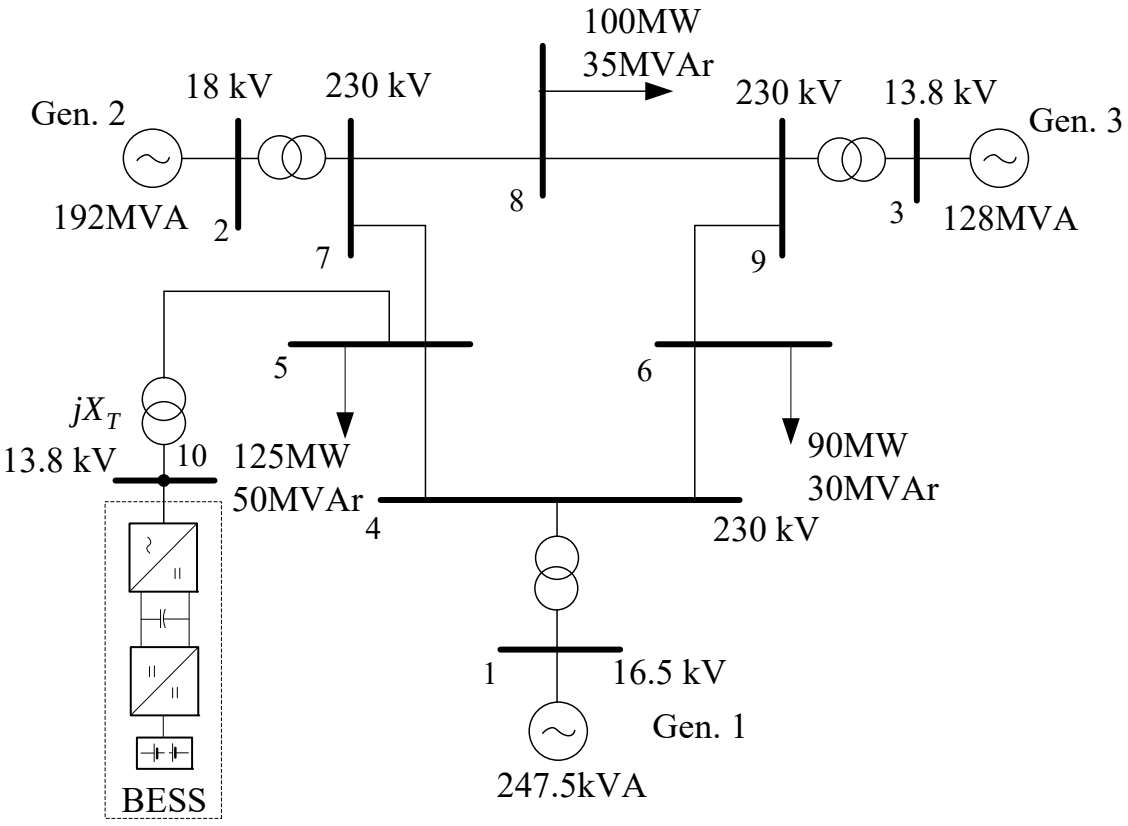

Figure 3.29: BESS connected to Bus 5 of a modified WSCC 9 bus test system.

Table 3.4: BESS Models

Name	Description	Model
Complete	Proposed complete average model	Battery + dc-dc + VSC + filter
Degraded	Same as Complete but $R_{bat} = 0.025\Omega$ & $V_{bat} = 400V$	Degraded battery + dc-dc + VSC + filter
Simplified	Proposed simplified model	Constant V_{dc} + VSC + filter
WECC	Model proposed in [17], [20]	VSC + filter

The following cases were simulated to study the BESS controls and impact on the transmission system and compare the aforementioned models:

- Case 1: At $t = 2$s, the reactive load at Bus 5 is increased from 50 MVAr to 80 MVAr, with the BESS providing Voltage Regulation (VR) and PQ mode.
- Case 2: At $t = 5$s, the generator connected at Bus 3 reduces its set point by 20 MW. The proposed complete and simplified BESS models are set to provide PFR ($K_D = 500$) and SFR, while the WECC model provides PFR only, as it does not have SFR capabilities. Furthermore, the complete model is also simulated to provide the two PFR and SFR services when the battery cells are degraded.
- Case 3: At $t = 1$s, a three-phase fault occurs at Bus 8 that is cleared after 50 ms. The PSSs are disabled in all generators, and the BESS is set to provide oscillation damping only, considering as well battery cell degradation. Since the WECC model does not have this feature, it is set to operate in constant PQ mode.
- Case 4: At $t = 1$s, a three-phase fault occurs at Bus 6 that is cleared after 50 ms. The PSSs are disabled and the BESS provides oscillation damping and voltage regulation at the same time, including also battery cell degradation. Since the WECC model does not have oscillation damping capabilities, it provides voltage regulation only.
- Case 5: At $t = 1$s, the load at Bus 8 increases by 20%, to represent a sudden loss of generation. The PSSs are disabled, and the BESS is set to provide PFR, oscillation damping, and VR simultaneously. Since the WECC model does not have oscillation damping capability, it is set to provide PFR only. The effects of degradation and SoC control are also studied in this case, with the SoC control parameters set to: $SoC_{\max}$ =2,222.22 kWh or 1 p.u., $SoC_{\min}$=0 kWh or 0.2 p.u., and SoC_o=111.11 kWh

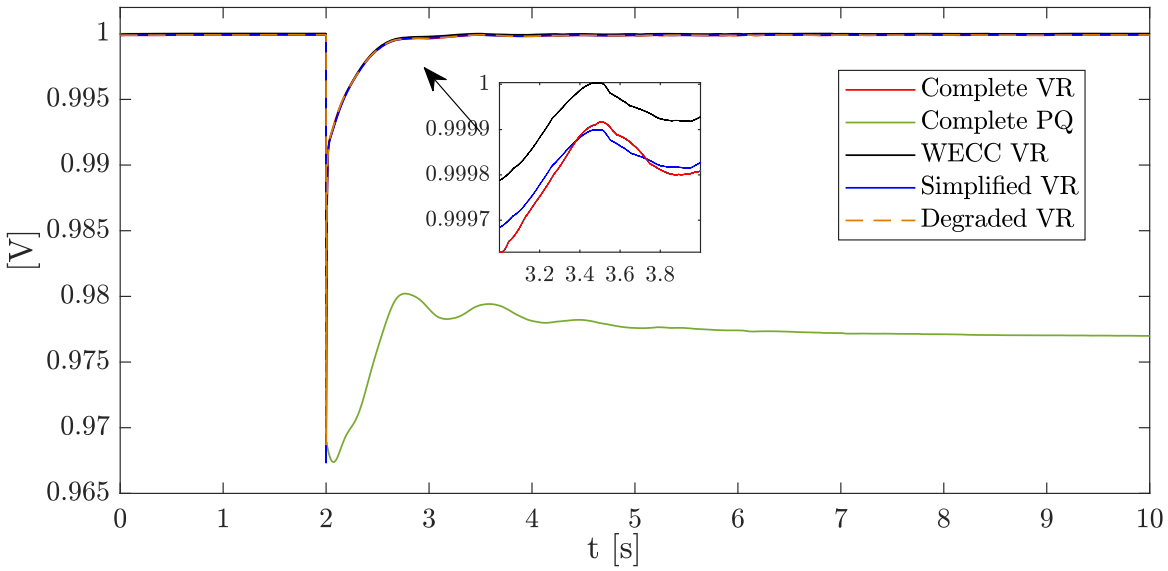

Figure 3.30: Case 1 voltage at Bus 5 for BESS in VR and PQ modes.

or 0.05 p.u. Notice that the energy capacity of the BESS is chosen to be small, which is to be expected for BESSs mainly providing PFR, SFR, and VR services, rather than arbitrage, and thus charges and discharges in relatively short times (seconds to minutes).

3.5.3 Results and Discussions

Case 1

Figure 3.30 shows the voltage at Bus 5, where it can be observed that after the event, the BESS regulates the voltage by increasing its reactive power injection, which helps the voltage to quickly reach steady-state, in less than a second. With the BESS operating in constant PQ mode, after the voltage drops to 0.97 p.u., which is generally acceptable, it does not fully recover to the nominal value, as expected, and stabilizing at around 0.975 p.u.

Observe that all the models yield similar responses, even when the battery cells are degraded, this can be attributed to the fact that while degradation limits the active power drawn from the BESS, the reactive power is mostly dictated by control of the VSC switches and the capacitor in the dc link.

Case 2

The effect of battery degradation on frequency regulation is examined in this case, and the results are presented in Figure 3.31 and Figure 3.32. Observe that the Complete and Simplified Models are very similar for PFR, stabilizing the frequency at 59.95 Hz, with SFR bringing the frequency back to nominal in around 1 sec, which requires larger active power injections from the BESS. The small oscillations observed in the SFR case, between 5s and 10s, are due to the values used in the SFR controller gains. Notice that when the WECC model is used, a larger frequency deviation occurs, with the frequency dropping to 59.83 Hz, thus taking longer to stabilize (around 6 s), due to an additional PI controller in the frequency regulation path in the WECC model and the absence of SFR in the WECC model; however, it reaches steady-state at the same value (frequency and power) as the Complete and Simplified Models.

When degradation is simulated, the BESS output power is limited to around 32 MW, thus compromising its frequency regulation capability. The reason for this limit is that, in discharging mode, degradation implies a lower V_{in} due to a reduced V_{bat} and larger voltage drop across R_{bat}; consequently, the dc-to-dc control requires a larger inductor current I_L to realize the nominal V_{dc}, but the inductor current limiter in the dc-to-dc controller prevents I_L from increasing further, which ultimately limits the discharging current from the battery cells and the BESS ability to respond to the commands of the plant controller, thus compromising the frequency regulation as shown in Figure 3.32, where the frequency drops to 59.86 Hz and stabilizes at 59.93 Hz, in the presence of both PFR and SFR. This behaviour can only be captured when modeling the dc-to-dc converter, which the WECC model does not consider.

Case 3

In this case all the PSSs are disabled, and hence the generators tend to oscillate after a disturbance, and thus the BESS can be used to provide the necessary damping. In order for the BESS to provide oscillation damping, the POD control needs to be properly tuned, as its parameters depend on the system conditions and other BESS parameters as explained next.

During the transients after the fault, all three generators and bus frequencies oscillate with a common under-damped frequency of $f_{osc} = 1.335$ Hz without PSS, which was determined by performing Prony analysis on the frequency traces [65], with the BESS not operating and all PSSs inactive. Although the rotor speed of the three generators oscillate at the same frequency, they have different mode phases, i.e., $\theta_{\omega_{g1}} = -36.38^o$,

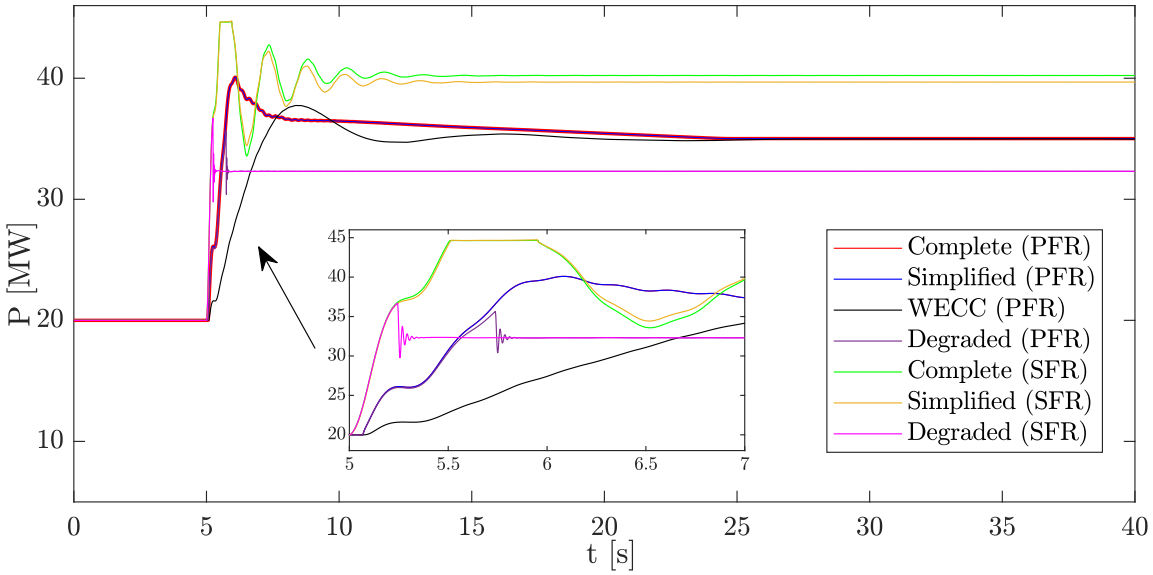

Figure 3.31: Case 2 active power supplied by BESS in PFR and SFR modes.

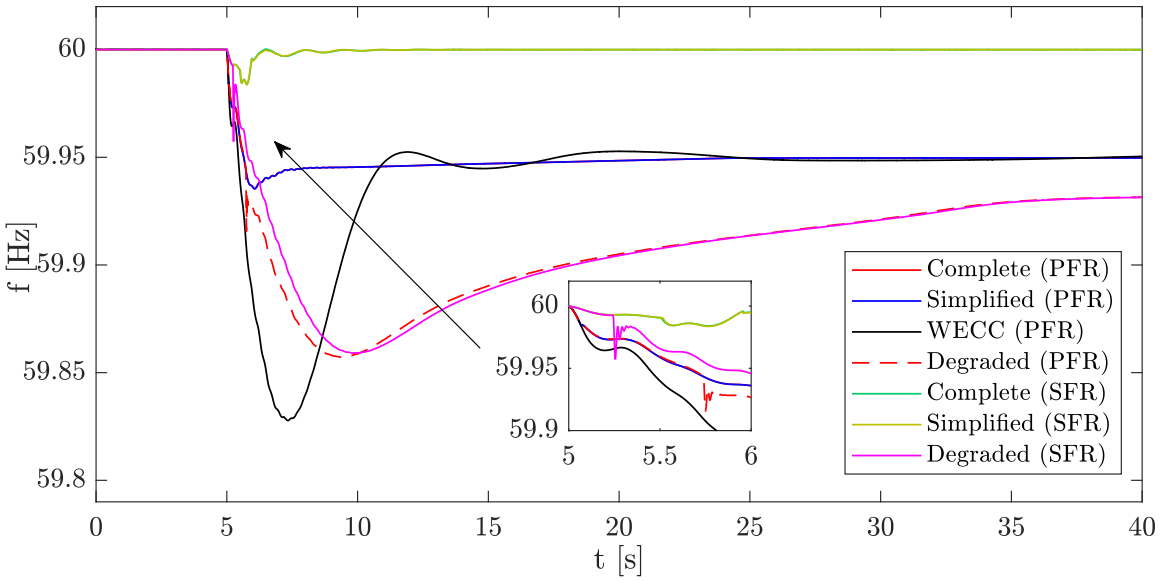

Figure 3.32: Case 2 frequency at Bus 10.

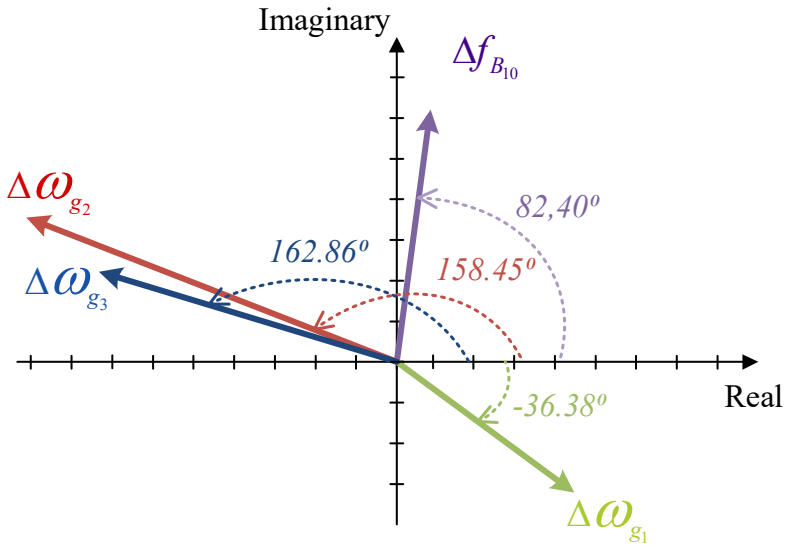

Figure 3.33: Eigen-vector components of generators' and Bus10 frequencies for low-damped frequency oscillation mode.

$\theta_{\omega_{g2}} = 158.45^o$, and $\theta_{\omega_{g1}} = 168.86^o$, as illustrated in Figure 3.33. Moreover, the mode phase of frequency signal at bus 10, at which the BESS is connected and from where the $\Delta\hat{f}$ signal will be obtained for the POD control, is $\theta_{\Delta f_{B10}} = 82.40^o$. Thus, the BESS can be tuned to add damping torque to Gen. 2, which is the one with the largest magnitude of frequency deviation $|\Delta\omega_{g2}|$ in that particular mode of oscillation. Hence, since the BESS output power should be 180^o phase-shifted with respect to the phase of $\Delta\omega g2$, the POD control parameters can be adjusted so that [58]:

$$\theta_{\Delta P_{BESS}} = \theta_{\Delta\omega_{g2}} + 180^o \tag{3.29}$$

where $\theta_{\Delta P_{BESS}}$ is the phase angle of the BESS power injected due to the POD action. Expressing $\theta_{\Delta\omega_{g2}}$ as a function of $\theta_{\Delta f_{B10}}$, which is the input frequency of the POD, it follows that:

$$\theta_{\Delta P_{BESS}} = \theta_{\Delta f_{B10}} + (158.45^o - 82.40^o) + 180^o \tag{3.30}$$

$$\theta_{\Delta P_{BESS}} = \theta_{\Delta f_{B10}} + 256.05^o \tag{3.31}$$

$$\theta_{\Delta P_{BESS}} - \theta_{\Delta f_{B10}} = 256.05^o \tag{3.32}$$

$$\tag{3.33}$$

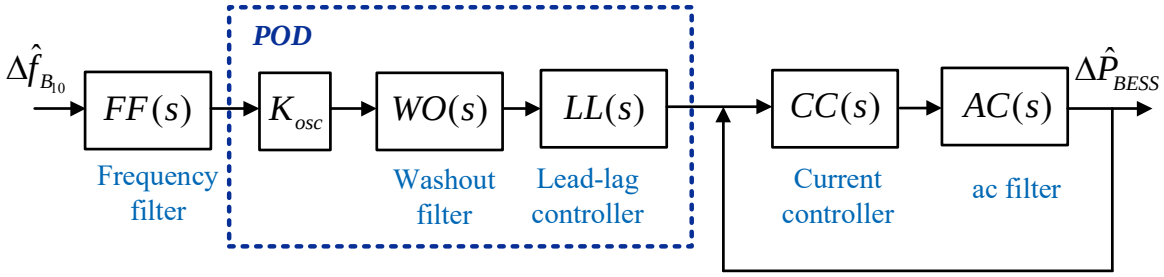

Figure 3.34: Series of transfer functions between $\Delta f_{B_{10}}$ and $\Delta\hat{P}_{BESS}$ in the BESS.

From the proposed plant controller depicted in Figure 3.6 and current controller in Figure 3.8, a transfer function having $\Delta\hat{f}_{B10}$ as input and $\Delta\hat{P}_{BESS}$ as output, respectively, can be derived, as the multiplication of individual transfer functions representing the different components in the path between the POD input and BESS output, as presented in Figure 3.34, where $FF(s)$, $WO(s)$, $LL(s)$, $CC(s)$, and $AC(s)$ are the individual transfer functions of the frequency transducer (filter), washout filter, lead/lag controller, current controller, and ac filter, respectively.

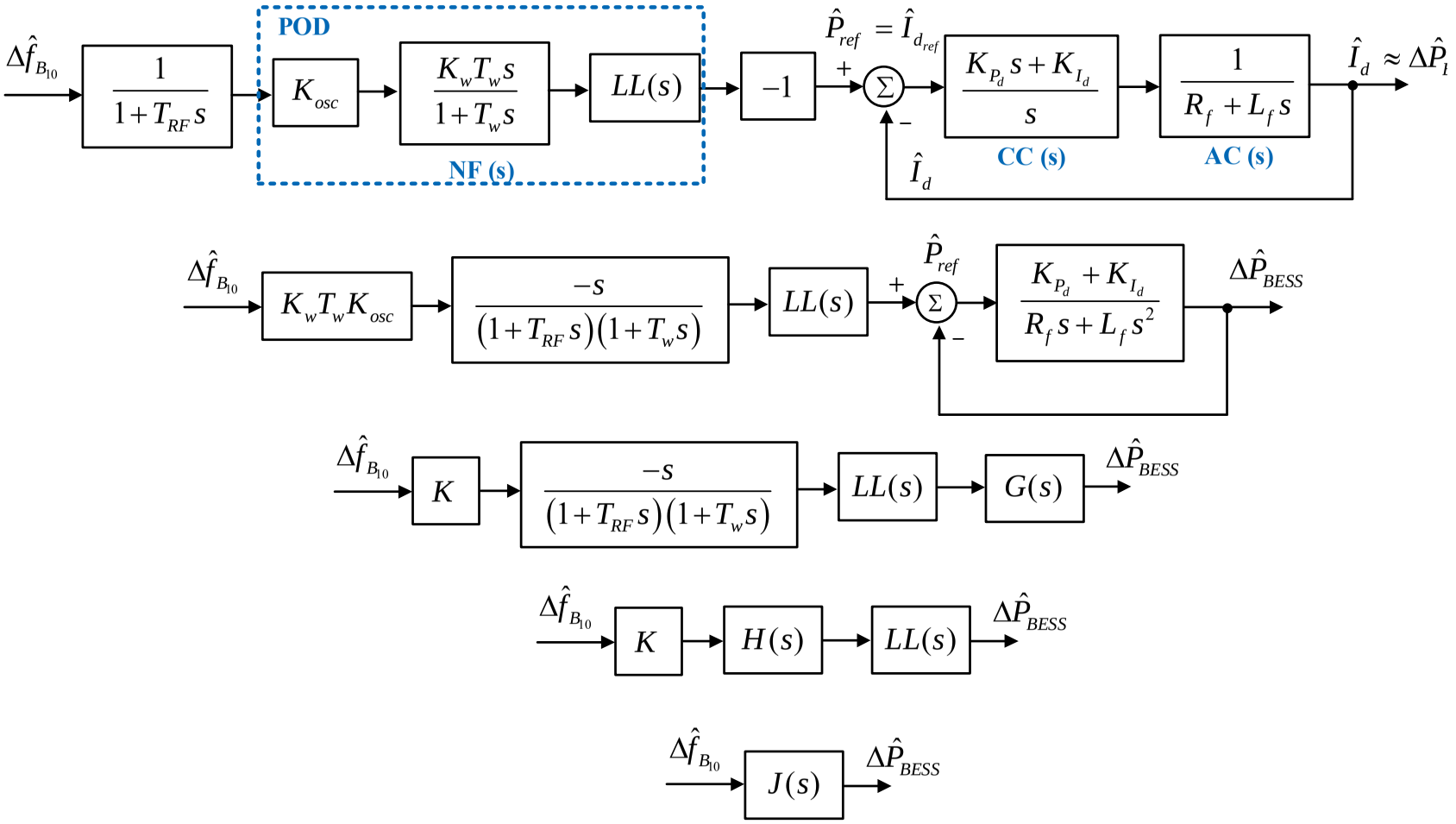

Figure 3.35: POD transfer functions operations.

By substituting the actual individual transfer functions in Figure 3.34, and assuming that $\hat{V}_d \approx 1$ p.u, and $\hat{V}_q \approx 0$ p.u, (this yields $\widehat{P}_{ref} = \widehat{V}_d \widehat{I}_{d_{ref}} \approx \widehat{I}_{d_{ref}}$) and assuming a simplified representation of the current controller plus ac filter [32], the transfer functions in Figure 3.35 can be obtained, where $K = K_W T_W K_{osc}$, and $G(s)$ is the open loop transfer function of the current controller and ac filter:

$$G(s) = \frac{\dfrac{K_{P_d} s + K_{I_d}}{R_f s + L_f s^2}}{1 + \dfrac{K_{P_d} s + K_{I_d}}{R_f s + L_f s^2}} \tag{3.34}$$

$$= \frac{K_{P_d} s + K_{I_d}}{K_{I_d} + (R_f + K_{P_d})\, s + L_f s^2} \tag{3.35}$$

and $H(s)$ is:

$$H(s) = \frac{-s}{(1 + T_{RF} s)\,(1 + T_W s)} G(s) \tag{3.36}$$

$$= \frac{-K_{P_d} s^2 - K_{I_d} s}{(1 + T_{RF} s)\,(1 + T_W s)\,(K_{I_d} + (R_f + K_{P_d})\, s + L_f s^2)} \tag{3.37}$$

Thus,

$$\frac{\Delta \hat{P}_{BESS}}{\Delta \hat{f}_{B10}} = K H(s) LL(s) = K |H(s)||LL(s)| \underline{/\theta_{H(s)} + \theta_{LL(s)}} \tag{3.38}$$

$$\frac{\Delta \hat{P}_{BESS}}{\Delta \hat{f}_{B10}} = |J(s)| \underline{/\theta_{J(s)}} = \left| \frac{\Delta \hat{P}_{BESS}}{\Delta \hat{f}_{B10}} \right| \underline{/\theta_{\Delta P_{BESS}} - \theta_{\Delta f_{B10}}} \tag{3.39}$$

From (3.38) and (3.39), it follows that:

$$\theta_{\Delta P_{BESS}} - \theta_{\Delta f_{B10}} = \theta_{H(s)} + \theta_{LL(s)} \tag{3.40}$$

Substituting (3.32) in (3.40), for the particular condition of $s = j2\pi f_{osc}$:

$$\theta_{H(s=j2\pi f_{osc})} + \theta_{LL(s=j2\pi f_{osc})} = 256.05^o \tag{3.41}$$

where $\theta_{H(s=j2\pi f_{osc})}$ can be calculated by substituting $s = j2\pi 1.335$ in (3.37) and the corresponding parameters from Table 3.3, with R_f and L_f expressed in p.u., as follows:

$$H(j2\pi 1.335) = 7.884\underline{/245.7^o} \tag{3.42}$$

From (3.42) and (3.41), the phase required by the lead/lag compensator, at the oscillation frequency f_{osc}, can be calculated as follows:

$$\theta_{LL} = 256.05 - 245^o \tag{3.43}$$

$$= 10.29^o \tag{3.44}$$

This is the input provided to the Matlab's® Control System Designer toolbox [66] to obtain, the values of T_{L_1}, T_{L_2}, T_{LG_1}, and T_{LG_2} presented earlier in Table 3.3. Hence, replacing these parameters into the lead/lag transfer function $LL(s)$, for $s = j2\pi 1.335$, the gain and phase added by the lead/lag compensator can be found to be as expected:

$$LL(s) = \frac{1 + T_{L_1}s}{1 + T_{L_2}s}\frac{1 + T_{LG_1}s}{1 + T_{LG_2}s} \tag{3.45}$$

$$LL(s = j2\pi 1.335) = 1.1337\underline{/10.29^o} \tag{3.46}$$

The washout parameters were obtained from typical values used in PSSs [64], while the main controller gain K_{osc} was calibrated by trial-and-error, running time-domain simulations until the best BESS performance for damping the oscillations was achieved. After the short circuit, the oscillation damping control used in the Complete and Simplified models stabilizes the system oscillations in less than 4s, as illustrated in Figure 3.37 and Figure 3.36, thus proving the effectiveness of the proposed control. On the contrary, undamped oscillations are observed with the WECC model, as this does not have POD control. Similarly, when degradation is simulated (two levels in this case), the effectiveness of the control is compromised. Thus, the frequency further deviates after the short circuit, i.e., down to 59.93 Hz for an $R_{bat} = 0.025\,\Omega$, and 59.87 Hz for $R_{bat} = 0.1\,\Omega$, and the system takes longer time to stabilize (around 11 s), with low frequency oscillations taking longer to damp down (around 8 s). The reason for this is that, as in Case 2, the dc-to-dc controller limits the BESS active power in discharging mode, which is observed as high-frequency oscillations in the degraded curves; however, in charging mode (negative P in Figure 3.37), the voltage drop in R_{bat} results in a larger input voltage to the dc-to-dc converter at the battery bank side V_{in}, because the current flows from the dc-to-dc converter to battery

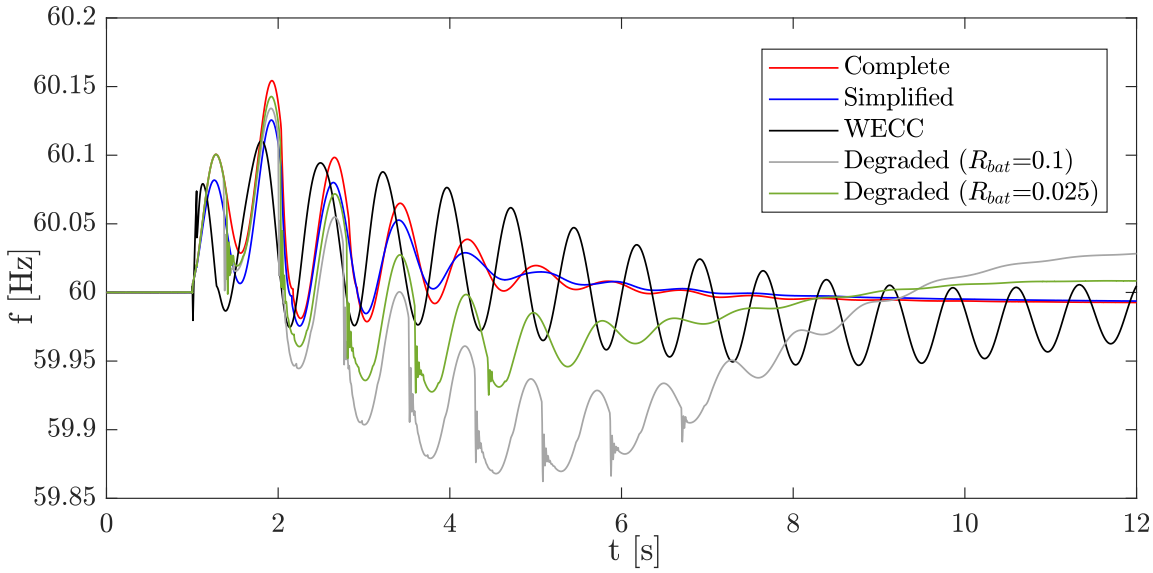

Figure 3.36: Case 3 frequency at Bus 10 for BESS providing POD.

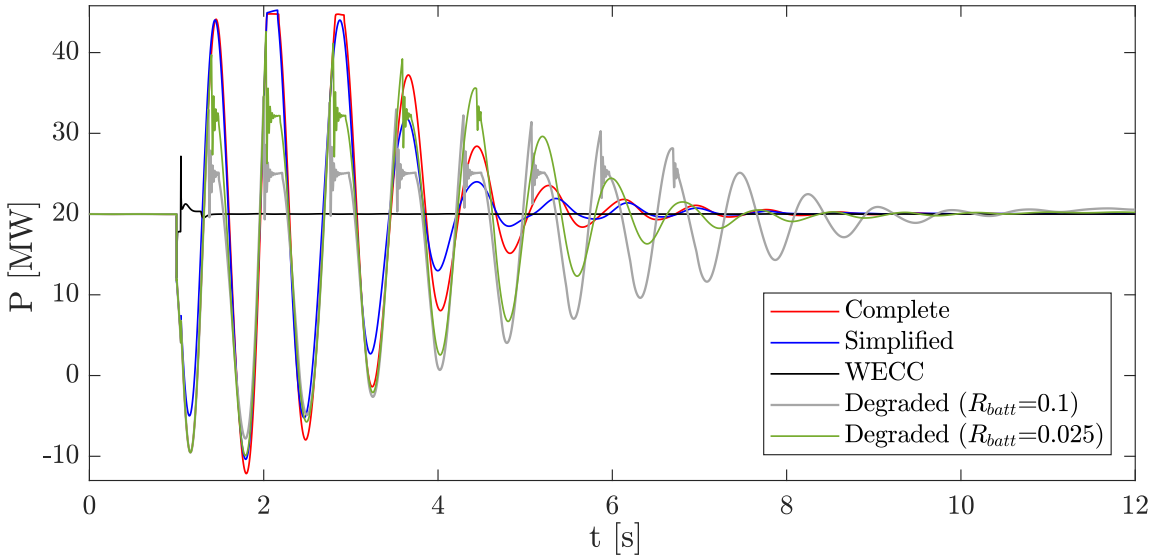

Figure 3.37: Case 3 active power supplied by BESS.

cells, which can be readily managed by the dc-to-dc controller by reducing the duty ratio, and thus no limit-related issues are observed when the BESS operates in charging mode.

Consequently, even in the battery-degraded cases, the POD controller still manages to damp the low-frequency oscillations, albeit taking longer to do so.

Observe in Figure 3.37 that the value of K_{osc} used allows operating the BESS at its full capacity during the first seconds after the fault, barely reaching limits, which contributes to damp the oscillations faster. Furthermore, the Complete model shows larger active power oscillations than the Simplified model, which results in larger frequency oscillations also. These differences can be attributed to the action of the dc-to-dc converter controller, which affects the dc link voltage as the power drawn from the battery cells varies.

Case 4

In Figures 3.38 to 3.41, the simultaneous operation of the BESS for oscillation damping and voltage control is demonstrated. Observe that, after the fault, the system oscillations are rapidly damped by the BESS in all cases, except when the WECC model is used, which shows undamped oscillations due to the lack of POD control. Indeed, the Complete and Simplified models damp the oscillations faster than in Case 3, in around 3s; this is due to the fact that the load being short-circuited during the fault is slightly larger in Case 3, but also because the BESS regulates voltage in Case 4, which helps to maintain the system voltages during the fault, as observed in Figure 3.41 for the voltage at Bus 10, which recovers very fast. In the Degraded case, the oscillations tend to last longer, but are also finally damped. These simulations demonstrate the effectiveness of the controls to allow the BESS to provide two independent services simultaneously, without significant interference between them.

Case 5

The results of Case 5 are presented in Figures 3.42 to 3.45. In this case, after the disturbance, the proposed PFR control increases the BESS active power injection, which stabilizes the system frequency at 59.95 Hz in less than 2s, while the POD control simultaneously acts to damp the system low frequency oscillations. The WECC model, on the other hand, takes longer to stabilize the frequency at the same value (around 5s), and does not damp the low-frequency oscillations, as expected. When degradation is considered, it can be observed that, again, since the BESS is operating in discharging mode, its power is limited; hence, the effectiveness of the BESS to regulate the frequency is compromised. Therefore, the system frequency takes longer time to stabilize (around 8s), as more power from the slower traditional generators is needed for regulation. Also, as the BESS active

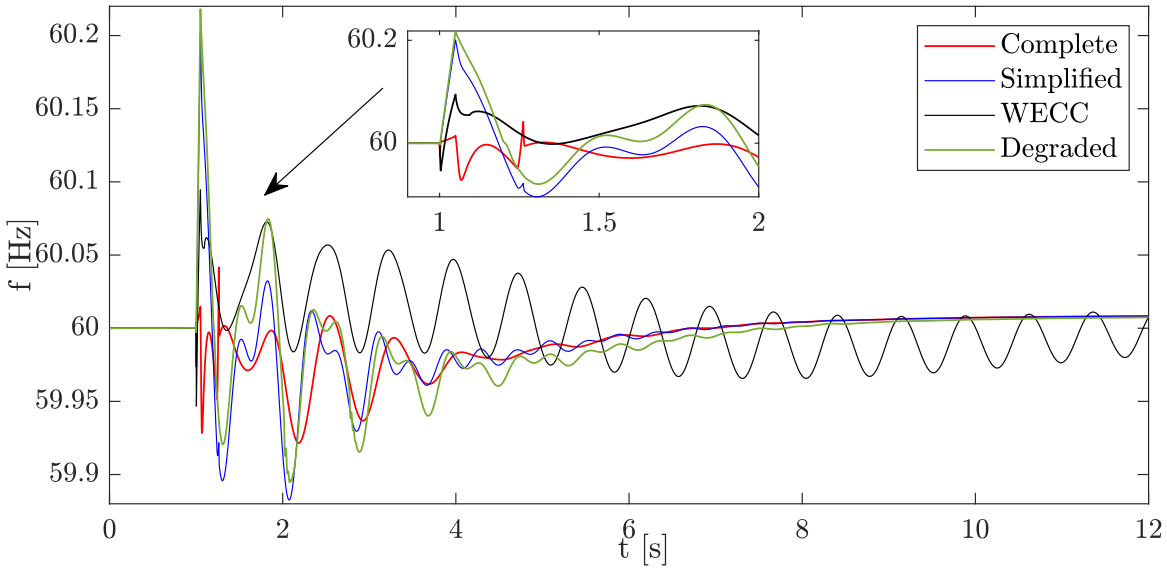

Figure 3.38: Case 4 frequency at Bus 10 with BESS providing POD and VR services.

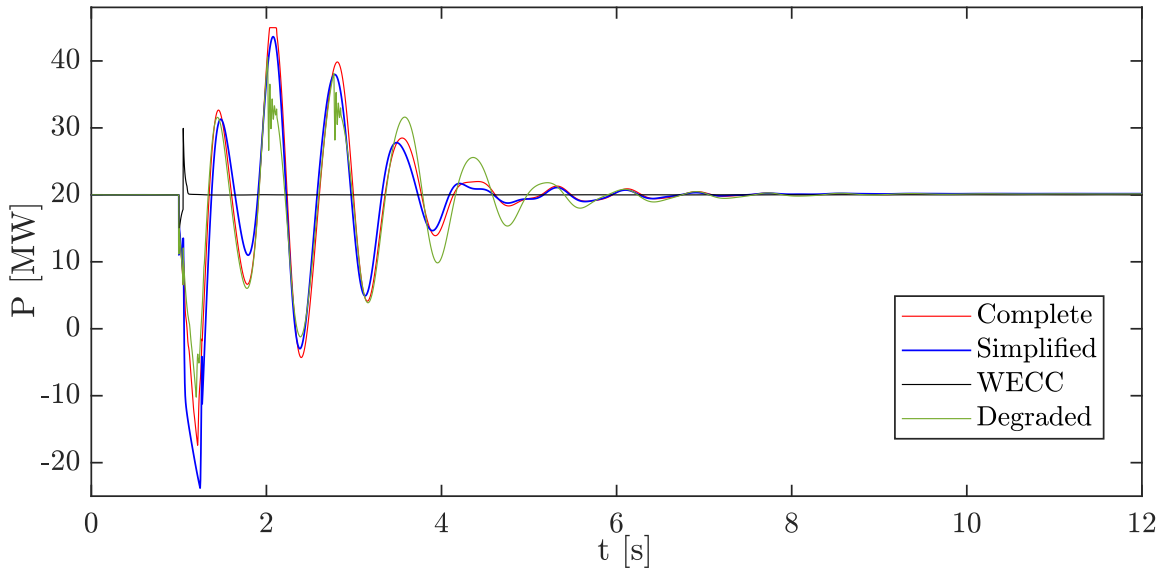

Figure 3.39: Case 4 active power supplied by BESS.

power is constrained, the POD is ineffective, and thus sustained oscillations are observed in active and reactive powers.

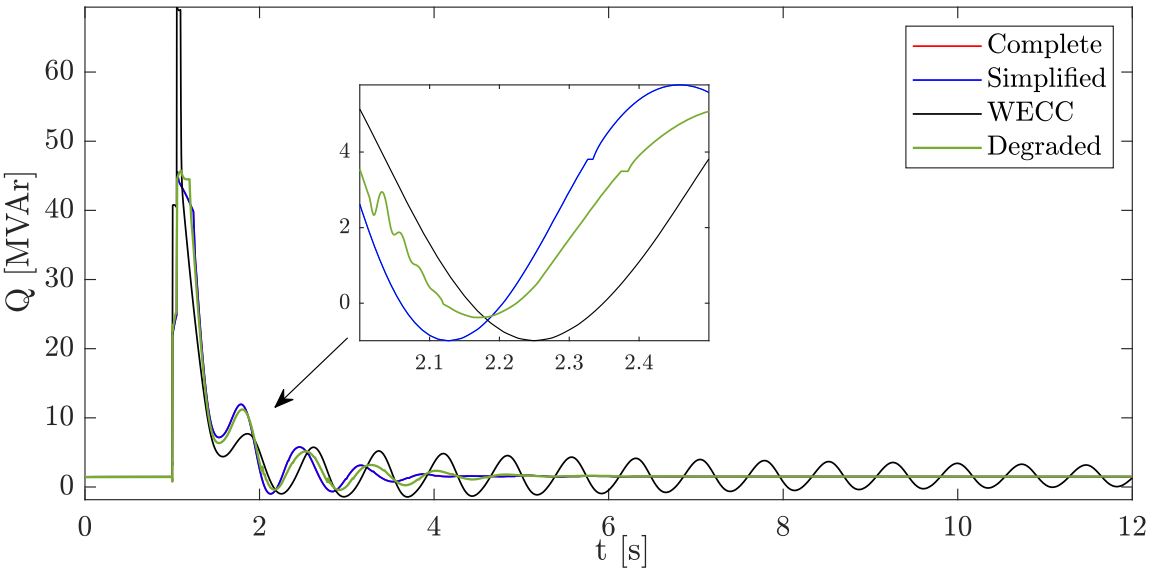

Figure 3.40: Case 4 reactive power supplied by BESS.

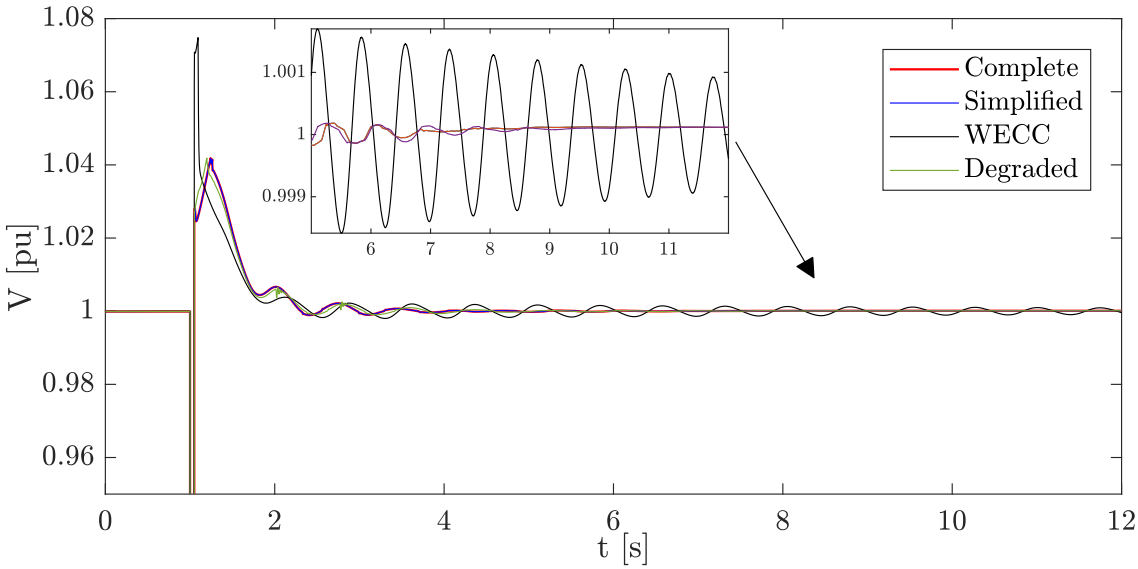

Figure 3.41: Case 4 voltage at Bus 10 for BESS.

Once the SoC reaches its minimum value at around 12s, as illustrated in Fig. 3.46 the SoC control, modeled in the three cases, shuts down the BESS, leaving the frequency

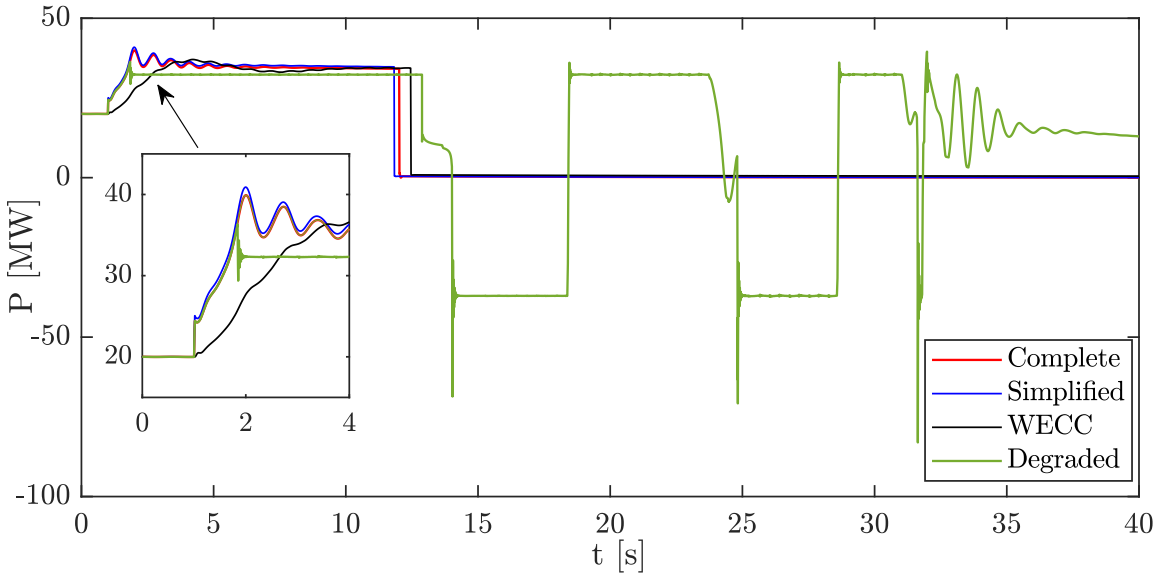

Figure 3.42: Case 5 active power supplied by BESS in PFR, POD, and VR modes.

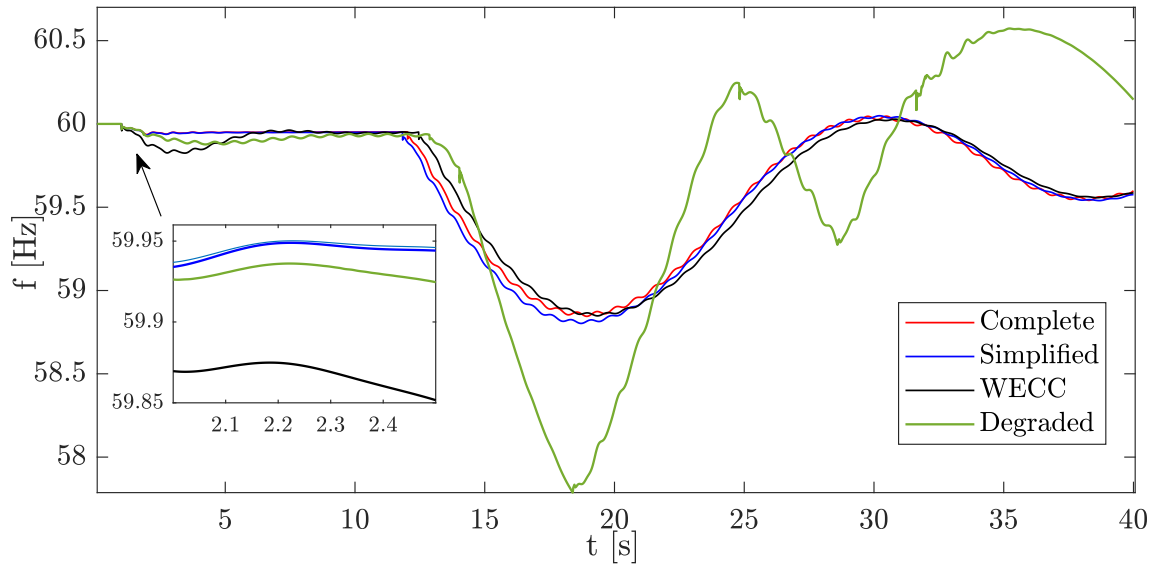

Figure 3.43: Case 5 frequency at Bus 10.

regulation task to the generators, which deteriorates the frequency regulation performance of the system, resulting in large low-frequency oscillations. When degradation is considered,

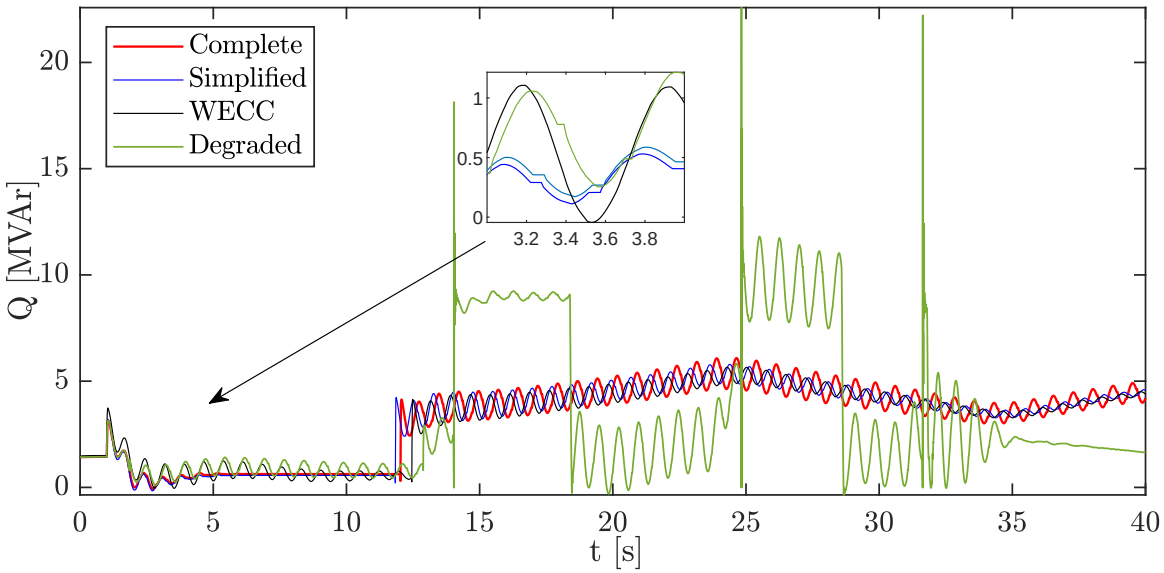

Figure 3.44: Case 5 reactive power supplied by BESS.

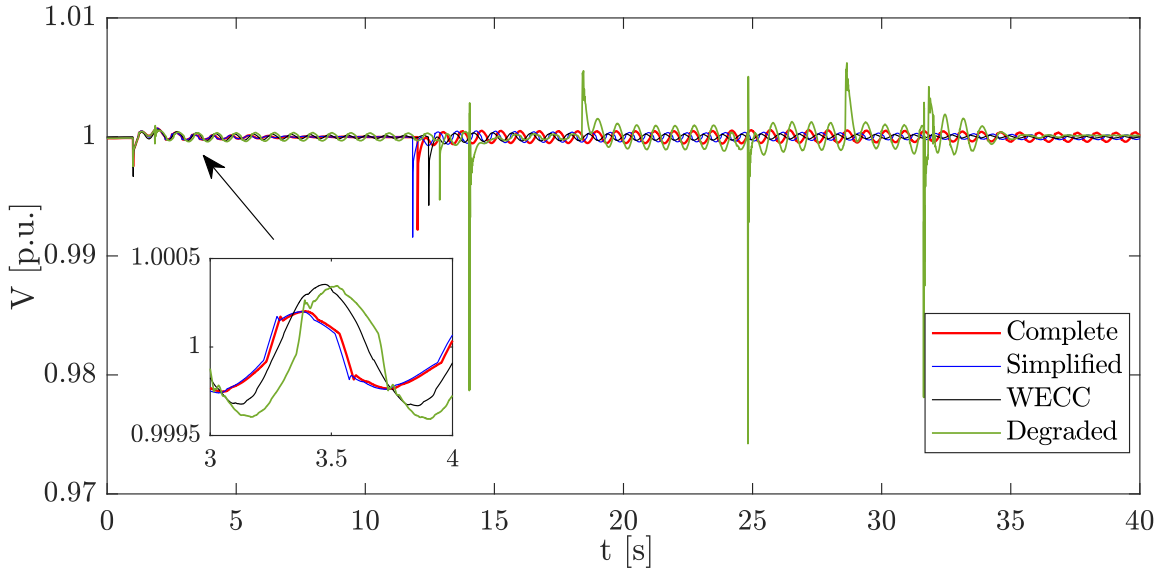

Figure 3.45: Case 5 voltage at Bus 10.

i.e., large R_{bat} and low V_{bat}, the BESS takes longer time to fully discharge, due to its limited output power; however, when it is finally shut down, a more severe oscillatory behavior

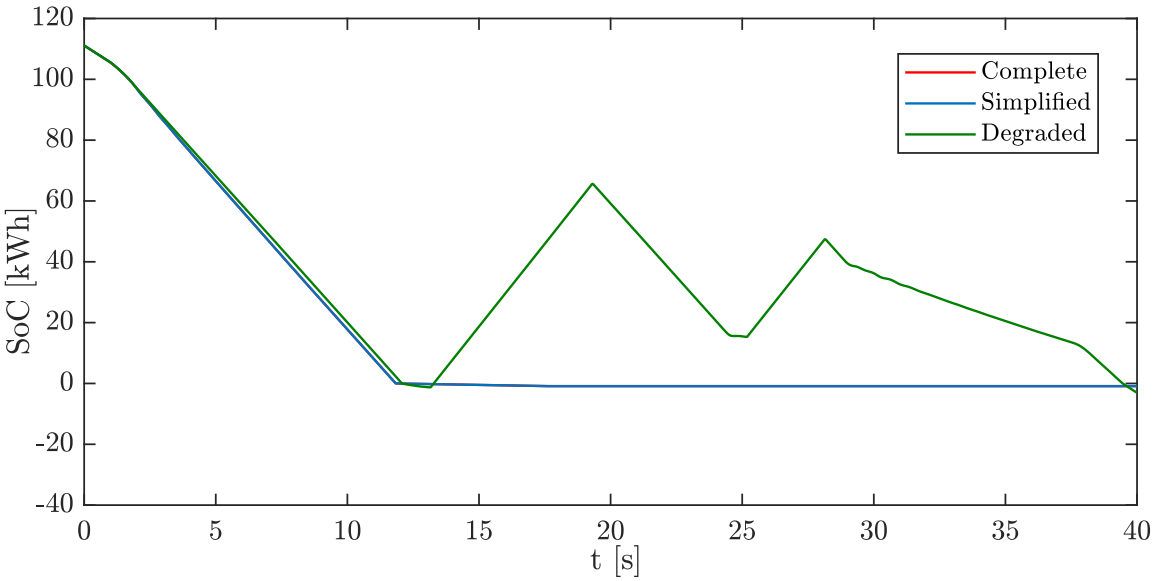

Figure 3.46: Case 5 BESS SoC.

is observed, which results in frequency instability. Notice that before the SoC limits are reached, the BESS is fully capable of regulating the frequency and damp the oscillations at the same time, while keeping the voltage regulated at its nominal value.

3.6 Summary

In this chapter, a dynamic average BESS model, including a simplified model for the battery bank, VSC, bi-directional buck-boost converter, ac filter, and associated controls, suitable for modeling small, medium or large BESS facilities, was proposed and validated against a detailed version of it, connected to an infinite bus and to a benchmark test power grid. It was demonstrated that, for step changes in the power references and contingencies such as short circuits, both models were equivalent as long as the limits in the control systems were not reached; otherwise, differences arose. It was also demonstrated that those differences could only be observed when the dc-to-dc converter and its controls were considered, which, in part, justify the need for their modelling. When the detailed and average models were simulated connected to a transmission gird, it was demonstrated that small capacity of distributed BESS was enough to considerably improve the system's frequency regulation with respect to a case without BESS.

The proposed average model was further compared with a simplified version that neglected the dynamics of the dc-to-dc converter, and with an existing BESS model widely used by industry, i.e., the WECC model, for several contingencies. It was demonstrated that the additional controls proposed in this thesis for the BESS, which were not considered in the WECC model, namely, SFR and POD controls, could significantly improve the contribution of a large BESS to the stability of the transmission grid, with controls that required less logic flags and regulation paths.

The inclusion of the dynamics of the dc-to-dc converter and its controls, and the decoupled dq current control in the BESS model are demonstrated here to be relevant, especially when degradation of the battery cells are considered. However, modeling this requires a much smaller integration step depending on the software used, which also increases simulation times.

Chapter 4

Aggregated BESS Dynamic Models for Active Distribution Network Studies

In this Chapter, a transmission-system-level aggregated model of BESSs distributed throughout the ADNs, is proposed, to study their dynamic performance and services provided to the grid. ADNs comprise intelligent loads, local generation, particularly solar PV, and BESSs, which can provide different services to transmission grids, including voltage control, oscillation damping, frequency regulation, and active and reactive power injections. Proper equivalent models of the ADN components allow to evaluate the impact and integration of these networks with transmission grids. The measurements of the aggregated response of the BESSs at the boundary bus of the ADN with the transmission system are used here to develop an aggregated black-box model based on two NNs, one for active power and another for reactive power, with their optimal topology obtained using a GA. Detailed simulations are performed, using TSAT and Simulink, of multiple BESSs connected to a CIGRE benchmark ADN connected to a load bus of the 9-bus WSCC benchmark transmission network; the test ADN is then replaced by the proposed black-box model, with aggregated models of the loads and PV generation, demonstrating that the proposed model can accurately reproduce the results obtained with the full ADN.

4.1 Aggregated BESS Black-box Model

In this section, a methodology to obtain an aggregated black-box BESS model at the boundary bus between transmission and distribution systems is proposed. The model is based on NNs representing active and reactive power injections, whose topologies are optimized using a GA, with parameters (weights) obtained by training the NNs based on data from measurements of active with reactive power, voltage, and frequency at the boundary bus. It is assumed that the BESSs are connected to a distribution system comprised also of loads and PV generation, and modeled as proposed in Chapter 3. PV generation is considered here as the dominant ADN supply source, instead of diesel generators or wind turbines, as these are becoming the norm in ADNs, as significant PV generation capacity is being deployed in various jurisdictions, with BESS addition being considered to enhance and facilitate PV integration [67, 68]. Nevertheless, aggregated models of other types of generation could be readily considered in the proposed black-box model development without loss of generality.

4.1.1 Proposed Black-box Model

NARX NNs are a subclass of recurrent NNs, which has been shown to be better for BESS modelling than conventional recurrent NNs in terms of learning capability, speed of convergence, and accuracy [69]. Hence, since many NNs are trained and tested as part of the algorithm to develop black-box models in this thesis, speed of convergence plays a major role, and thus NARX NNs are used here for the proposed black-box models, based on (2.1) and (2.2) for open- and closed-loop configurations, respectively, as depicted in Figure 4.1, where the TDL blocks represent time delays applied to their inputs. Note that the main difference between the open- and closed-loop configurations is that the latter does not need information of the actual system output, as the NN's output values $\check{y}_{t-1}, \check{y}_{t-2}, .., \check{y}_{t-n_y}$ are fed back to the network. Moreover, the NARX-NN's G function in (2.1) or (2.2), can be implemented as a feedforward NN with the corresponding input and output delays feeding the first hidden layer [70] as presented in Figure 4.2.

The proposed black-box model is presented in Figure 4.3, which consists of two NARX NN in closed-loop configuration, NN-P and NN-Q, whose outputs represent the active P and reactive Q power injections of the aggregated BESSs at the boundary bus, and are calculated as follows:

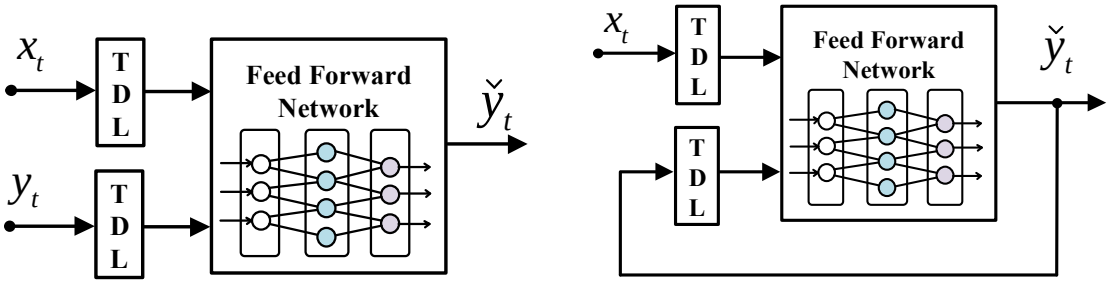

Figure 4.1: NARX NN in (a) open-loop and (b) closed-loop configurations.

$$\check{P}_t = F\begin{pmatrix} \check{P}_{t-1}, \check{P}_{t-2}..., \check{P}_{t-n_y}, \\ \check{f}_t, \hat{f}_{t-1}, ..., \hat{f}_{t-n_x}, \\ \hat{V}_t, \hat{V}_{t-1}, ..., \hat{V}_{t-n_x}, \\ \Delta\hat{P}_{ref_t}, \Delta\hat{P}_{ref_{t-1}}, ..., \Delta\hat{P}_{ref_{t-n_x}}, \\ \hat{PV}_t, \hat{PV}_{t-1}, ..., \hat{PV}_{t-n_x} \end{pmatrix} \tag{4.1}$$

$$\check{Q}_t = H\begin{pmatrix} \check{Q}_{t-1}, \check{Q}_{t-2}, ..., \check{Q}_{t-n_y}, \\ \hat{f}_t, \hat{f}_{t-1}, ..., \hat{f}_{t-n_x}, \\ \hat{V}_t, \hat{V}_{t-1}, ..., \hat{V}_{t-n_x}, \\ \Delta\hat{P}_{ref_t}, \Delta\hat{P}_{ref_{t-1}}, ..., \Delta\hat{P}_{ref_{t-n_x}}, \\ \hat{PV}_t, \hat{PV}_{t-1}, ..., \hat{PV}_{t-n_x} \end{pmatrix} \tag{4.2}$$

where $\check{P}$ and $\check{Q}$ are estimations of the active and reactive power injections of the aggregated BESSs in p.u., respectively, and assumed to be functions of the relevant measurements available at the boundary bus; $\hat{V}$ and $\hat{f}$ are the voltage and frequency at the boundary bus in p.u., respectively; $\Delta\hat{P}_{ref}$ is the command signal sent from the central entity to modify the power set point of BESSs in p.u. (see Section 3.2.1); $\hat{PV}$ is a signal proportional to the solar irradiance, expressed as the per unit power of all PV generators; $F : \mathbb{R}^{1\times(n_y+4(1+n_x))} \rightarrow \mathbb{R}$ and $H : \mathbb{R}^{1\times(n_y+4(1+n_x))} \rightarrow \mathbb{R}$ are nonlinear functions mapping the input data, including the feedback of historical data of the estimated outputs, and t represents the time, with a Δt time resolution of the input data. Note that F and H represent the internal model

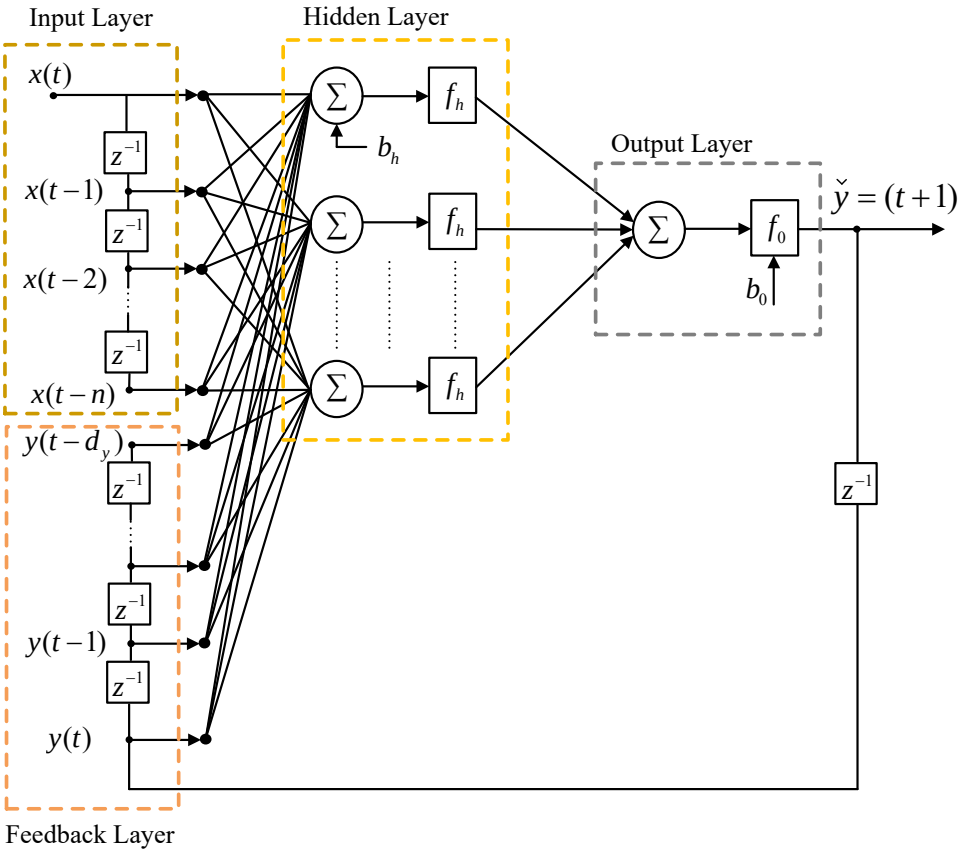

Figure 4.2: Recurrent NN topology (NARX)

of the NNs proposed for the aggregation of P and Q, respectively, and depends on the structure of these networks, i.e., number of layers, number of neurons per layer, weights connecting neurons between layers, the activation function of the neurons, etc. Observe also that the individual BESSs use $\hat{f}$, $\hat{V}$, and $\hat{P}_{ref}$ as input signals to their control systems, and therefore, are adequate as input signals for the black-box model, with $\hat{V}$ and $\hat{f}$ also having enough information of the system state. On the other hand, the signal $\hat{PV}$ provides information of the power injections of the distributed photovoltaic generation, which affect the system and BESS operation, and is independent from these two, and it thus needs to be taken into consideration as input.

Observe in (4.1) and (4.2) that n_x and n_y denotes measurements of past input and output data (delays), respectively, which should provide a large-enough window of past

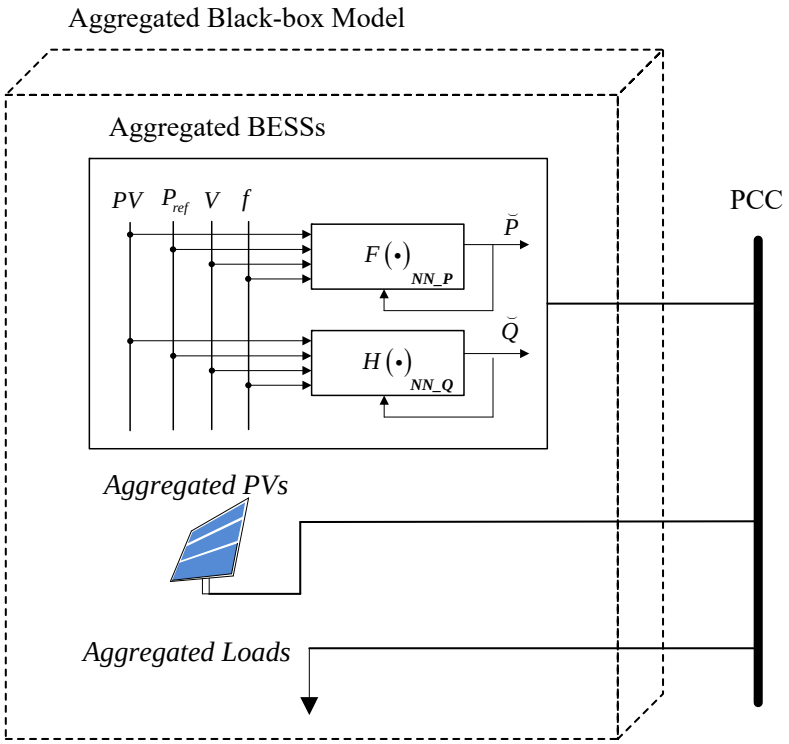

Figure 4.3: Proposed aggregated black-box model for distributed BESS.

information to capture the main dynamics of the BESSs response. The number of neurons in the input layer depends on the number of input signals considered in the model, which is 4 neurons in the present work, i.e., $\hat{f}$, $\hat{V}$, $\Delta\hat{P}_{ref}$, and $\hat{PV}$, and 1 neuron for the output $\check{P}$ or $\check{Q}$ at the output layer. The number of hidden layers is often challenging to determine; intuitively, larger number of hidden layers would more accurately represent complex systems, but it is not guaranteed, and would considerably increase the computation burden in training the NNs. The number of hidden layers is considered to be fixed at 4 in this thesis, and has been determined through trial and error, based on the available measurements.

4.1.2 Aggregated Load and PV Models

Aggregated loads and PV generation can be represented as follows [9]:

$$P_{eq_L} = \sum_j P_{L_{o_j}} V_j^{\alpha}, \quad Q_{eq_L} = \sum_j Q_{L_{o_j}} V_j^{\beta} \tag{4.3}$$

$$P_{eq_{PV}} = \sum_j P_{PV_{o_j}}, \quad Q_{eq_{PV}} = \sum_j Q_{PV_{o_j}} \tag{4.4}$$

where P_{L_o} and Q_{L_o}, and P_{PV_o} and Q_{PV_o}, are the aggregated active and reactive loads respectively, and aggregated active and reactive PV power injections of the PV generation, at each bus j of the distribution system. Note that this aggregation assumes that the PV generators are represented as constant negative power loads, as usual in ADNs where these systems operate in Constant P (Maximum Point Power Tracking or MPPT) and zero Q mode, as is the case nowadays for most of these PV sources, and the loads behave as voltage dependent loads, with α and β exponents for P and Q respectively, as is typically the case in dynamic studies [9], especially since these represent loads on distribution feeders.

Since measurements of the active and reactive power injections at the boundary bus, represent the aggregated effect of the entire distribution system, the power injections coming from the BESSs can be calculated by extracting the aggregated load (4.3) and PV generation (4.4), as follows:

$$P_{BESS} = P_{Bus} - P_{eq_{PV}} + P_{eq_L} \tag{4.5}$$

$$Q_{BESS} = Q_{Bus} - Q_{eq_{PV}} + Q_{eq_L} \tag{4.6}$$

where P_{Bus} and Q_{Bus} are the measurements of active and reactive power injections at the boundary bus, respectively. Note that the aggregated BESS measurements P_{BESS} and Q_{BESS} are independent of the type of load, since the loads are extracted from P_{Bus} and Q_{Bus} measurements.

4.1.3 Training and Testing

The training of the two proposed NNs is performed based on actual measured or simulated data, for $\mathscr{L}$ different time series obtained from $\mathscr{L}$ different events. In order to use this data for training, some pre-processing is necessary, for which the algorithm depicted in Figure 4.4 is used, as described next.

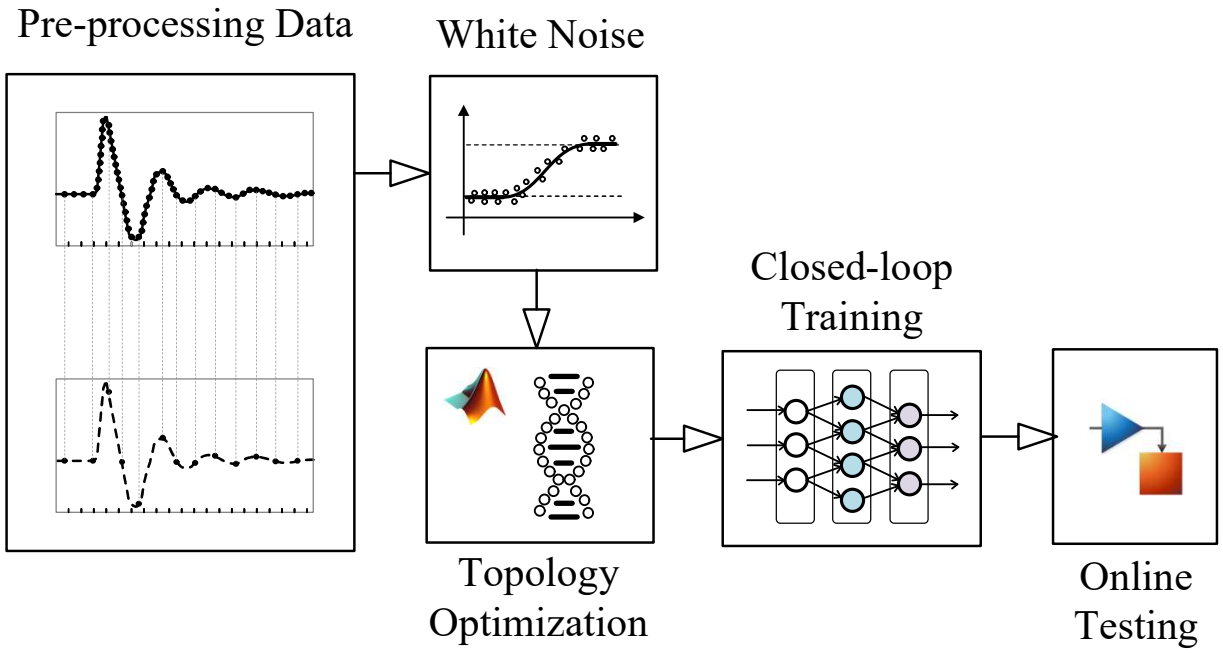

Figure 4.4: Algorithm used for NN data pre-processing and NN training.

Data Resolution

One of the benefits of using aggregated models is the reduction of the time step of the simulations, since detailed system responses, such as those associated with BESS' converter switches, are aggregated and thus simplified. Using data with high resolution increases the training time of NNs, which is critical if several NN topologies are to be tested, when, for example, an optimal configuration is needed. Hence, the first step in the proposed algorithm is to reduce the resolution of the training data, such that the main dynamics of the system are still captured. In BESSs, the relevant time constants associated with grid controllers are in the order of ms, therefore, the data resolution should be in that range.

Aggregated BESS Measurements

Once the lower-resolution data is obtained, the aggregated power measurements of the BESSs P and Q are calculated using (4.5) and (4.6) for each time series $l = 1,...,\mathscr{L}$. Then,

the aggregated per-unit values of $\hat{P}$ and $\hat{Q}$ are calculated as follows:

$$\hat{P}_{BESS} = \frac{P_{BESS}}{\sum_h S_h} \qquad \forall\, l = 1, ..., \mathscr{L} \tag{4.7}$$

$$\hat{Q}_{BESS} = \frac{Q_{BESS}}{\sum_h S_h} \qquad \forall\, l = 1, ..., \mathscr{L} \tag{4.8}$$

where S_h is the power rating of each individual BESS h connected at the distribution system.

White Noise Addition

White noise injection to the input data is performed before training, as this is a regularization technique used to reduce overfitting and improve the robustness of the NN, for better generalization and faster learning [71]. This helps prevent the NNs from becoming too sensitive to small disturbances or noise introduced due to model inaccuracies when used in simulations. The level of white noise creates a trade-off between accuracy and sensitivity, with the latter being observed during simulations only. Furthermore, since the output of the NNs are more sensitive to certain input signals, the level of white noise should be different for different inputs, and defined based on simulation results. Thus, white noise is added to the training data as follows:

$$x_{l,t} = \underline{x}_{l,t} + \mu_{l,t}\rho_x \max\left(\underline{\boldsymbol{x}}_l\right) \tag{4.9}$$

$$y_{l,t} = \underline{y}_{l,t} + \mu_{l,t}\rho_y \max\left(\underline{\boldsymbol{y}}_l\right) \tag{4.10}$$

where $\underline{x}_{l,t}$ is the reduced-resolution value of the input variable $x := \{\hat{f}, \hat{V}\}$ at time t, of the time series l; $\mu_{l,t} \sim U[0,1]$ is a random variable modeled as a uniformly distributed random process; $\underline{\boldsymbol{x}}_l$ is a vector containing all $\underline{x}_t$ of the times series l; and ρ_x is a parameter that defines the level of white noise added to the variable x with respect to its highest value in the series l, as illustrated in Figure 4.5. The same definitions apply for the output variables y.

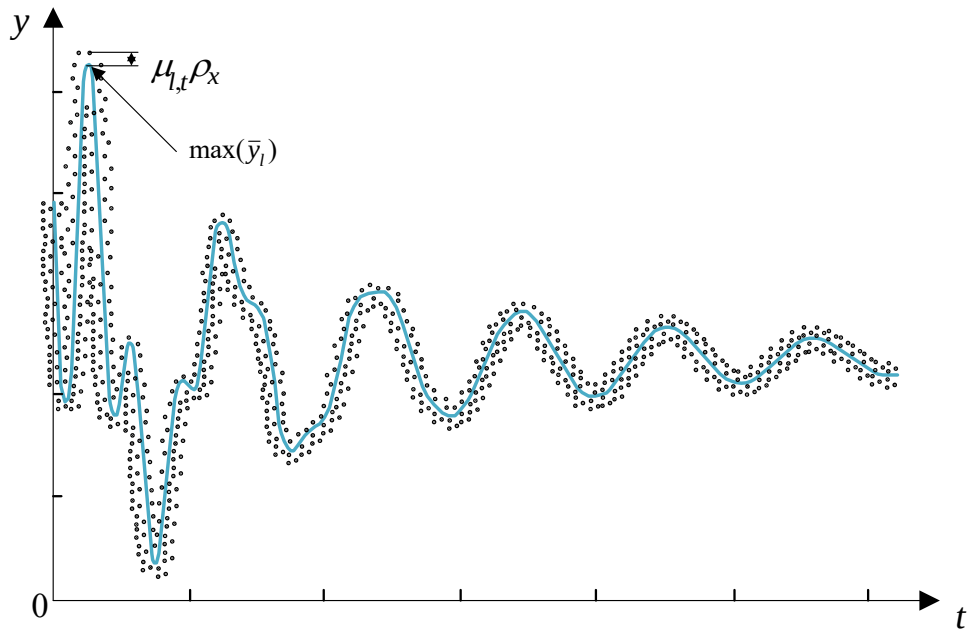

Figure 4.5: White noise addition technique for input and output signals.

Optimal NN Topology

The objective here is to find the vector $\boldsymbol{N}^* := [N_1^*, N_2^*, .., N_X^*]$ that contains the optimal number of neurons N_i^* per hidden layer i of the black-box NN model, which, minimizes the Mean Squared Error (MSE) of the NN prediction with respect to the actual measurements used as validation data, for all time series, assuming that the total number of hidden layers X is a fixed parameter in the model. Thus, considering the highly non-linear relation between performance and topology in a NN, a GA, which is a search-based optimization

technique, is used to determine $\boldsymbol{N}^*$ as follows:

$$
\begin{aligned}
\min_{\boldsymbol{N}} \quad & \text{MSE} = \frac{1}{\mathscr{L} \times M} \sum_{l=1}^{\mathscr{L}} \sum_{k} \xi_{l,k}^2 \\
\text{s.t.} \quad & \hat{y}_{l,k} - \check{y}_{l,k} - \xi_{l,k} = 0, \quad \forall\, k \\
& G \left(\begin{array}{c} \check{y}_{l,r-1}, \check{y}_{l,r-2}, ..., \check{y}_{l,r-n_y}, \\ \hat{f}_{l,r}, \hat{f}_{l,r-1}, ..., \hat{f}_{l,r-n_x}, \\ \hat{V}_{l,r}, \hat{V}_{l,r-1}, ..., \hat{V}_{l,r-n_x}, \\ \Delta\hat{P}_{ref_{l,r}}, \Delta\hat{P}_{ref_{l,r-1}}, ..., \Delta\hat{P}_{ref_{l,r-n_x}}, \\ \hat{PV}_{l,r}, \hat{PV}_{l,r-1}, ..., \hat{PV}_{l,r-n_x}, \\ \boldsymbol{w}, \boldsymbol{N} \end{array} \right) - \check{y}_{l,k} = 0, \\
& \qquad\qquad\qquad\qquad\qquad\qquad\qquad\qquad \forall\, k = r, l = 1, ..., \mathscr{L} \\
& \boldsymbol{1} \preceq \boldsymbol{N} \preceq \boldsymbol{N}_{\max} \\
& N_i \in \mathbb{Z}^+, \quad \forall\, i = 1, ..., X
\end{aligned}
\tag{4.11}
$$

where the vector $\boldsymbol{N} := [N_1, N_2, .., N_X]$ is part of the input variables of the NN function G, with r representing the index of all measured data points of the time series l; k is the index of the measured data points used for validation only of the time series l; M is the total number of data points k; $\mathscr{L}$ is the total number of time series; $\xi_{k,l}$ is the error of the predicted value $\check{y}_{l,k}$ with respect to the measurement $\hat{y}_{l,k}$ in p.u., using the nonlinear function G representing the NN; $\boldsymbol{w}$ is the vector of internal weights of the NN; and $\boldsymbol{N}_{\max}$ is a vector that contains the maximum number of neurons per layer i. Note that the only variables in this problem are the entries of the vector $\boldsymbol{N}$.

The optimization problem described in (4.11) is solved using a GA, where $\boldsymbol{N}$ is a member of the population C_e, updated at every generation $e+1$, based on the individuals $\boldsymbol{N}$ that had the best performance toward minimizing the objective function, i.e., minimum MSE on the validation data set. Note that, since the NN must be trained for each candidate solution $\boldsymbol{N}$ in order to obtain the output of G, and that the objective at this stage of the algorithm is to determine the optimal topology of NN, early stopping of the training process is enforced, which reduces the time required by the GA to solve the problem. The output of this stage is the optimal topology $\boldsymbol{N}^*$.

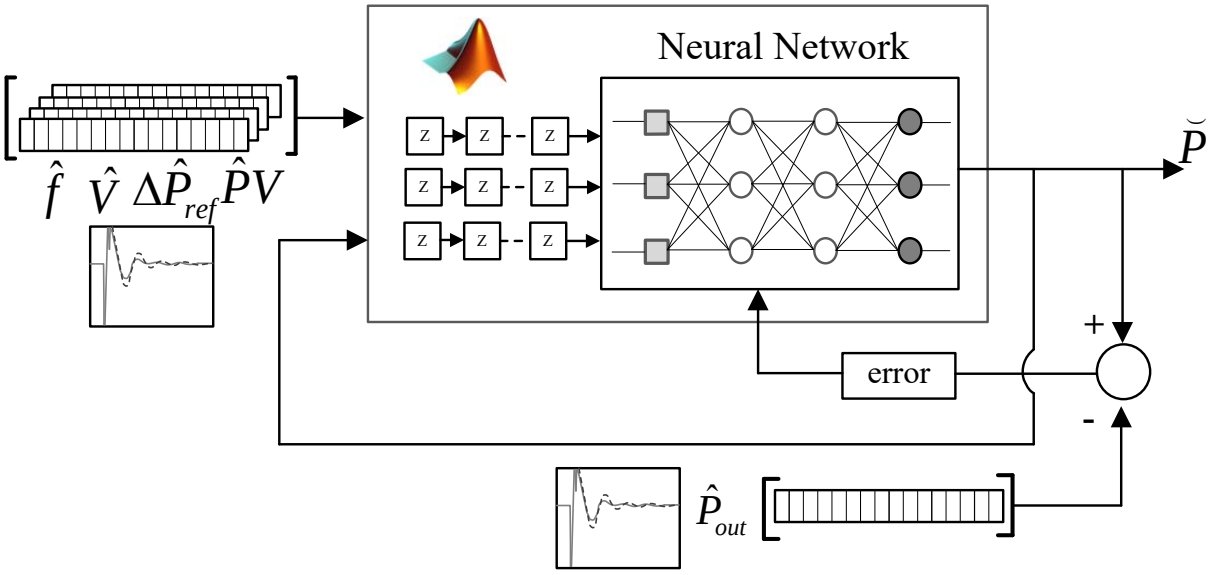

Figure 4.6: NNs training process.

Black-box Model Training

Finally, using $\boldsymbol{N}^*$, the NN is trained considering a larger number of maximum epochs to obtain the lowest possible error, and thus determine the optimal vector of weights $\boldsymbol{w}$, as shown in Figure 4.6.

4.2 Results

The aggregated BESS model is validated through simulations using the methodology proposed in Section 4.1, to obtain a black-box model of aggregated BESSs distributed within a modified version of the American CIGRE Medium-Voltage (MV) test ADN in [72], connected at Bus 5 of an also modified WSCC 9-bus benchmark transmission system [61], [64], which are both simulated in TSAT [60]. The aggregated BESS model is validated through simulations. Thus, the results discussed hereafter demonstrate the effectiveness of the proposed model to reproduce the behaviour of the detailed model, and without loss of generality, it should apply to any interconnected transmission and distribution grids, given the general and well-accepted dynamic models used in the presented simulations.

4.2.1 Test System

In order to reduce the simulation complexity, all loads and low-voltage networks are considered balanced and aggregated at the MV/LV transformers. All breakers in the system are closed, resulting in feeder loops. A high penetration of PV generation is assumed, with storage capacity spread across the distribution system, i.e., small units at households and larger units all aggregated at the MV level, corresponding to an equivalent 1.5 MVA PV and 1.5 MVA BESS at each of the 14 buses of the ADN, as depicted in Figure 4.7. The BESS are based on the model described in Chapter 2, and since the scope of this thesis is on BESS aggregation, simplified models for the loads and PV generation are used, as discussed in Section 4.1.2; thus, the loads are modeled as constant impedance loads, assuming α=β=2, and the PVs as negative constant power loads. The Bus 0 of the ADN is connected to Bus 5 of the WSCC 9-bus benchmark system, through a 115 kV/230 kV step-up transformer and transmission line which represents a sub-transmission system, whose parameters are extracted from [72]. Single-phase detailed representations of the BESS were implemented in Powertech's power system software package TSAT [60], requiring a time step of 0.101ms to ensure convergence, since the program did not converge with a 0.1ms time step.

The transmission system comprises one hydro generator Gen1, and two steam generators Gen 2 and Gen 3, which supply three loads, while also providing PFR and voltage control. The steady-state data of the WSCC 9-bus test system was extracted from [61], and its dynamic data from [64], including the machines' excitation systems and PSSs.

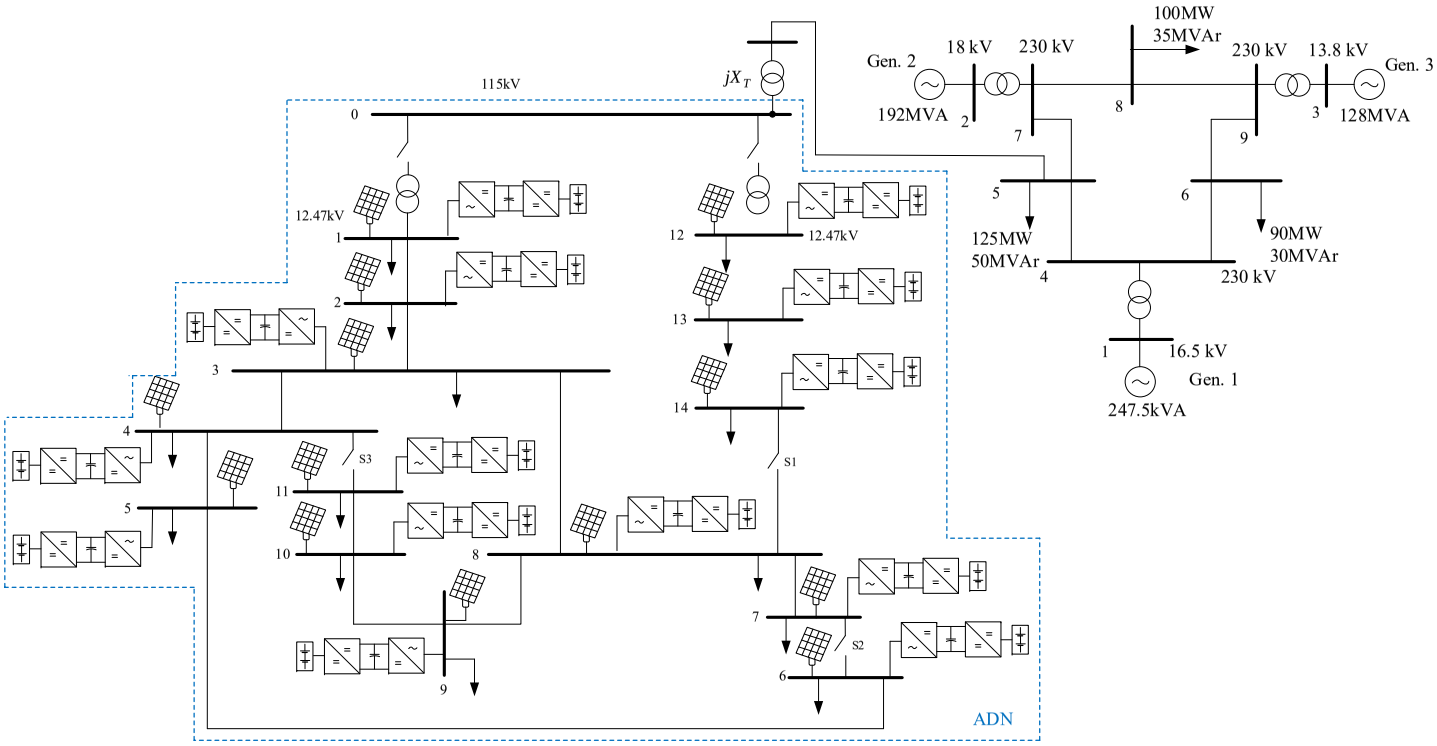

Figure 4.7: Transmission-ADN test system.

4.2.2 Simulated Cases

The BESS model discussed in Chapter 3 is used to simulate seven cases, in which contingencies are applied in the transmission system, while the BESSs are set to operate in different modes, i.e., PFR, Oscillation Damping (OD), and Constant Active Power (PC). Measurements of the active and reactive power injections, voltage, and frequency at Bus 0 of the ADN are recorded to obtain the aggregated BESS model. In all cases, the BESSs are set to initially operate in discharging mode, supplying 0.1 MW each, and the PVs injecting 0.75 MW, without loss of generality. Hence, in normal operating conditions, the ADN is consuming power from the transmission system. Also, to provide reactive power compensation, the BESSs provide voltage regulation at their local buses in all cases, to maintain the distribution system voltage within acceptable limits in the MV test system (between +6%/- 6% of the nominal [73]). Furthermore, step changes in the PV power are also simulated in all cases, to represent variations in the solar irradiance, as follows: {8 s, +0.1 p.u.}, {12 s, +0.1 p.u.}, and {14 s, -0.1 p.u.}.

The seven study cases are the following:

- Case 1: The power output of Gen 2 is reduced by 10% at t=3 s, to simulate a sudden loss of generation; all BESSs are set to operate in PFR mode using local frequency measurements (distributed control); and the PSS of the three generators are active.
- Case 2: Same as Case 1, but the power output of Gen 3 is reduced by 20% at t=3 s.
- Case 3: Same as Case 1 and 2, but the power output of Gen 1 is reduced by 30% at t=3 s.
- Case 4: A short circuit is applied at Bus 8 at t=3 s, and then removed after 50 ms, while all BESSs operate in OD mode, and the PSS of the three generators are disabled. In this case, the BESSs receive the same frequency signal (f at Bus 0) for the OD control, assuming that a single entity at the distribution system level controls the BESSs (centralized control).
- Case 5: Same as Case 4, but the short circuit is applied at Bus 6.
- Case 6: No contingency is simulated on the transmission system, but the reference output power of the 14 BESSs are changed by +0.5 p.u. (+ 0.75 MW) at t=3 s, when operating in PQ mode and in centralized control to simulate a sudden increase in the power supplied by the ADN.

- Case 7: Same as Case 6, but all BESS output powers are changed by -0.5 p.u. (+0.75 MW) at t=3 s, to simulate a sudden decrease in the power supplied by the ADN.

These cases are summarized in Table 4.1. The length of the simulations for all cases is 22s. Note that at least two time series per type of service and contingency are simulated, which activate most the BESSs' controller branches (except the constant power factor control) and excite the relevant system dynamics, which provide quality data to train the black-box model to accurately represent the aggregated BESSs for these contingencies, as well as untrained events, as demonstrated next.

Table 4.1: Simulated Cases

Case	Contingency	BESS Control			PSS
		P	Q	Input Signal	
1	-10%ΔP Gen 2	PFR	V Reg.	Local	Yes
2	-20%ΔP Gen 3	PFR	V Reg.	Local	Yes
3	-30%ΔP Gen 1	PFR	V Reg.	Local	Yes
4	Short circuit at Bus 8	OD	V Reg.	Central	No
5	Short circuit at Bus 6	OD	V Reg.	Central	No
6	+0.5ΔP_{BESS}	PC	V Reg.	Central	Yes
7	-0.5ΔP_{BESS}	PC	V Reg.	Central	Yes

The main assumptions in developing the aggregated BESS model are the following:

- All BESSs independently operate in the same control mode in each case, i.e., PFR, OD, and PC, as described in Section 3.2.1. Different control modes are used, depending on the contingency simulated.
- All BESSs regulate the local voltage in all cases.
- The input signals to the black-box BESS model are the per-unit bus frequency and voltage at the boundary bus between transmission and distribution systems, a signal proportional to the solar irradiance ($\hat{PV}$), and a signal proportional to the change in the BESSs' power reference ($\Delta\hat{P}_{ref}$).
- All PVs connected at the distribution level have the same power rating and produce the same active power.
- The nominal load values and ADN topology are the same in all cases.

- All BESSs have the same $\Delta\hat{P}_{ref}$ in Cases 6 and 7.
- The events simulated in the above cases are sufficient to excite the relevant internal dynamics of the BESSs.
- The BESSs are assumed to leave enough energy available to supply the power required by the system, i.e., SoC limits are not reached.

4.2.3 BESS Black-box Model Parameters

The methodology proposed in Section 4.1.3 is applied here to obtain the aggregated black-box BESS model, for which simulated measurements at Bus 0 of the ADN are used to train the two NNs, NN-P and NN-Q. The TSAT simulations used a data resolution of 0.101 ms, which represents around 220,000 data points per input per case; hence, training the NN with that resolution requires 7.7 million data points for the seven cases considered, for all the inputs and output feedback, per NN. This presents a computational challenge, because of the large number of operations required while adjusting the NNs' weights during training. Hence, the data resolution was reduced to 0.01 s, as explained in Section 4.1.3, which considerably reduced the computational burden, while capturing the main dynamics of the aggregated behaviour of the BESSs, relevant for typical transient stability studies. Furthermore, five measurements of past data of the inputs and outputs are used in (4.1) and (4.2), since these provide a large-enough window of historic information observed by the model, as demonstrated in the next section. The aggregation of the BESSs was performed using (4.5)-(4.8).

To determine the level of noise required to obtain adequate black-box models, a sensitivity analysis of the inputs to the NNs was performed, starting with finding the optimal NN configuration without considering white noise. Then, the NN with the optimal configuration was trained, adding white noise to the input data and observing how the MSE values change for the trained and untrained events, noticing that as the level of white noise increased, the MSE slightly increased for the trained events, but considerably decreased for the untrained events. Hence, the noise levels were increased until acceptable MSE values were obtained for both the trained and untrained events. These white noise levels were then applied to the input data to obtain a new optimal NN configuration. This empirical process yielded $\rho_x = \rho_y = 0.003$ for (4.9) and (4.10).

In [41], two hidden layers are proposed in an NN black-box model in order to represent the response of an aggregated system based on microturbines, to one type of disturbance

only. Here, in three different disturbances in the seven studied cases ($\mathscr{L} = 7$) are considered, which with the addition of PVs changing their output power, requires a more complex NN structure. Indeed, when less than 4 hidden layers were studied (e.g., 2 and 3), poor performance in the predictive capability of the NNs was observed, resulting in too many topologies. On the other hand, more than four layers increased considerably the domain of the problem, making it intractable, since the number of possible topologies increased exponentially with the number of hidden layers. Hence, four hidden layers ($X = 4$) for NN-P and NN-Q are considered, since it increases the capability of the NNs, while keeping the computational burden reasonable, and yielding adequate results as demonstrated here. Furthermore, the number of neurons per layer are constrained to 50, to reduce the population domain in the GA. The activation function used for the neurons is the sigmoid function. Each case described in Section 4.2.2 corresponds to the time series l that is used to train the NNs, with 70% of the available data of each time series being used for training, 25% for validation, and 5% for testing.

The following optimization problems, illustrated in Figure 4.8, are then solved using GAs, to obtain the optimal topology of NN-P and NN-Q:

$$
\begin{aligned}
\min_{\boldsymbol{N_P}} \quad & \text{MSE} = \frac{1}{7 \times M} \sum_{l=1}^{7} \sum_{k} \xi_{P_{l,k}}^2 \\
\text{s.t.} \quad & \hat{P}_{l,k} - \check{P}_{l,k} - \xi_{P_{l,k}} = 0, \quad \forall\, k \\
& F \left(\begin{array}{c} \check{P}_{l,r-1}, \check{P}_{l,r-2}, ..., \check{P}_{l,r-5}, \\ \hat{f}_{l,r}, \hat{f}_{l,r-1}, ..., \hat{f}_{l,r-5}, \\ \hat{V}_{l,r}, \hat{V}_{l,r-1}, ..., \hat{V}_{l,r-5}, \\ \Delta\hat{P}_{ref_{l,r}}, \Delta\hat{P}_{ref_{l,r-1}}, ..., \Delta\hat{P}_{ref_{l,r-5}}, \\ \hat{PV}_{l,r}, \hat{PV}_{l,r-1}, ..., \hat{PV}_{l,r-5}, \\ \boldsymbol{w}_p, \boldsymbol{N_p} \end{array} \right) - \check{P}_{l,r} = 0, \\
& \qquad\qquad\qquad\qquad\qquad\qquad\qquad\qquad \forall\, r \wedge l = 1, ..., 7 \\
& \mathbf{1} \preceq \boldsymbol{N_P} \preceq N_{P_{\max}} \boldsymbol{I} \\
& N_{P_i} \in \mathbb{Z}^+, \quad \forall\, i = 1, ..., 4
\end{aligned}
\tag{4.12}
$$

$$
\begin{aligned}
\min_{\boldsymbol{N_Q}} \quad & \text{MSE} = \frac{1}{7 \times M} \sum_{l=1}^{7} \sum_{k} \xi_{Q_{l,k}}^2 \\
\text{s.t.} \quad & \hat{Q}_{l,k} - \check{Q}_{l,k} - \xi_{Q_{l,k}} = 0, \quad \forall\, k \\
& H \left(\begin{array}{c} \check{Q}_{l,r-1}, \check{Q}_{l,r-2}, ..., \check{Q}_{l,r-5}, \\ \hat{f}_{l,r}, \hat{f}_{l,r-1}, ..., \hat{f}_{l,r-5}, \\ \hat{V}_{l,r}, \hat{V}_{l,r-1}, ..., \hat{V}_{l,r-5}, \\ \Delta\hat{P}_{ref_{l,r}}, \Delta\hat{P}_{ref_{l,r-1}}, ..., \Delta\hat{P}_{ref_{l,r-5}}, \\ \hat{PV}_{l,r}, \hat{PV}_{l,r-1}, ..., \hat{PV}_{l,r-5}, \\ \boldsymbol{w}_Q, \boldsymbol{N_Q} \end{array} \right) - \check{Q}_{l,r} = 0, \\
& \qquad\qquad\qquad\qquad\qquad\qquad\qquad\qquad \forall\, r \wedge l = 1, ..., u \\
& \mathbf{1} \preceq \boldsymbol{N_Q} \preceq N_{Q_{\max}} \boldsymbol{I} \\
& N_{Q_i} \in \mathbb{Z}^+, \quad \forall\, i = 1, ..., 4
\end{aligned}
\tag{4.13}
$$

A summary of the parameters for (4.12) and (4.13) is presented in Table 4.2. The size of

Table 4.2: NN-Based Black-box Model Configuration

Parameter	Value	Parameter	Value
n_x	5	n_y	5
$N_{P_{\max}}$	50	$N_{Q_{\max}}$	5
M	550	$\mathscr{L}$	7
X	4		

the population of the GA is 1000 individuals, and the maximum number of epochs for the training of each candidate NN is limited to 500. The convergence criteria used for the GA is a maximum of 200 generations, or 50 consecutive generations without any reduction in the minimum MSE. The evolution of the MSE of NN-P and NN-Q, per generation, is presented in Figure 4.9. More than 92,000 different candidate topologies for NN-P and NN-Q were trained and validated against their corresponding available measurements, resulting in the optimal configurations: $\boldsymbol{N_P}^* = [40, 16, 37, 5]$ and $\boldsymbol{N_Q}^* = [23, 49, 33, 19]$, being the number of neurons in each NN's hidden layers.

Based on $\boldsymbol{N_P}^*$ and $\boldsymbol{N_Q}^*$, the NN-P and NN-Q are then obtained by increasing the maximum number of epochs for training to 1000. The performance regression of prediction using NN-P and NN-Q for the training and validation data is presented in Figure 4.10. Note that a good prediction was obtained, yielding correlation coefficients close to unity. The MSE of the validation data considering the seven time series for NN-P and NN-Q were

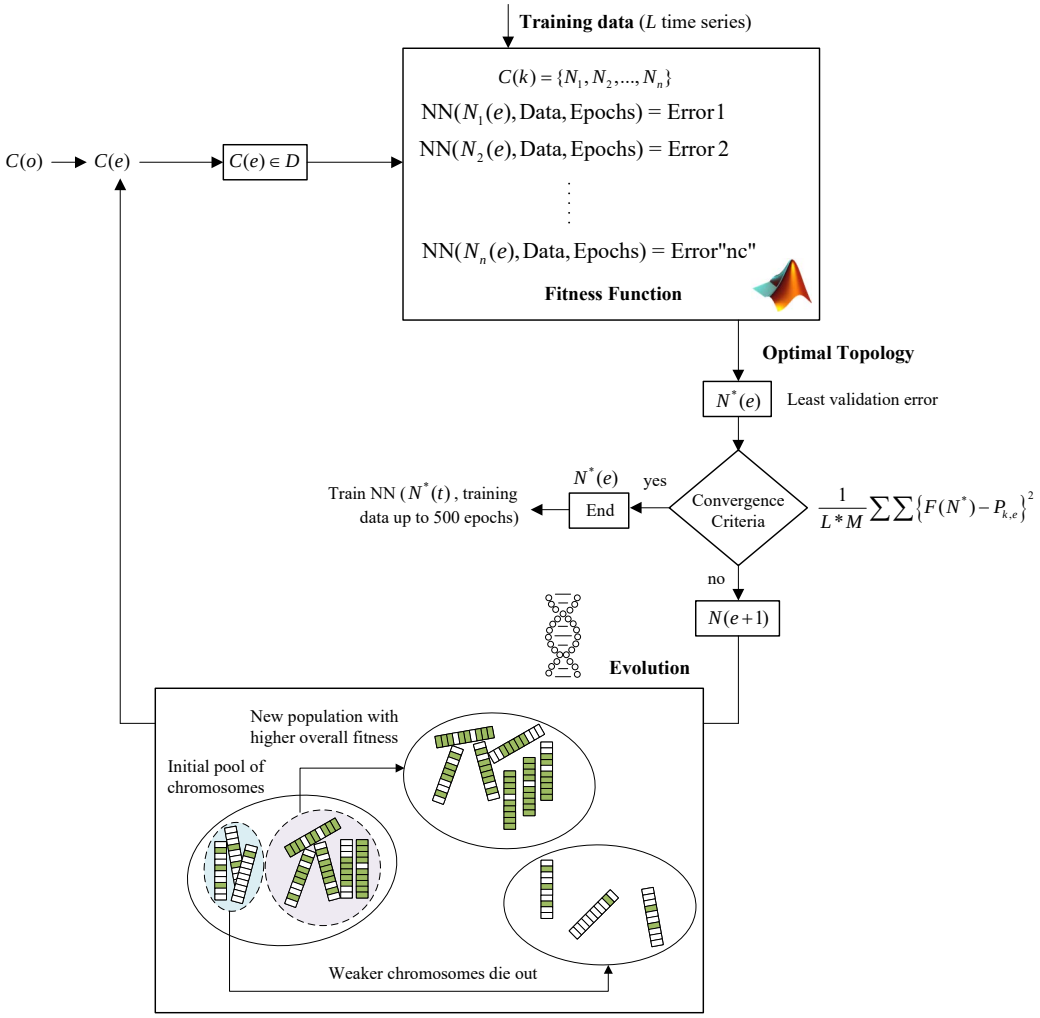

Figure 4.8: Optimal topology optimization process.

7.499×10^{-5} p.u. and 1.282×10^{-5} p.u., respectively.

4.2.4 Model Validation in Simulink

In order to validate the proposed aggregated BESS black-box model in simulations, the transmission system discussed in Section 4.2.1 with the proposed NN-P and NN-Q aggregated BESS models were implemented in Matlab Simulink. The black-box model is

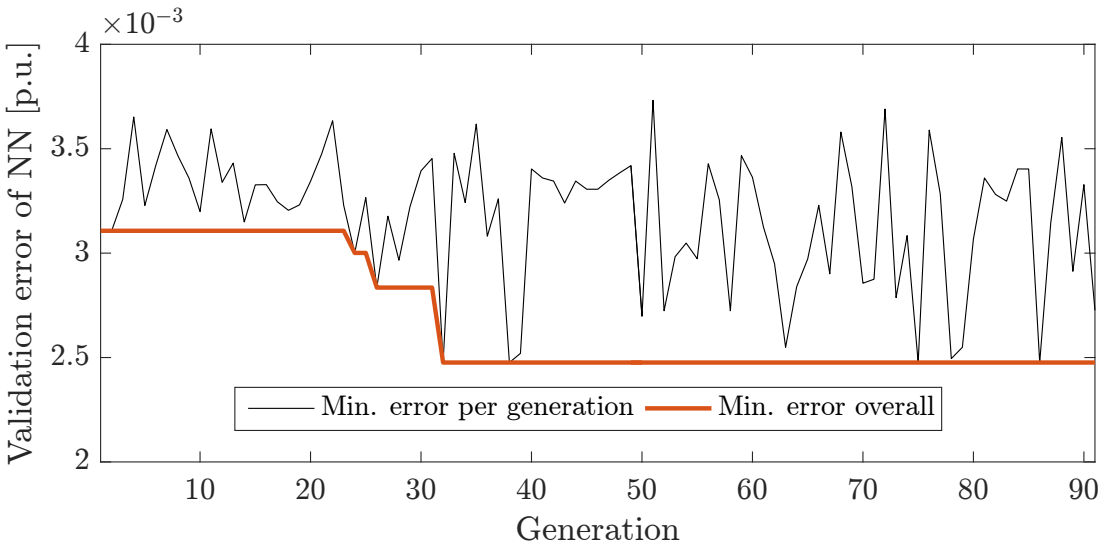

(a)

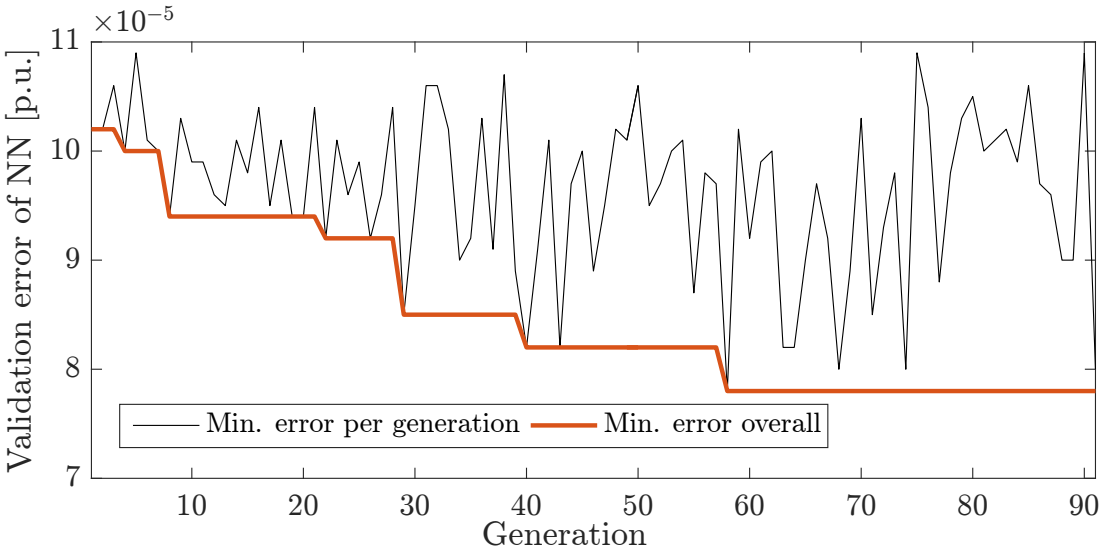

(b)

Figure 4.9: Evolution of the MSE per generation of (a) NN-P and (b) NN-Q.

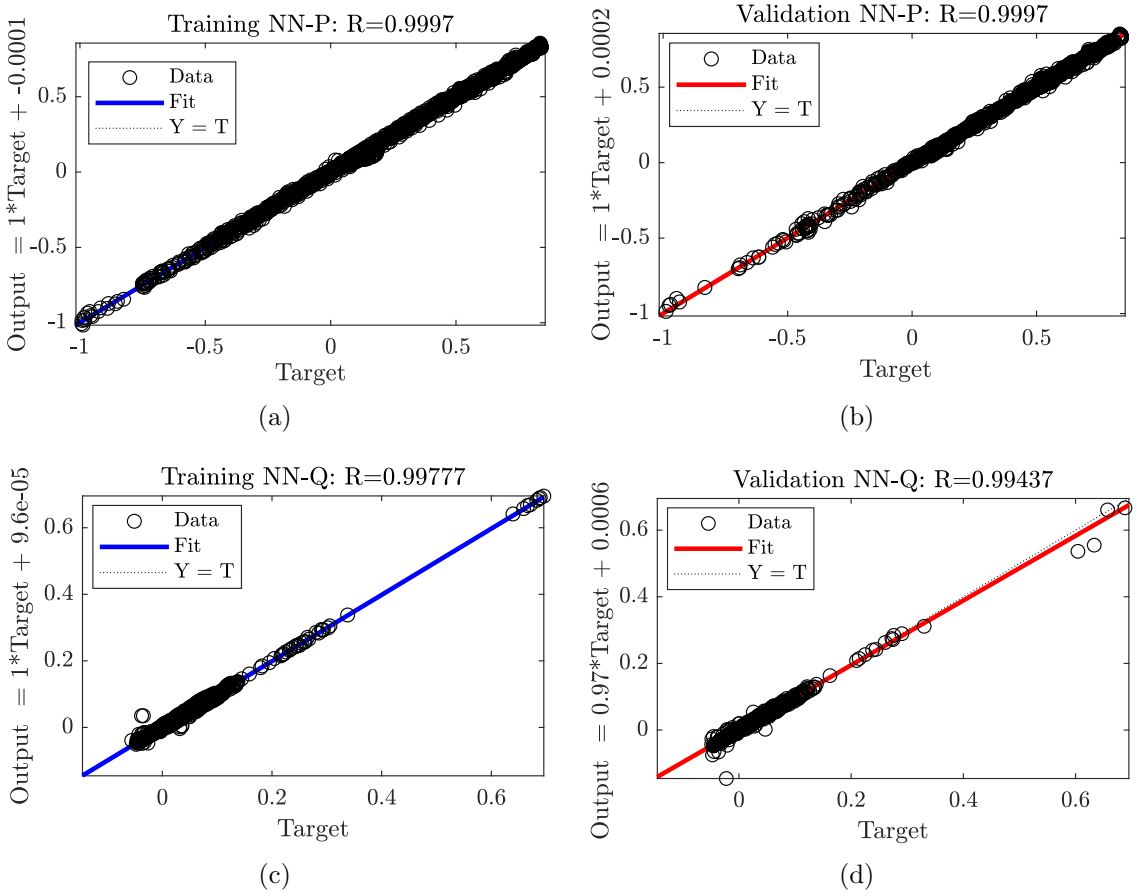

Figure 4.10: Correlation coefficient R for (a) training and (b) validation data for NN-P, and (c) training and (d) validation data for NN-Q.

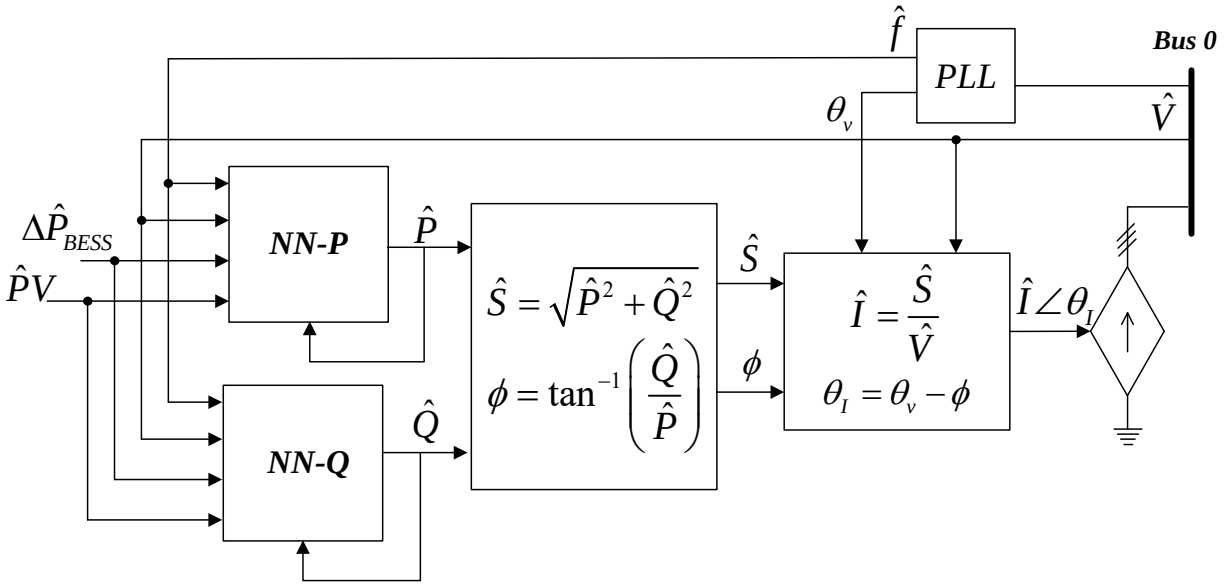

Figure 4.11: Simulink interface for the aggregated BESS model.

effectively integrated in the simulations as a controllable current source connected at Bus 0, which requires the interface presented in Figure 4.11. Note that $\check{P}$ and $\check{Q}$ are used to calculate the current I injected at Bus 0, by dividing the aggregated BESS apparent power S by the measured terminal voltage V, while the current angle θ_I is obtained by subtracting the power factor angle ϕ from the voltage phase angle θ_V. The frequency measurements f and θ_V are obtained through a PLL circuit.

A comparison between the detailed model and simulations based on the proposed aggregated black-box BESS models was performed for all the cases described in Section 4.2.2. In Figures 4.12 to 4.25 the simulation results for all cases are presented.

In Cases 1, 2, and 3 (Figures 4.12 to 4.17), the BESSs, operating in local control mode, provides PFR, thus increasing their active power injections to help stabilize the dropping frequency, resulting from the power reduction of the generators in the transmission system. Notice that the system frequency is also affected by the changes in the PV generation within the distribution system, which occurs at 8 s, 12 s, and 14 s; furthermore, since the $\hat{PV}$ input signal to the NN-P and NN-Q also changes at these times, fast transients that quickly disappear are observed in $\hat{P}$ and $\hat{Q}$. Observe that NN-P can accurately reproduce the aggregated active power injections $\hat{P}$. On the other hand, NN-Q outputs follow very closely the reactive power curves obtained with the detailed model with a small offset,

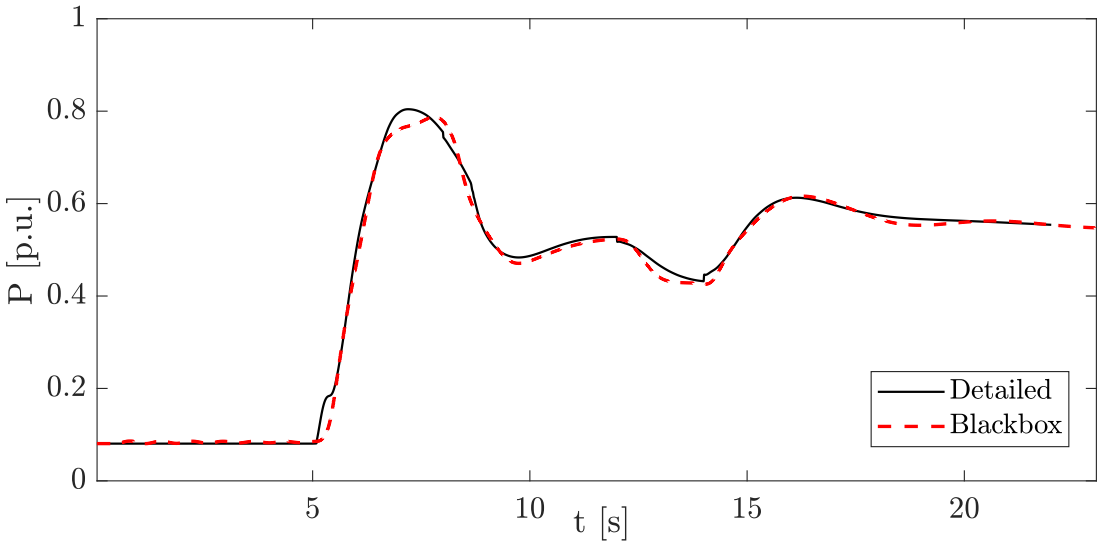

(a)

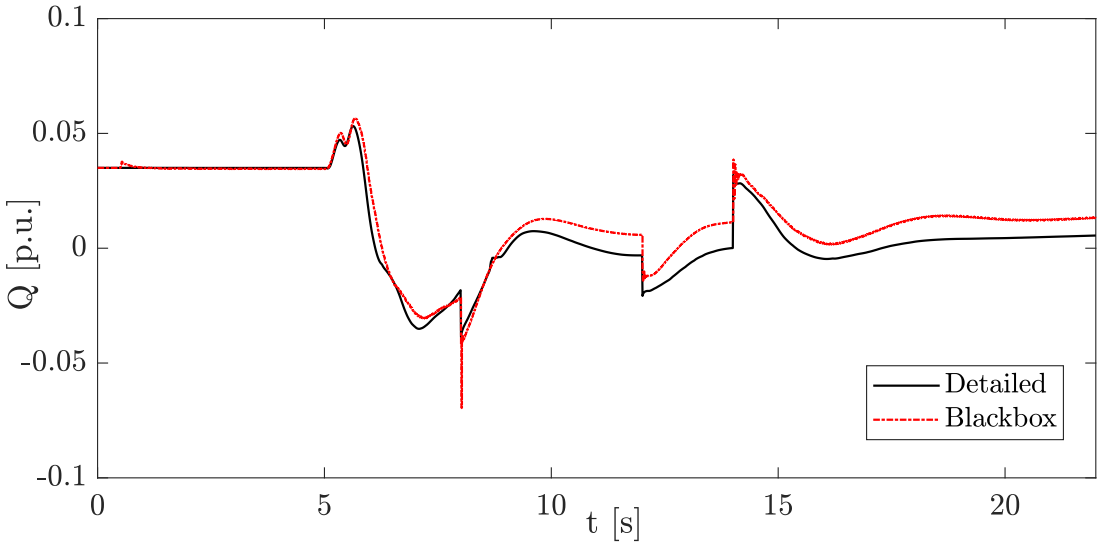

(b)

Figure 4.12: Aggregated BESS output for Case 1 (a) $\hat{P}$, (b) $\hat{Q}$.

which is due to the fact that the initial steady-state voltage at Bus 0 in the Simulink simulations is slightly larger than that in the original TSAT detailed model, as observed in Figures 4.12b, 4.14b and 4.16b. Furthermore, the variations in the PVs generation has

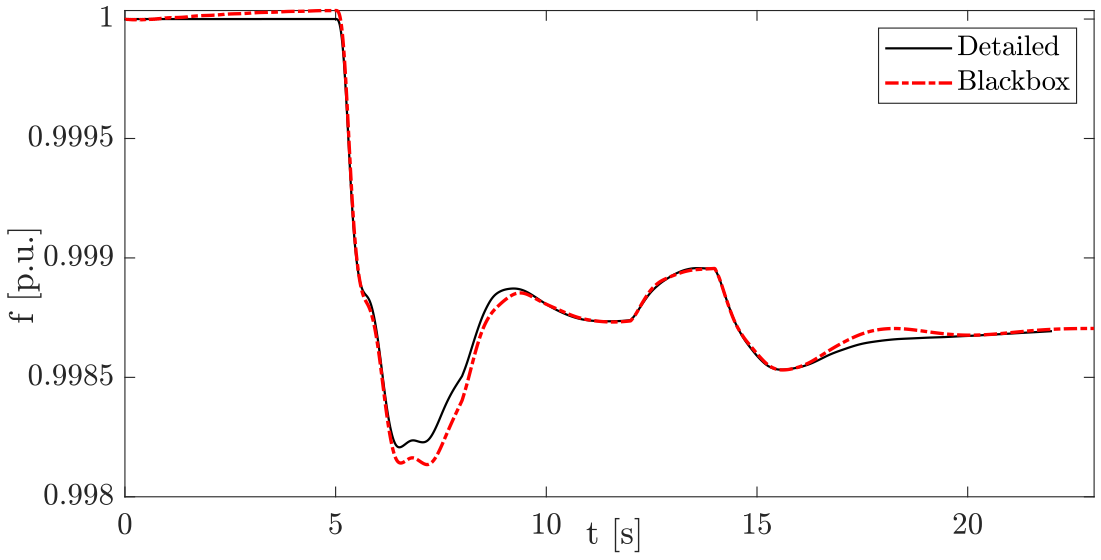

(a)

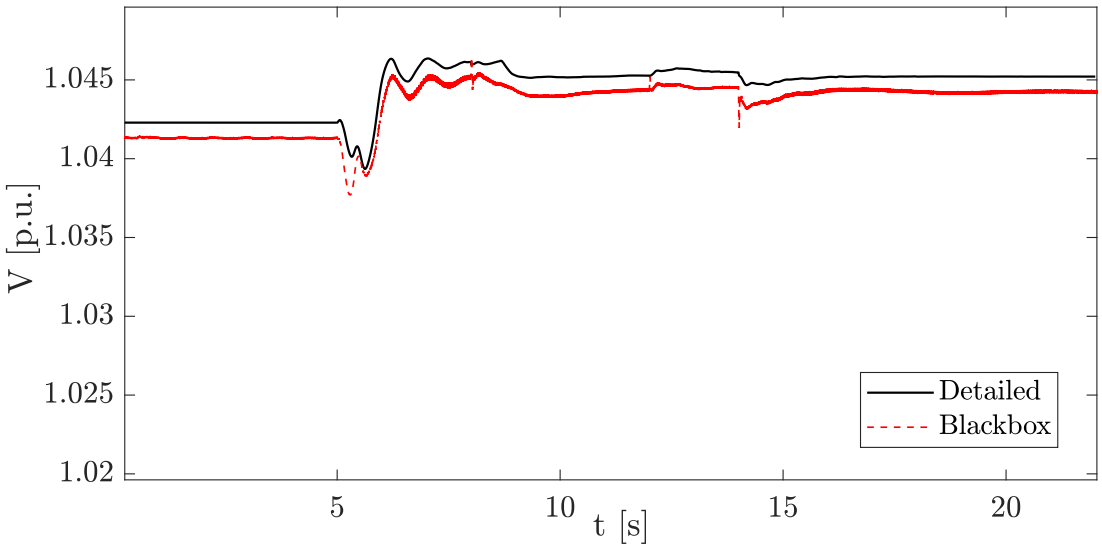

(b)

Figure 4.13: System performance in Case 1 (a) $\hat{f}$, and (b) $\hat{V}$.

a direct impact on the voltage regulation capability of the BESS, as the PV sources are physically located at the same buses as the BESSs.

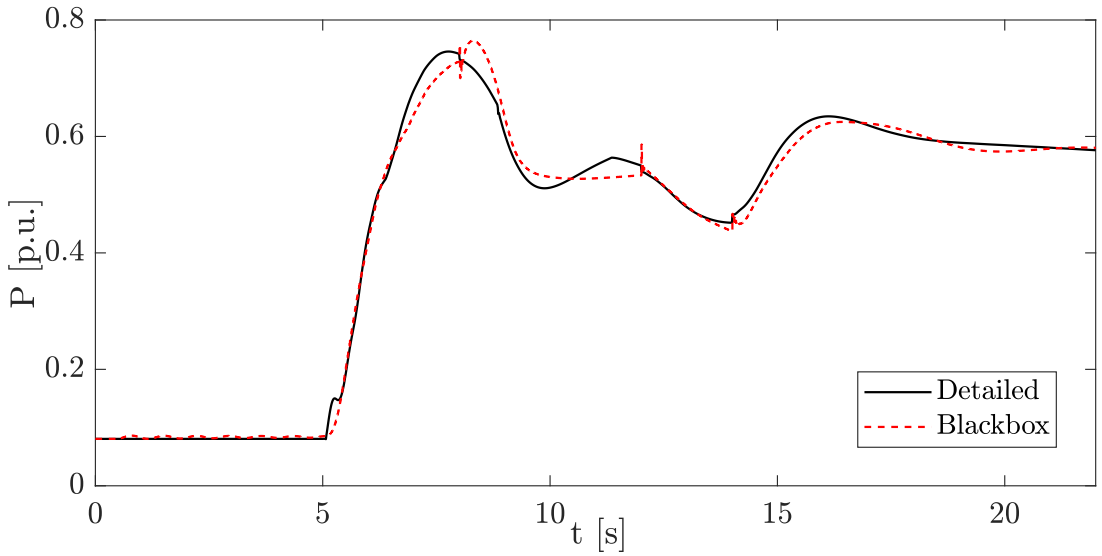

(a)

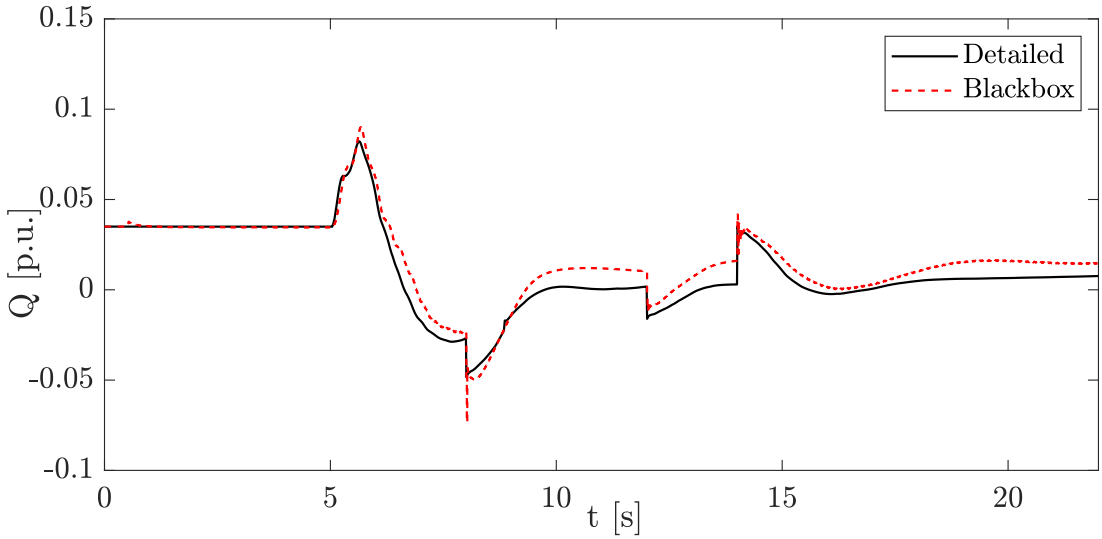

(b)

Figure 4.14: Aggregated BESS output for Case 2 (a) $\hat{P}$, (b) $\hat{Q}$.

The results for Cases 4 and 5 (Figures 4.18 to 4.21), demonstrate, first, that proper control of distributed BESSs can help to damp low-frequency oscillations at the transmission

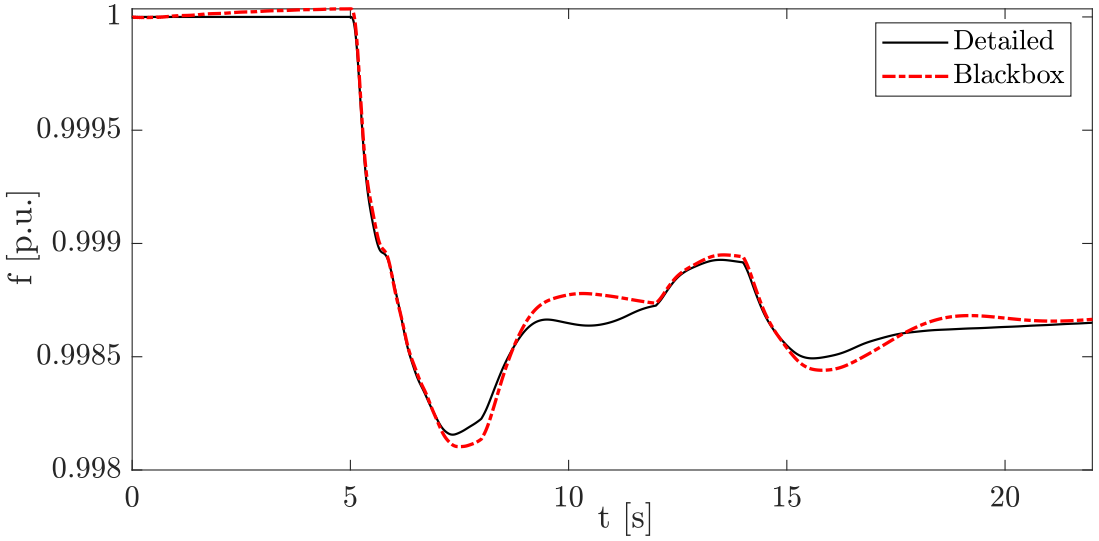

(a)

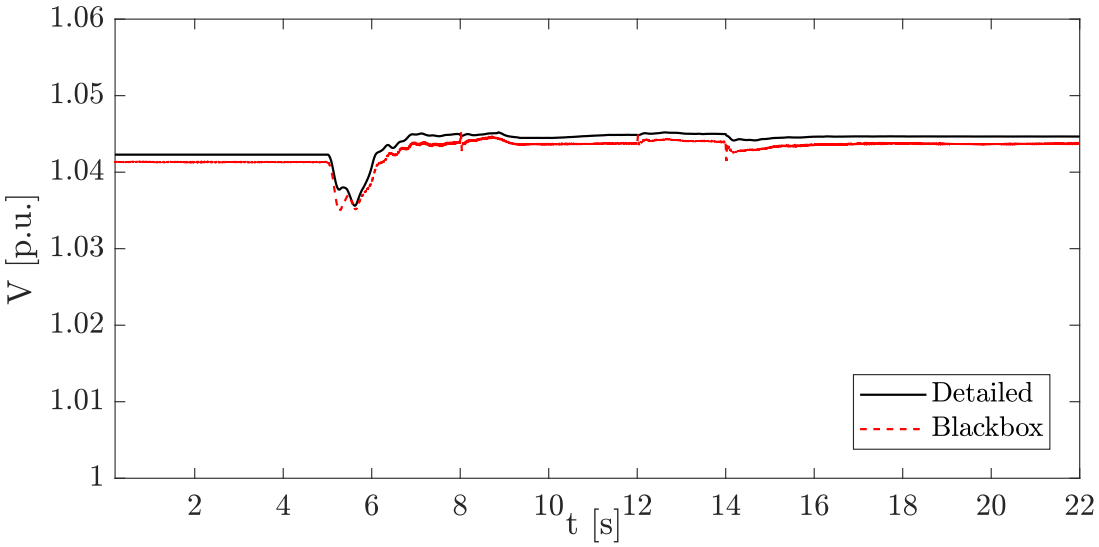

(b)

Figure 4.15: System performance in Case 2 (a) $\hat{f}$, and (b) $\hat{V}$.

level, and, second, that the proposed NN-P and NN-Q are able to properly represent the aggregated BESS response, even though the system response is considerably different from

those obtained in the previous cases. Notice that NN-P tends to produce $\hat{P}$ values slightly larger than those in the detailed model, thus reducing the system oscillations faster. Similar results are observed in Cases 6 and 7 (Figures 4.22 to 4.25), where, while $\hat{P}$ remains constant, changing only when NN-P receives a $\Delta\hat{P}_{ref}$ command, $\hat{Q}$ varies according to the voltage regulation requirements at the local buses.

Based on the aforementioned results, the proposed black-box model is shown to be robust enough with respect to grid component model inaccuracies, as the measurements were obtained in TSAT [60], while the black-box model simulations were performed on Matlab's Simscape based on three-phase models [74], with somewhat different component models. Furthermore, note that the interface depicted in Figures 4.11 was introduced to connect the black-box model to the transmission grid in Simscape, as opposed to the BESSs being directly connected to the system as in the case of the TSAT simulations.

In order to demonstrate the generalization capability of the proposed model, two additional cases, for which the NNs were not trained, were simulated. Thus, in Figures 4.26 and 4.27, the response of the aggregated BESSs providing PFR, for a reduction of 5% in the power output of Gen 2 (Case 8) is presented; and in Figures 4.28 and 4.29, their aggregated response while providing oscillation damping for a 50 ms short circuit at Bus 9 of the transmission system (Case 9) is depicted. Observe that the main trend of $\hat{P}$ and $\hat{Q}$ are still adequately reproduced in both cases, with a more significant difference for $\hat{P}$ and $\hat{Q}$ in Case 8.

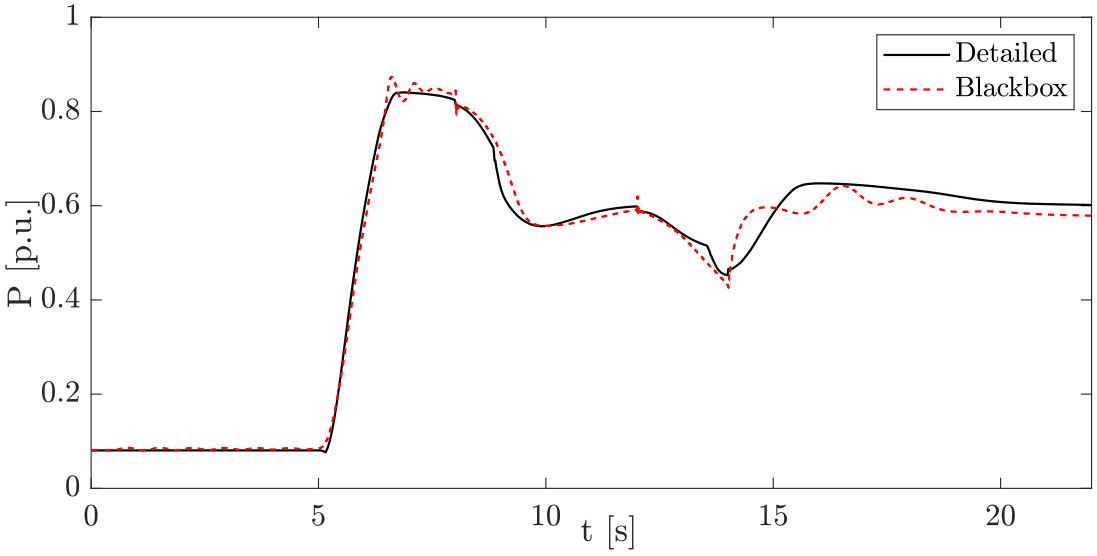

(a)

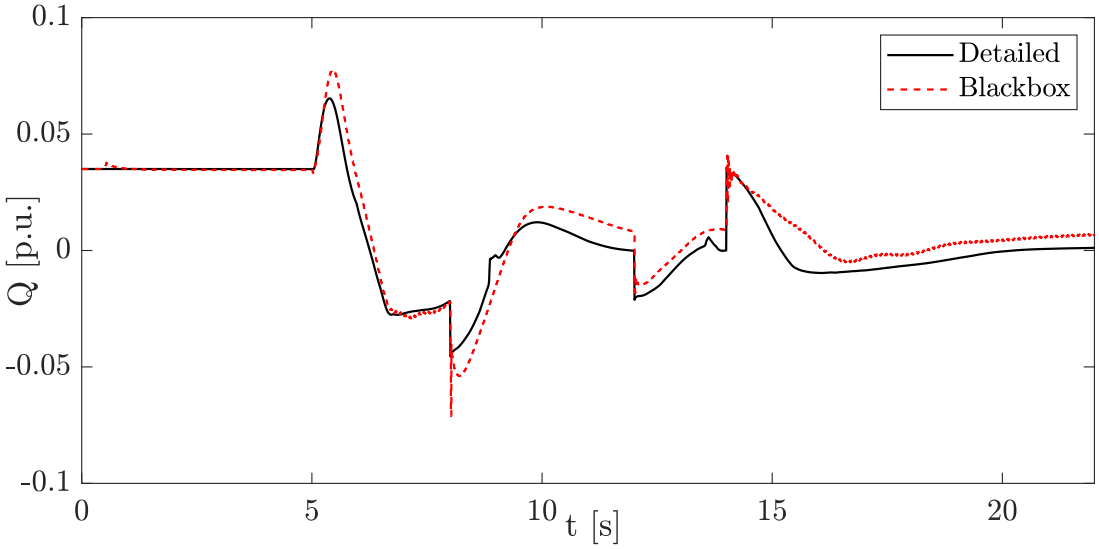

(b)

Figure 4.16: Aggregated BESS output for Case 3 (a) $\hat{P}$, (b) $\hat{Q}$.

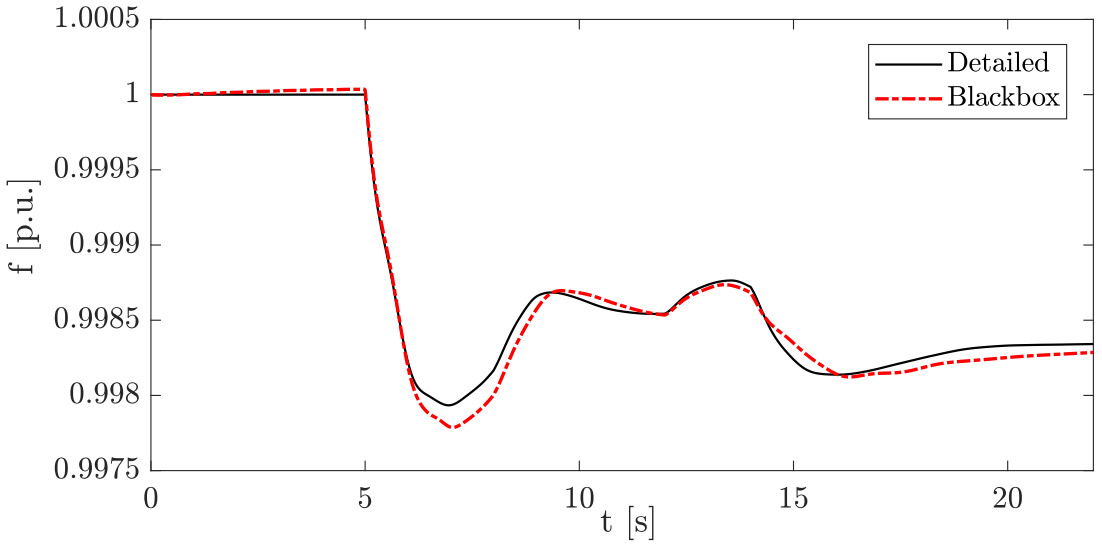

(a)

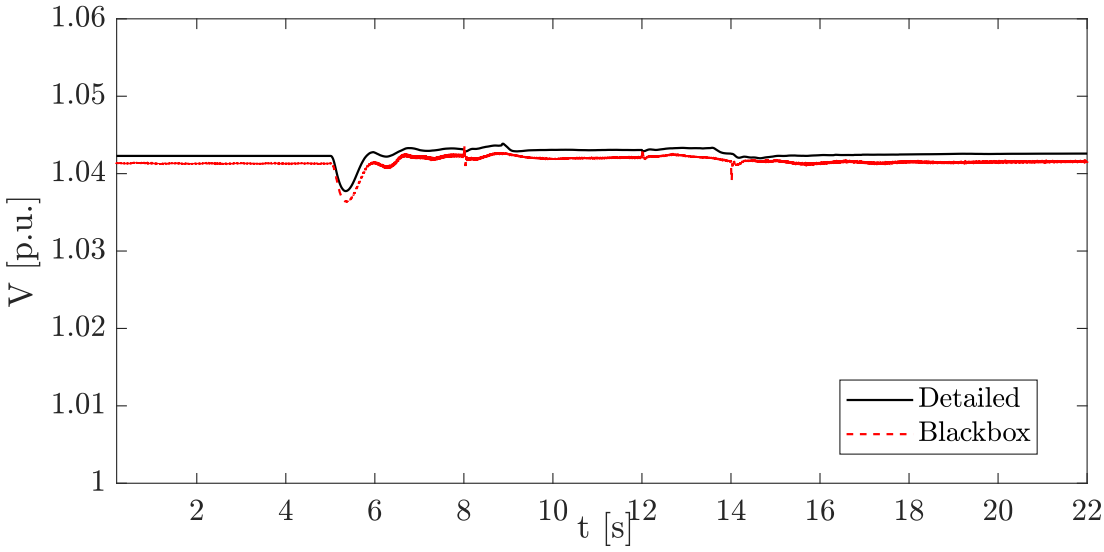

(b)

Figure 4.17: System performance in Case 3 (a) $\hat{f}$, and (b) $\hat{V}$.

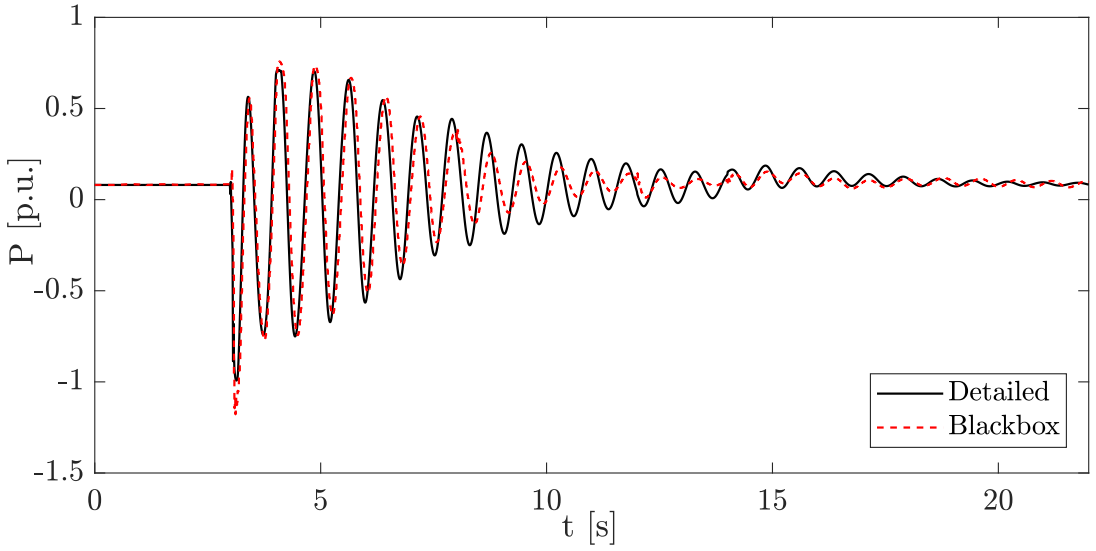

(a)

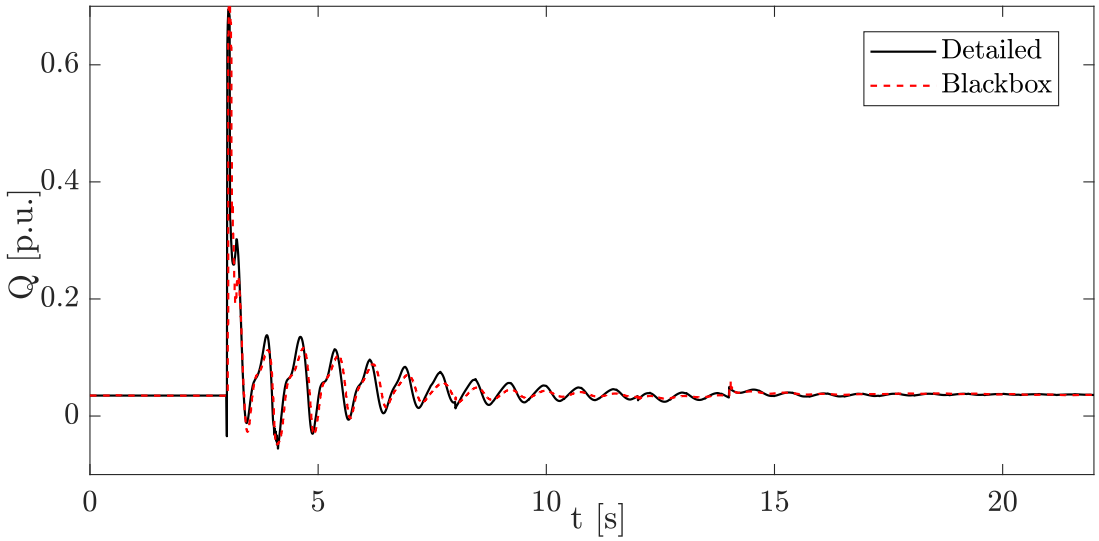

(b)

Figure 4.18: Aggregated BESS output for Case 4 (a) $\hat{P}$, (b) $\hat{Q}$.

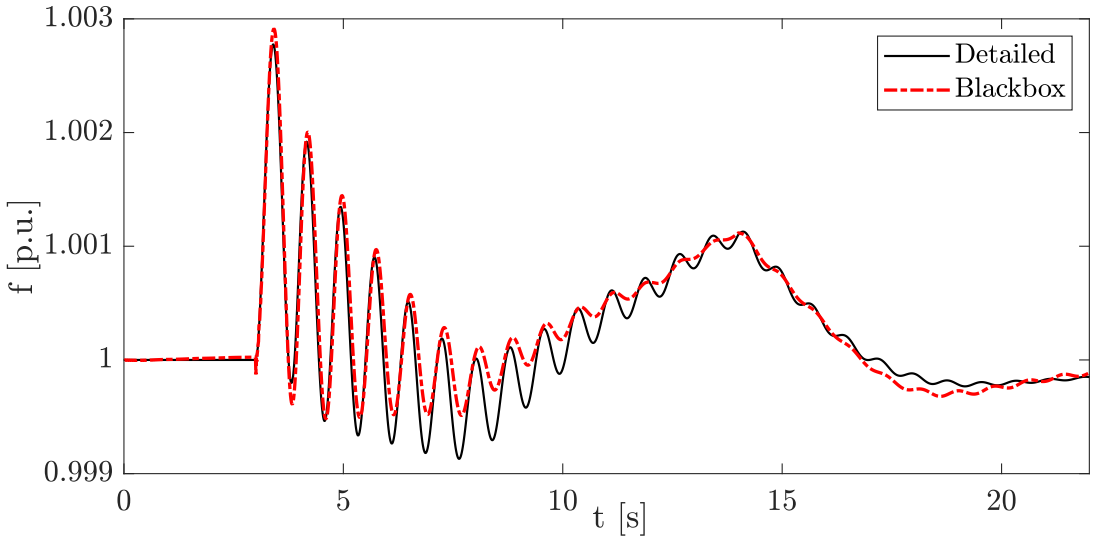

(a)

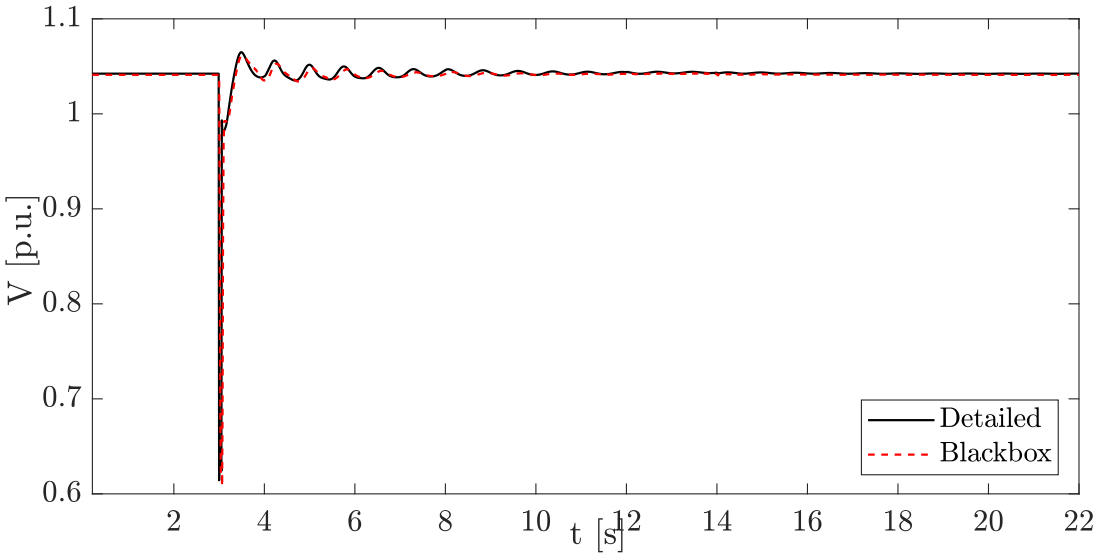

(b)

Figure 4.19: System performance in Case 4 (a) $\hat{f}$, and (b) $\hat{V}$.

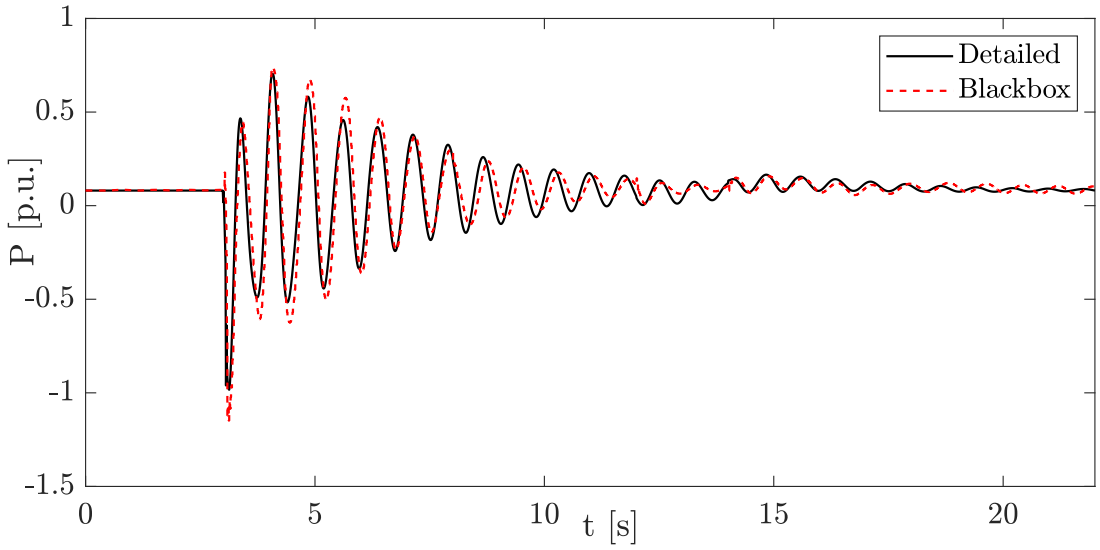

(a)

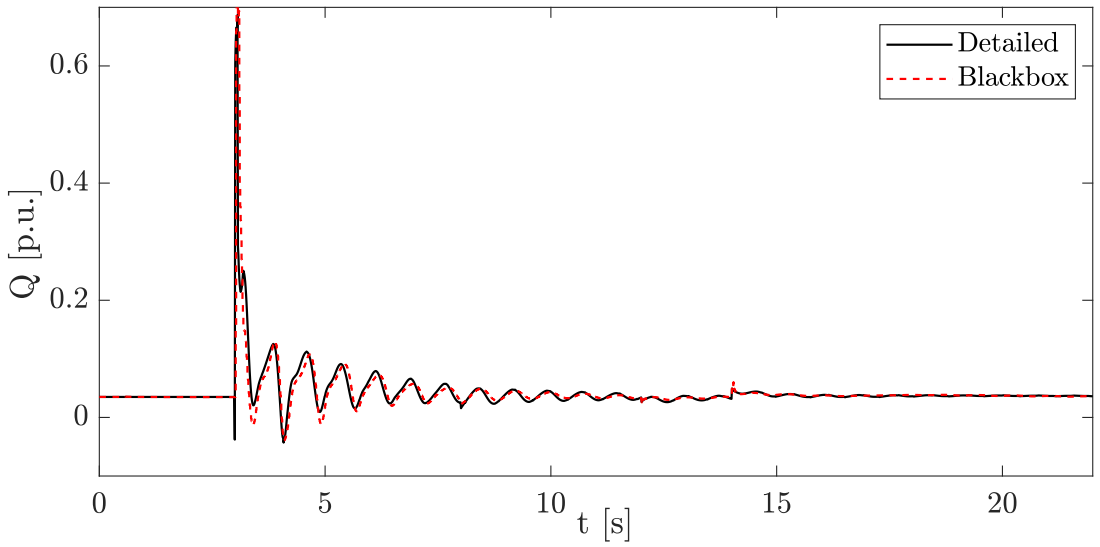

(b)

Figure 4.20: Aggregated BESS output for Case 5 (a) $\hat{P}$, (b) $\hat{Q}$.

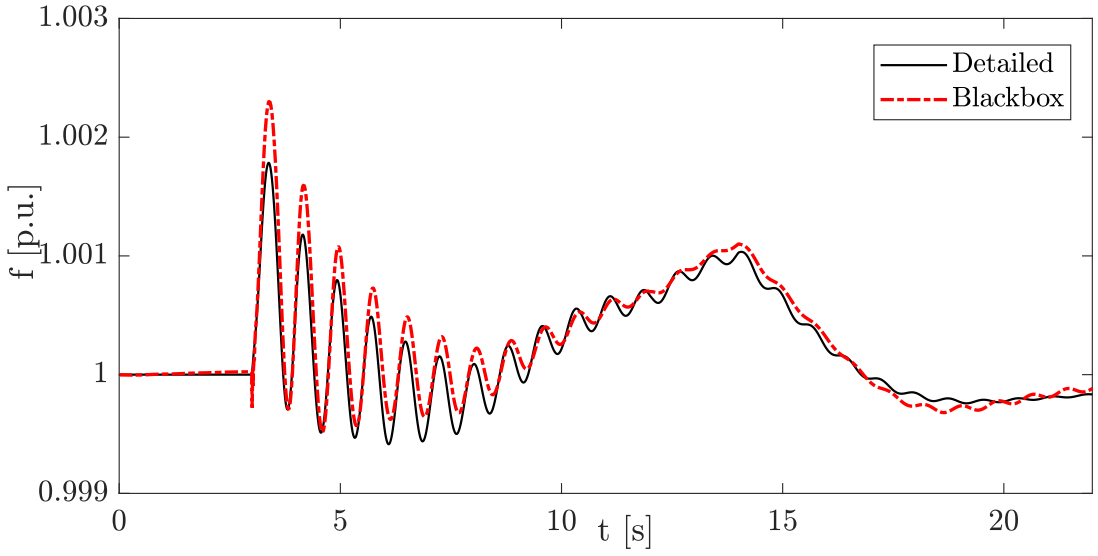

(a)

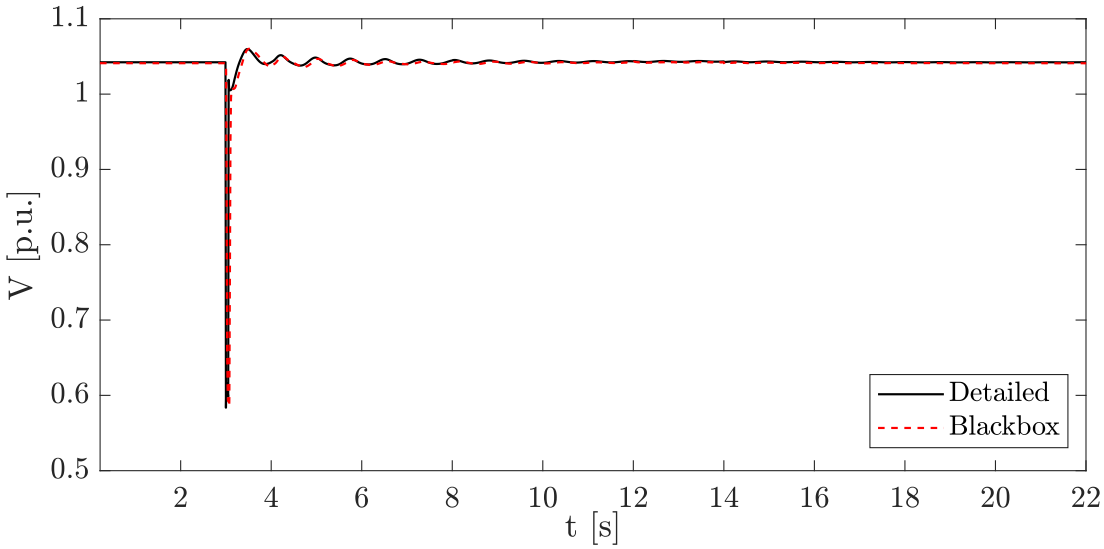

(b)

Figure 4.21: System performance in Case 5 (a) $\hat{f}$, and (b) $\hat{V}$.

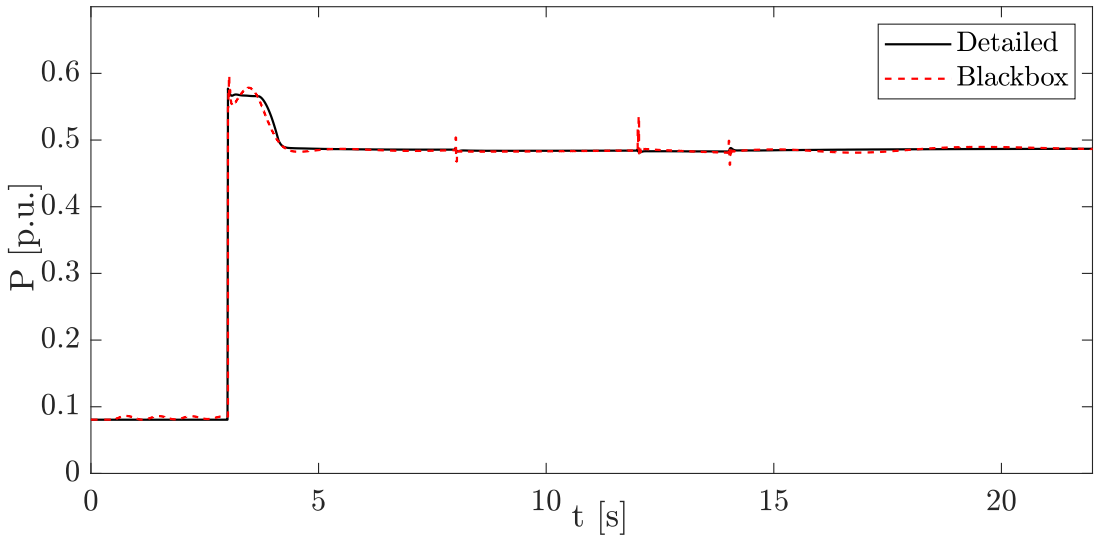

(a)

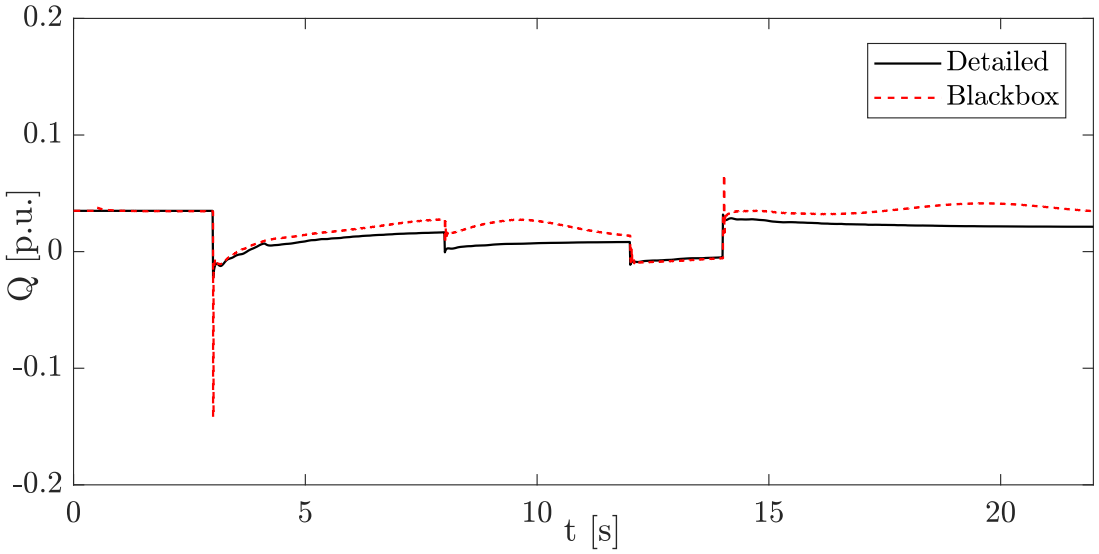

(b)

Figure 4.22: Aggregated BESS output for Case 6 (a) $\hat{P}$, (b) $\hat{Q}$.

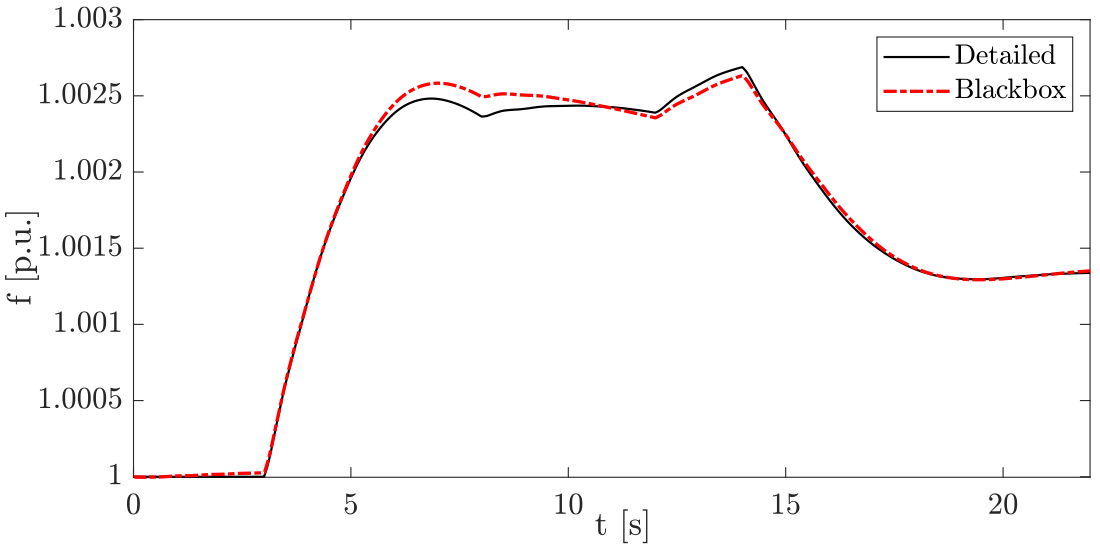

(a)

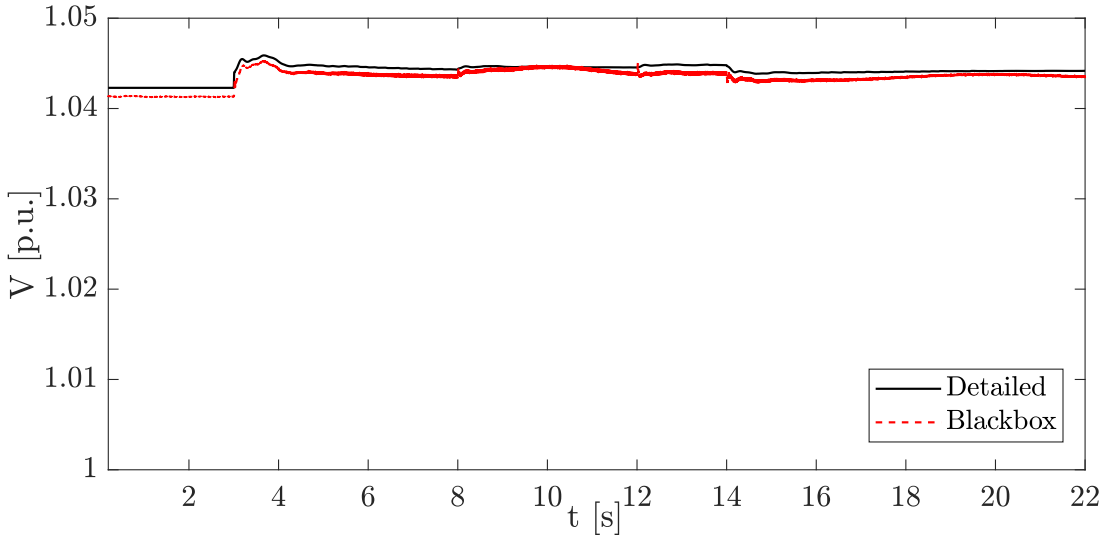

(b)

Figure 4.23: System performance in Case 6 (a) $\hat{f}$, and (b) $\hat{V}$.

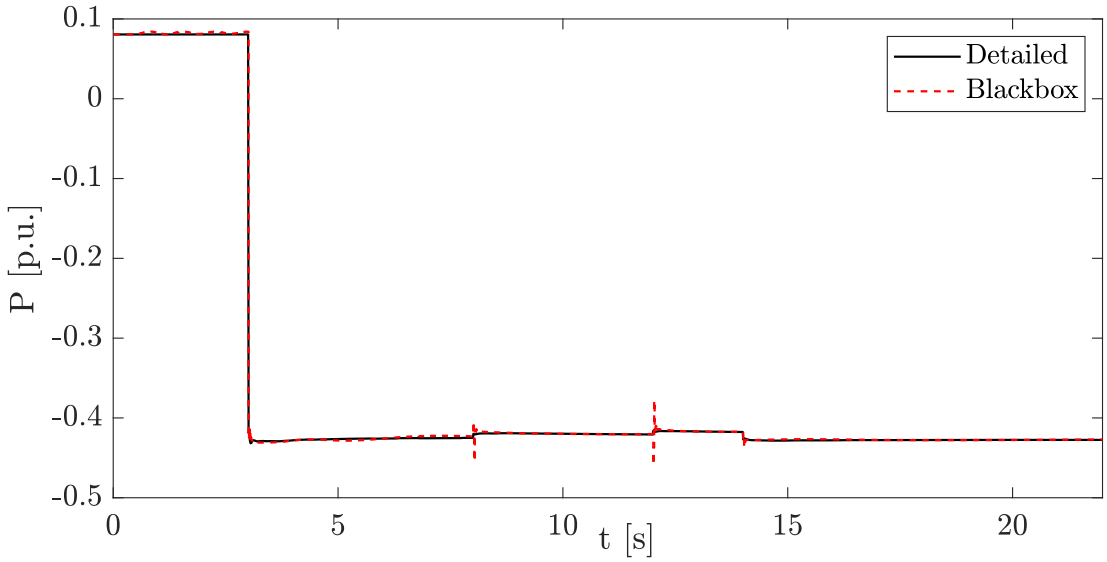

(a)

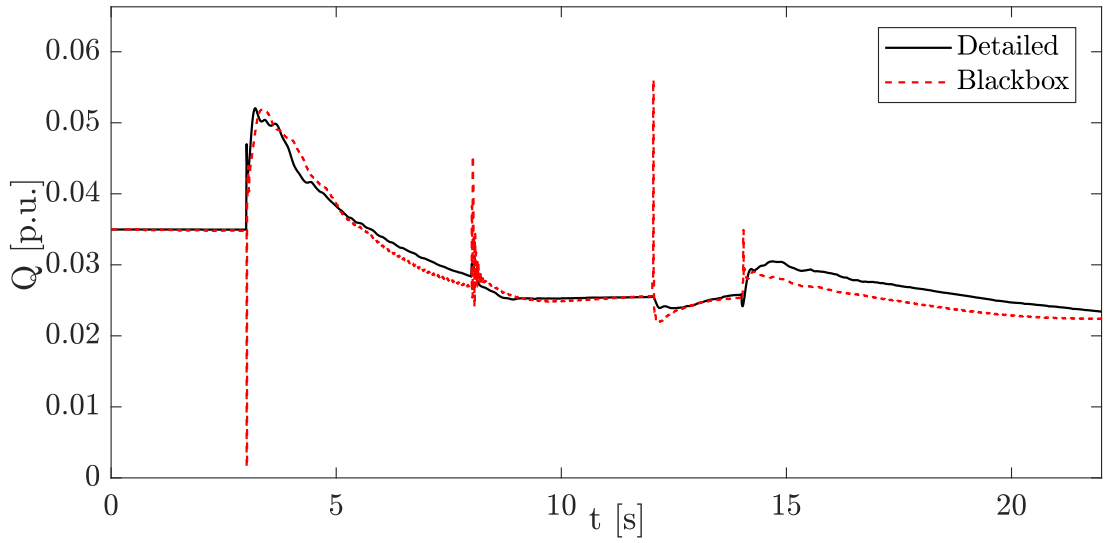

(b)

Figure 4.24: Aggregated BESS output for Case 7 (a) $\hat{P}$, (b) $\hat{Q}$.

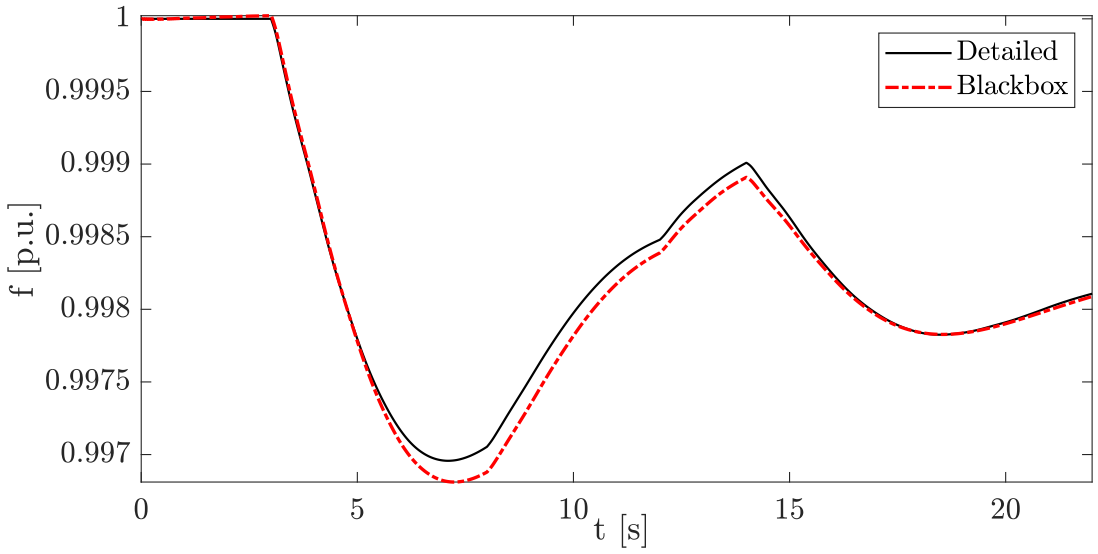

(a)

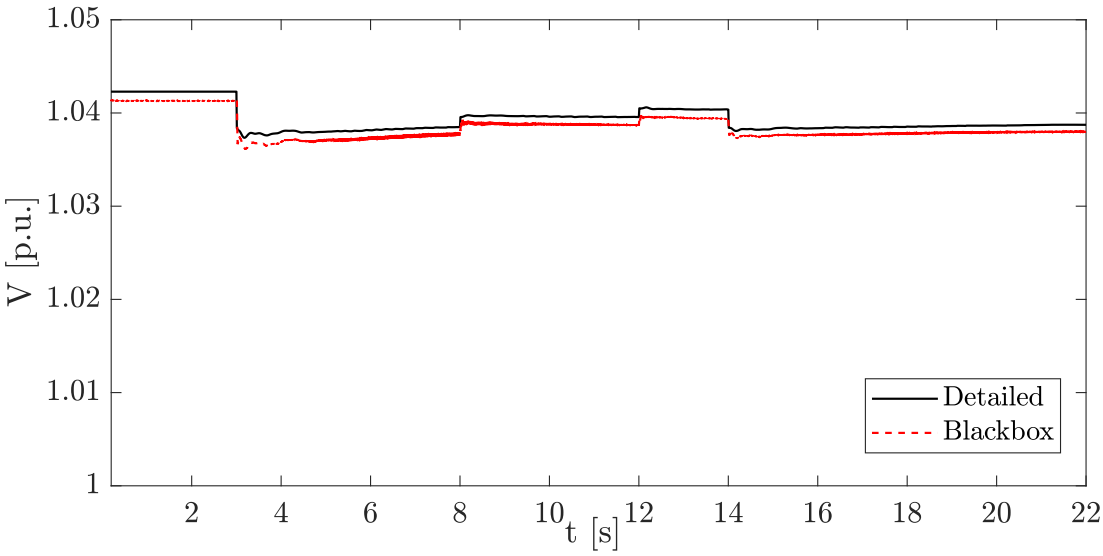

(b)

Figure 4.25: Aggregated BESS output for Case 7 (a) $\hat{f}$, and (b) $\hat{V}$.

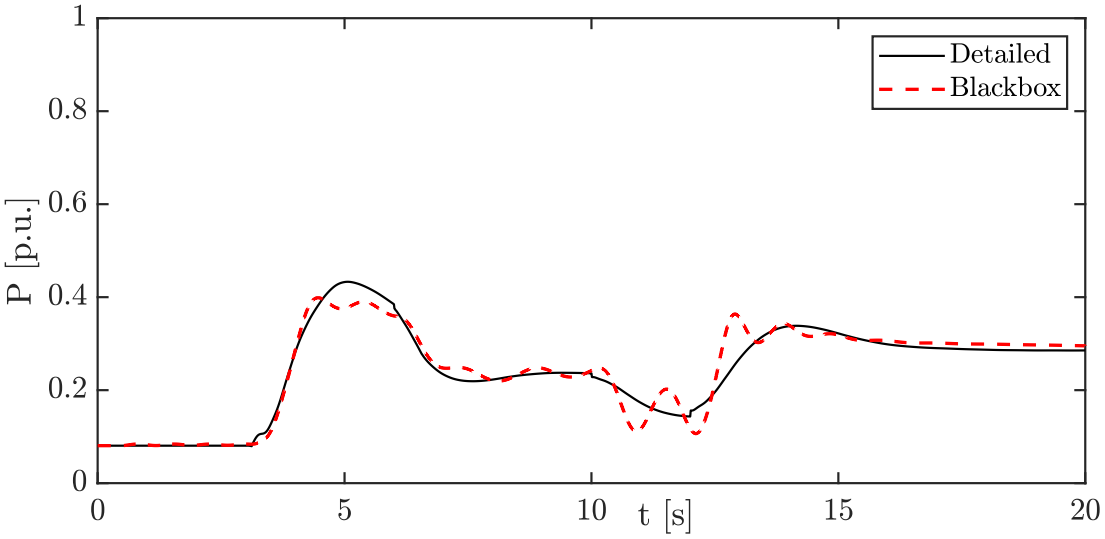

(a)

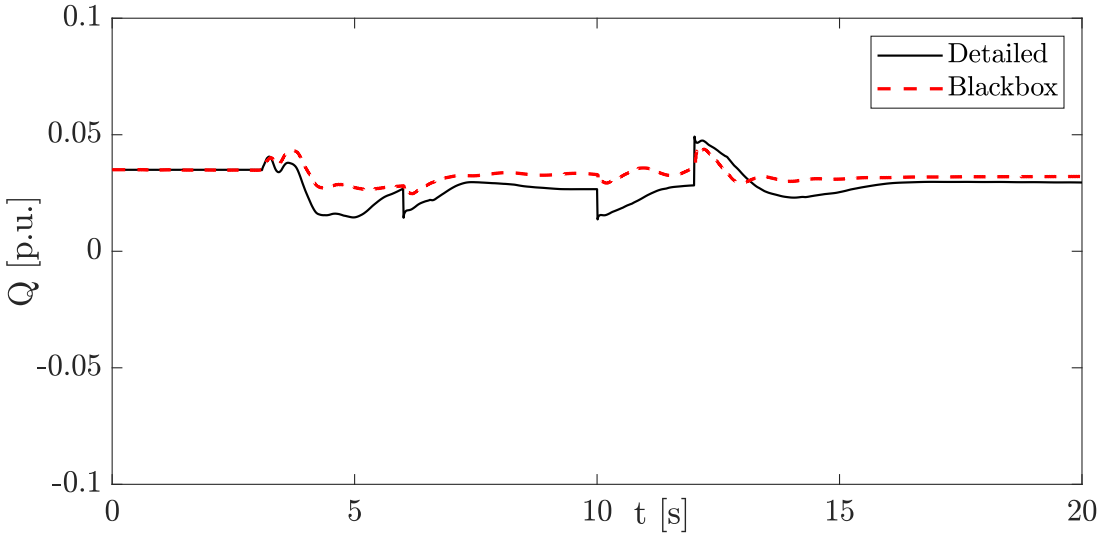

(b)

Figure 4.26: Aggregated BESS output for Case 8 (a) $\hat{P}$, (b) $\hat{Q}$.

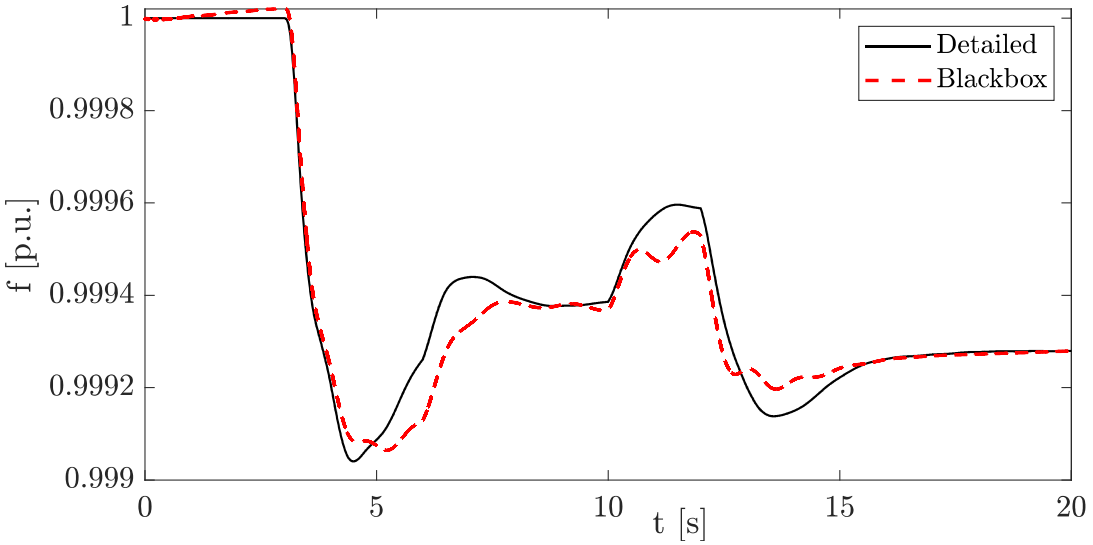

(a)

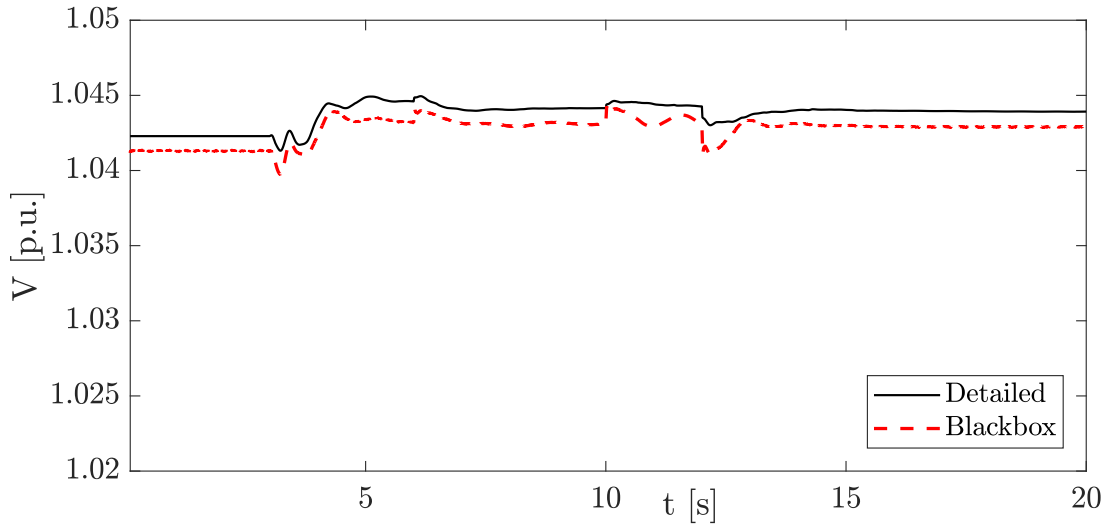

(b)

Figure 4.27: System performance in Case 8 (a) $\hat{f}$, and (b) $\hat{V}$.

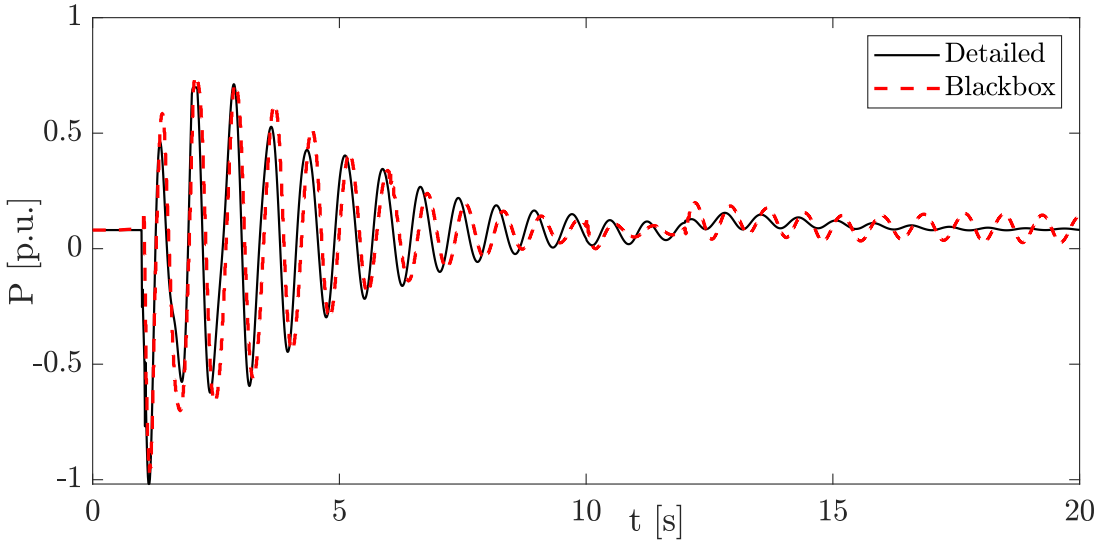

(a)

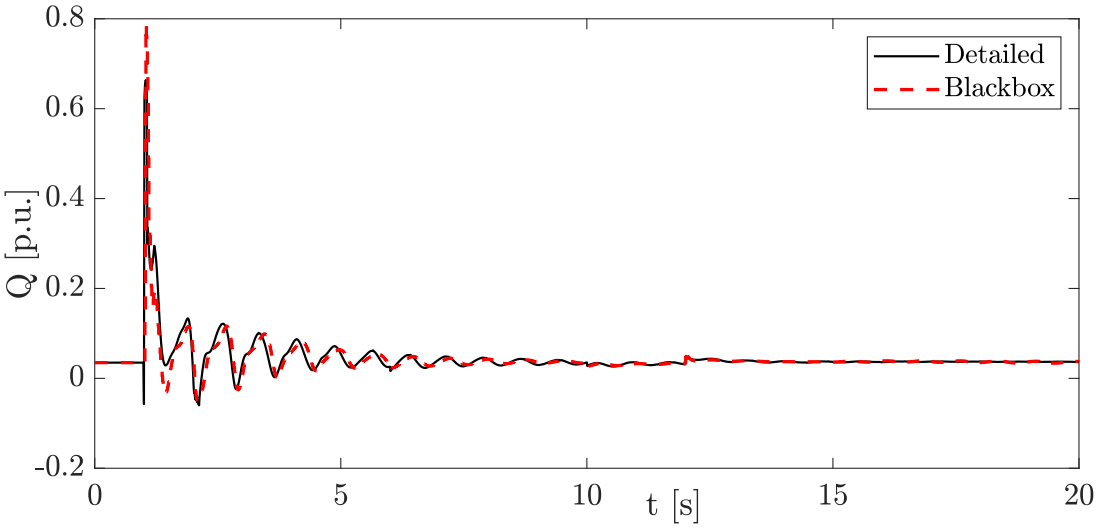

(b)

Figure 4.28: Aggregated BESS output for Case 9 (a) $\hat{P}$, (b) $\hat{Q}$.

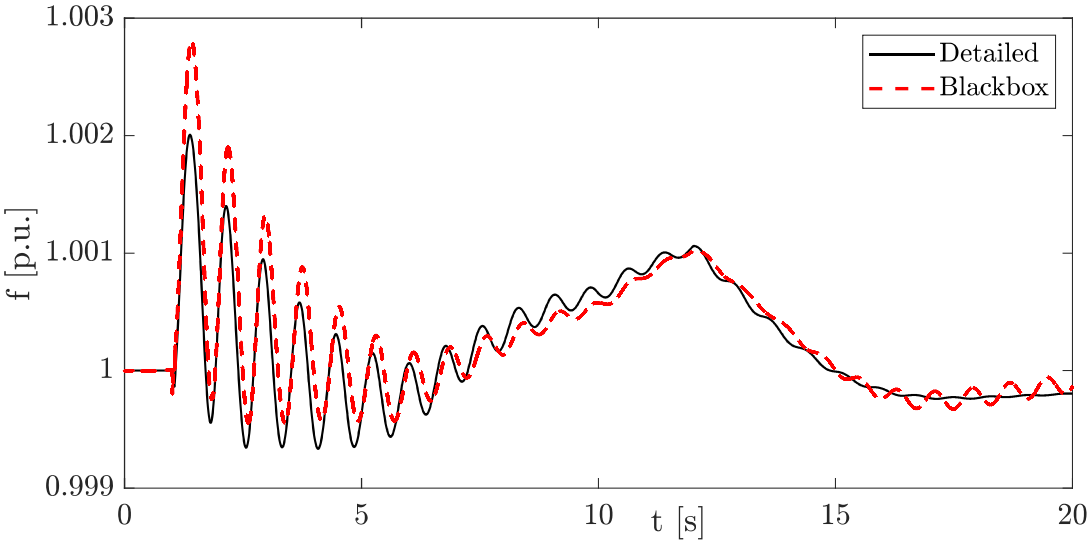

(a)

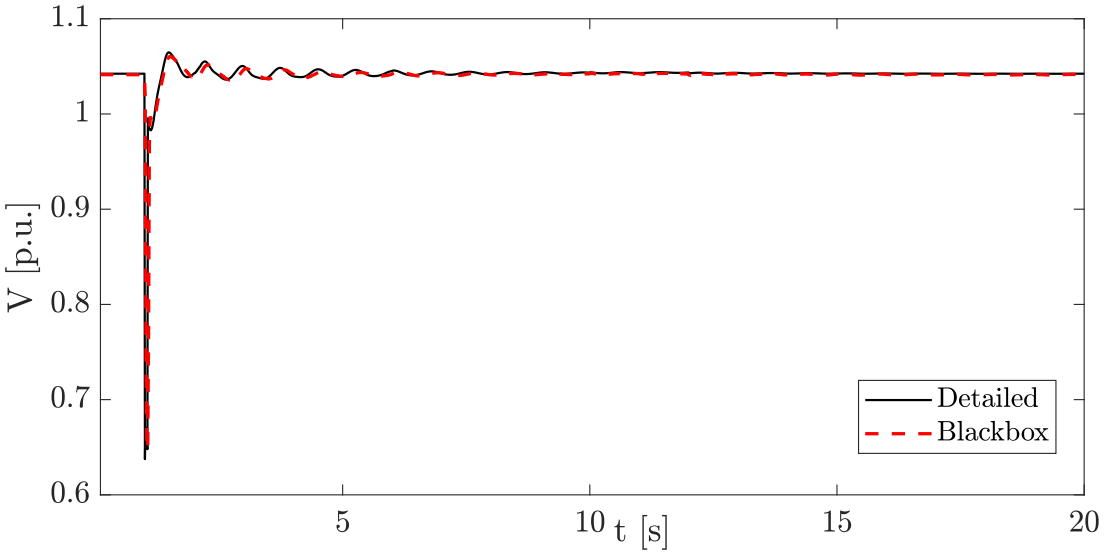

(b)

Figure 4.29: System performance in Case 9 (a) $\hat{f}$, and (b) $\hat{V}$.

4.3 Summary

In this Chapter, black-box models were proposed to represent the aggregated response of BESSs connected at the distribution level for contingencies at the transmission level. The models comprised two NNs, one for P and the other for Q, whose topologies were obtained using a GA-based approach to determine the optimal number of neurons in the hidden layers. The NNs were trained, validated, and tested with data for nine different transmission system contingencies using realistic benchmark test systems, demonstrating through simulations that the proposed models could accurately reproduce the results obtained from the previously proposed models with the BESSs providing different services, while considering PV solar generation and loads. The resulting black-box model was able to handle noise introduced in its input without compromising the accuracy of its output, and also represented events for which it was not trained. The model proposed can thus be readily applied by transmission system operators for studies where PV systems with storage capacity are massively deployed, or as a planning tool to estimate the effects of increasing penetration of distributed BESS on transmission systems.

Chapter 5

Conclusions

5.1 Summary and Conclusions

In this thesis, the impacts of grid-scale and distributed BESSs connected to ADNs, on the transmission grid were investigated. For this purpose, appropriate and novel BESS models and controls were proposed to facilitate the provision of grid services, such as frequency and voltage regulation, low-frequency oscillation damping, and active and reactive power injections. In addition, the development and validation of a dynamic a black-box model to represent the aggregated effect at the transmission level of distributed BESS in an ADN was presented. The proposed aggregated model facilitates studying the effects of ADNs on transmission system, by avoiding the need for detailed modeling of medium- and low-voltage systems for time-domain simulations.

In the first part of the thesis, the dynamic modelling of a BESS comprising multiple parallel VSCs and dc-to-dc converters per VSC, was addressed in detail. The battery bank associated with each dc-to-dc converter was modeled as a voltage source in series with a resistor, representing the internal voltage and resistance of a battery array forming the battery bank, which allows modeling degraded battery cells, characterized by larger resistance and lower internal voltages. An average model per-switching period of a bidirectional dc-to-dc converter has derived, which is the interface between the battery bank and the VSC. The average model of a VSC and the dynamics of a first-order filter complemented the BESS model. Then, a two-level hierarchical control strategy was proposed for the BESS. In the first level, or plant controller, frequency and voltage signals were used to calculate BESS' power reference values based on a particular mode of operation defined by a control flag, i.e., constant PQ, constant power factor, voltage regulation, frequency

regulation (PFR or SFR), POD, or simultaneous POD and frequency regulation. These reference values were then passed to the second level, where they were converted into current reference values, checked to prevent VSC overloading, and passed to a decoupled dq current controller, to control the effective P and Q injections, with the dc-to-dc converter controlling the dc-link voltage.

The proposed BESS model was validated against detailed EMT simulations for their equivalency, except during large transients when the EMT model tends to hit limits more often, thus affecting the control response. Thereafter, the impact of grid-scale BESSs on transmission systems was investigated, first by simulating several small-sized BESSs units connected at the load buses of a modified WSCC 9-bus test system, and then, as a single large-size BESS connected at a load bus of the same test system, as to provide different grid services in the presence of system disturbances, such as short circuits, generator trippings, and load changes. It was demonstrated that, in most cases, the proposed BESS controls were very effective in regulating the voltage and frequency, and damp low-frequency oscillations; however, when battery degradation was considered, the effectiveness of BESS to provide these services was considerably compromised because of the operation of the dc-to-dc converter controller, particularly for frequency regulation. It was shown that this behaviour was not captured by existing industry-grade BESS models in simulations, because of lack of representation of the dc-to-dc converter in these models.

In the second part of the thesis, a methodology was proposed to develop a black-box model that represents the aggregated effect of multiple ADN BESSs on the transmission grid. Two NARX NNs were used to represent the aggregated BESS P and Q injections at the boundary bus between the ADN and the transmission system, which were trained with measurements obtained at this bus. The inputs of the black-box model were the voltage and frequency at the boundary bus; a signal that can externally modify the power references (P_{ref} and Q_{ref}) of the individual BESS, controlled by a centralized entity at the ADN level; and a signal proportional to the solar irradiation to capture the behaviour of the PV generation embedded in the ADN, which directly affects the BESS operation. The optimal topologies of the NNs were obtained using GA, which seeks to minimize the NNs' prediction errors with respect to the actual measurements, i.e., the entry vector containing the number of neurons per layer. To test this methodology, detailed simulations were performed using a commercial-grade software for power system analysis, based on a test system comprise of multiple BESSs connected to a CIGRE benchmark ADN connected to a load bus of the 9-bus WSCC benchmark transmission network, from where the required measurements were obtained. It was demonstrated that the black-box model, with aggregated models of the loads and PV generation, were accurate enough to represent detailed simulations, not only for the same events from which the training data was obtained, but also for untrained

events.

The following conclusions can be drawn from the presented work:

- The additional controls proposed in this thesis for BESS, which are not considered in existing models, such as the WECC model, namely, SFR control and OD, can significantly improve the contribution of a grid-scale BESS to the stability of the transmission grid, with fewer control logic flags and regulation paths than existing model controls.
- The inclusion of the dynamics of the dc-to-dc converter and decoupled dq current control in the BESS model is shown to be important, especially when degradation of the battery cells are considered. However, modeling this requires a much smaller integration step depending on the software used, which also increases the simulation times.
- The proposed black-box model can accurately reproduce the results obtained from detailed models, with the BESSs providing different services, while considering PV solar generation and loads.
- The obtained black-box models are robust, as they are able to handle white noise in their inputs without compromising the accuracy of their outputs, and are also able to represent events for which they were not trained. The model proposed in this thesis can thus be readily applied by transmission system operators for studies where PV systems with storage capacity are massively deployed, or as a planning tool to estimate the effects on transmission systems of increasing penetration of distributed PV generation and BESS at distribution systems.

5.2 Contributions

The main contributions of this thesis can be summarized as follows:

- Propose and validate a novel average BESS model for transmission system dynamic studies, which integrates the battery banks and dc-to-dc converter and its controls at the dc side of the VSC. This model can be parametrized to simulate new or existing BESS facilities, considering the degradation of the battery cells.

- Demonstrate the relevance of modelling the dc side of a bulk BESS facility connected to a transmission system, especially for applications such as frequency regulation, voltage control, and transient stability, showing specifically the effects of degradation of the battery cells and limits in the dc-to-dc converter controller on the dynamic response of the BESS.

- Assess the effectiveness of proposed oscillation damping, secondary frequency regulation, and voltage regulation controllers, and evaluate the contributions of a large BESS to the stability of a transmission system.

- Integrate the proposed parametrizable novel model of the BESSs in a commercial-grade software package used for dynamic analysis of power systems, demonstrating its advantages over existing and well-accepted models in the presence of contingencies.

- Propose and demonstrate a methodology to develop a NN-based black-box model that accurately reproduces the aggregated behaviour of distributed BESSs providing different grid services, namely, frequency regulation, oscillation damping, constant power injections, and voltage regulation. The proposed methodology optimizes the topology of a black-box model based on GA, while considering the NN's training times and the black-box model's sensitivity to small variations, using white noise in its inputs to improve the model robustness.

- Study and illustrate the impact of distributed BESSs on a benchmark transmission system, for different grid contingencies, based on a benchmark ADN.

The results discussed in Chapters 3 have been published in [75] and [76], while the results in Chapter 4 have been submitted for publication in [77].

5.3 Future Work

Future research may be carried out to address the following issues:

- Incorporate the effect of SoC on the battery internal voltage, by using more detailed models, such as those depicted in Figure 2.3.

- Apply the proposed BESS model for studies in a large power systems, such as the Ontario's power system, to study the potential of a large BESS facility to improve grid real operations.

- Apply the proposed methodology to develop a black-box model based on actual measurements from an actual ADN.

References

[1] M. T. Lawder, B. Suthar, P. W. C. Northrop, S. De, C. M. Hoff, O. Leitermann, M. L. Crow, S. Santhanagopalan, and V. R. Subramanian, "Battery energy storage system (BESS) and battery management system (BMS) for grid-scale applications," *Proceedings of the IEEE*, vol. 102, no. 6, pp. 1014–1030, 2014.

[2] X. Luo, J. Wang, M. Dooner, and J. Clarke, "Overview of current development in electrical energy storage technologies and the application potential in power system operation," *Applied Energy*, vol. 137, pp. 511–536, 2015.

[3] N. Hatziargyriou, T. Van Cutsem, J. Milanović, P. Pourbeik, C. Vournas, O. Vlachokyriakou, P. Kotsampopoulos, Hong, R. Ramos, J. Boemer, P. Aristidou, V. Singhvi, J. dos Santos, and L. Colombari, "Contribution to bulk system control and stability by distributed energy resources connected at distribution network," Technical report PES-TR22, IEEE PES Power System Dynamic Performance Committee, January 2017.

[4] "Innovation landscape brief: Utility-scale batteries," Technical report, International Renewable Energy Agency (IRENA), Abu Dubai, 2019. [Online]. Available: https://www.irena.org/-/media/Files/IRENA/Agency/Publication/2019/Sep/IRENA_Utility-scale-batteries_2019.pdf

[5] H. Golpîra, H. Seifi, and M. R. Haghifam, "Dynamic equivalencing of an active distribution network for large-scale power system frequency stability studies," *IET Generation, Transmission & Distribution*, vol. 9, no. 15, pp. 2245–2254, 2015.

[6] J. V. Milanović and S. M. Zali, "Validation of equivalent dynamic model of active distribution network cell," *IEEE Transactions on Power Systems*, vol. 28, no. 3, pp. 2101–2110, 2013.

[7] Y. Zhang, S. Lyden, B. L. de la Barra, and M. Haque, "A genetic algorithm approach to parameter estimation for PV modules," in *IEEE PES General Meeting*, Boston, MA, July 2016, pp. 1–5.

[8] J. Matevosyan, S. M. Villanueva, S. Djokic, J. Acosta, S. M. Zali, F. Resende, and J. Milanovic, "Aggregated models of wind-based generation and active distribution network cells for power system studies-literature overview," in *IEEE PowerTech*, Trondheim, Norway, June 2011, pp. 1–8.

[9] P. Kundur, N. Balu, and M. Lauby, *Power system stability and control*. NY: McGraw-hill, 1994.

[10] A. Gomez-Exposito, A. J. Conejo, and C. Canizares, *Electric energy systems: analysis and operation*. Boca Raton, FL, USA: CRC Press, 2016.

[11] W. Du, H. Wang, L. Xiao, and R. Dunn, "Modeling energy storage systems into electric power transmission systems," in *44th IEEE International Universities Power Engineering Conference (UPEC)*, Glasgow, United Kingdom, September 2009, pp. 1–5.

[12] A. Kanchanaharuthai, V. Chankong, and K. A. Loparo, "Transient stability and voltage regulation in multimachine power systems Vis-Vis STATCOM and battery energy storage," *IEEE Transactions on Power Systems*, vol. 30, no. 5, pp. 2404–2416, 2015.

[13] Ortega and F. Milano, "Generalized model of VSC-based energy storage systems for transient stability analysis," *IEEE Transactions on Power Systems*, vol. 31, no. 5, pp. 3369–3380, 2016.

[14] D. Bazargan, S. Filizadeh, and A. M. Gole, "Stability analysis of converter-connected battery energy storage systems in the grid," *IEEE Transactions on Sustainable Energy*, vol. 5, no. 4, pp. 1204–1212, 2014.

[15] P. Pourbeik, S. E. Williams, J. Weber, J. Sanchez-Gasca, J. Senthil, S. Huang, and K. Bolton, "Modeling and dynamic behavior of battery energy storage: A simple model for large-scale time-domain stability studies," *IEEE Electrification Magazine*, vol. 3, no. 3, pp. 47–51, 2015.

[16] R. T. Elliott, A. Ellis, P. Pourbeik, J. J. Sanchez-Gasca, J. Senthil, and J. Weber, "Generic photovoltaic system models for WECC - a status report," in *IEEE PES General Meeting*, Denver, CO, July 2015, pp. 1–5.

[17] "WECC battery storage dynamic modeling guideline," Technical report, WECC, Modeling and Validation Work Group, pp. 1–38, 2016.

[18] X. Xu, M. Bishop, D. G. Oikarinen, and C. Hao, "Application and modeling of battery energy storage in power systems," *CSEE Power and Energy Syst.*, vol. 2, no. 3, pp. 82–90, 2016.

[19] T. Xia, M. Li, P. Zi, L. Tian, X. Qin, and N. An, "Modeling and simulation of battery energy storage system (BESS) used in power system," in *5th International Conference on Electric Utility Deregulation and Restructuring and Power Technologies (DRPT)*, Changsha, China, November 2015, pp. 2120–2125.

[20] P. Pourbeik, "Proposal for new features for the renewable energy system generic models," Technical report, WECC.

[21] U. Datta, A. Kalam, and J. Shi, "Battery energy storage system to stabilize transient voltage and frequency and enhance power export capability," *IEEE Transactions on Power Systems*, vol. 34, no. 3, pp. 1845–1857, 2019.

[22] D. Bazargan, B. Bahrani, and S. Filizadeh, "Reduced capacitance battery storage dc-link voltage regulation and dynamic improvement using a feedforward control strategy," *IEEE Transactions on Energy Conversion*, vol. 33, no. 4, pp. 1659–1668, 2018.

[23] M. Farrokhabadi, S. König, C. A. Cañizares, K. Bhattacharya, and T. Leibfried, "Battery energy storage system models for microgrid stability analysis and dynamic simulation," *IEEE Transactions on Power Systems*, vol. 33, no. 2, pp. 2301–2312, 2018.

[24] D. Kottick, M. Blau, and D. Edelstein, "Battery energy storage for frequency regulation in an island power system," *IEEE Transactions on Energy Conversion*, vol. 8, no. 3, pp. 455–459, 1993.

[25] H. Pia, S. Chen, H. Lv, and H. Liu, "Control strategy of battery energy storage system to participate in the second frequency regulation," in *International Symposium on Smart Electric Distribution Systems and Technologies (EDST)*, Vienna, Austria, September 2015, pp. 53–57.

[26] L. Liang, J. Zhong, and Z. Jiao, "Frequency regulation for a power system with wind power and battery energy storage," in *IEEE International Conference on Power System Technology (POWERCON)*, Auckland, New Zealand, November 2012, pp. 1–6.

[27] C. Mosca, F. Arrigo, A. Mazza, E. Bompard, E. Carpaneto, G. Chicco, and P. Cuccia, "Mitigation of frequency stability issues in low inertia power systems using synchronous compensators and battery energy storage systems," *IET Generation, Transmission, and Distribution*, vol. 13, no. 17, pp. 3951–3959, 2019.

[28] W. Du, Z. Chen, H. F. Wang, and R. Dunn, "Energy storage systems applied in power system stability control," in *42nd International Universities Power Engineering Conference*, Brighton, UK, September 2007, pp. 455–458.

[29] C. F. Lu, C. C. Liu, and C. J. Wu, "Dynamic modelling of battery energy storage system and application to power system stability," *IEE Proceedings - Generation, Transmission and Distribution*, vol. 142, no. 4, pp. 429–435, 1995.

[30] M. Chen and G. A. Rincon-Mora, "Accurate electrical battery model capable of predicting runtime and I-V performance," *IEEE Transactions on Energy Conversion*, vol. 21, no. 2, pp. 504–511, 2006.

[31] P. Pourbeik and J. K. Petter, "Modeling and validation of battery energy storage systems using simple generic models for power system stability studies," *Cigre Science & Engineering,(9)*, 2017.

[32] D. Bazargan, "A study of battery energy storage dynamics in power systems," Ph.D. thesis, University of Manitoba, 2014.

[33] J. H. Chow, R. Galarza, P. Accari, and W. W. Price, "Inertial and slow coherency aggregation algorithms for power system dynamic model reduction," *IEEE Transactions on Power Systems*, vol. 10, no. 2, pp. 680–685, 1995.

[34] T. Y. J. Lem and R. T. H. Alden, "Comparison of experimental and aggregate induction motor responses," *IEEE Transactions on Power Systems*, vol. 9, no. 4, pp. 1895–1900, 1994.

[35] P. Jazayeri, W. Rosehart, and D. T. Westwick, "A multistage algorithm for identification of nonlinear aggregate power system loads," *IEEE Transactions on Power Systems*, vol. 22, no. 3, pp. 1072–1079, 2007.

[36] S. M. Zali and J. V. Milanović, "Generic model of active distribution network for large power system stability studies," *IEEE Transactions on Power Systems*, vol. 28, no. 3, pp. 3126–3133, 2013.

[37] X. Feng, Z. Lubosny, and J. W. Bialek, "Identification based dynamic equivalencing," in *IEEE Lausanne Power Tech*, Lausanne, Switzerland, July 2007, pp. 267–272.

[38] M. K. Donnelly, J. E. Dagle, D. J. Trudnowski, and G. J. Rogers, "Impacts of the distributed utility on transmission system stability," *IEEE Transactions on Power Systems*, vol. 11, no. 2, pp. 741–746, 1996.

[39] G. J. Vachtsevanos and K. C. Kalaitzakis, "A methodology for dynamic utility interactive operation of dispersed storage and generation devices," *IEEE Transactions on Power Systems*, vol. 7, no. 1, pp. 45–51, 1987.

[40] A. K. Srivastava, A. A. Kumar, and N. N. Schulz, "Impact of distributed generations with energy storage devices on the electric grid," *IEEE Systems Journal*, vol. 6, no. 1, pp. 110–117, March 2012.

[41] A. M. Azmy and I. Erlich, "Identification of dynamic equivalents for distribution power networks using recurrent ANNs," in *IEEE PES Power Systems Conference and Exposition.*, New York, NY, October 2004, pp. vol 1. 348–353.

[42] C. Han, D. Changhong, and Li Dalu, "Recurrent neural network-based dynamic equivalencing in power system," in *IEEE International Conference on Control and Automation*, Guangzhou, China, May 2007, pp. 2396–2399.

[43] "IESO Report: Energy Storage," Technical report, Independent Electricity System Operator - IESO, March 2016. [Online]. Available: http://www.ieso.ca/-/media/files/ieso/document-library/energy-storage/ieso-energy-storage-report_march-2016.pdf

[44] V. A. Boicea, "Energy storage technologies: The past and the present," *Proceedings of the IEEE*, vol. 102, no. 11, pp. 1777–1794, 2014.

[45] A. R. Sparacino, G. F. Reed, R. J. Kerestes, B. M. Grainger, and Z. T. Smith, "Survey of battery energy storage systems and modeling techniques," in *Proceedings of the IEEE PES General Meeting*, San Diego, CA, July 2012, pp. 1–8.

[46] G. Saldaña, J. I. San Martín, I. Zamora, F. J. Asensio, and O. Oñederra, "Analysis of the current electric battery models for electric vehicle simulation," *Energies*, vol. 12, no. 14, p. 2750, 2019.

[47] I. Serban and C. Marinescu, "Control strategy of three-phase battery energy storage systems for frequency support in microgrids and with uninterrupted supply of local loads," *IEEE Transactions on Power Electronics*, vol. 29, no. 9, pp. 5010–5020, 2014.

[48] S. Vazquez, S. M. Lukic, E. Galvan, L. G. Franquelo, and J. M. Carrasco, "Energy storage systems for transport and grid applications," *IEEE Transactions on Industrial Electronics*, vol. 57, no. 12, pp. 3881–3895, 2010.

[49] N. Mohan, T. M. Undeland, and W. P. Robbins, *Power electronics: converters, applications, and design*. John wiley & sons, 2003.

[50] M. Restrepo, C. A. Cañizares, and M. Kazerani, "Three-stage distribution feeder control considering four-quadrant ev chargers," *IEEE Transactions on Smart Grid*, vol. 9, no. 4, pp. 3736–3747, 2018.

[51] F. O. Karray and C. W. De Silva, *Soft computing and intelligent systems design: theory, tools, and applications*. Pearson Education, 2004.

[52] Z. Boussaada, O. Curea, A. Remaci, H. Camblong, and N. Mrabet Bellaaj, "A nonlinear autoregressive exogenous (NARX) neural network model for the prediction of the daily direct solar radiation," *Energies*, vol. 11, no. 3, pp. 1–21, 2018.

[53] P. Kundur, J. Paserba, V. Ajjarapu, G. Andersson, A. Bose, C. Canizares, N. Hatziargyriou, D. Hill, A. Stankovic, C. Taylor, T. Van Cutsem, and V. Vittal, "Definition and classification of power system stability ieee/cigre joint task force on stability terms and definitions," *IEEE Transactions on Power Systems*, vol. 19, no. 3, pp. 1387–1401.

[54] S. Bacha, I. Munteanu, A. I. Bratcu *et al.*, *Power electronic converters modeling and control*. Springer, 2014.

[55] M. Restrepo, J. Morris, M. Kazerani, and C. A. Cañizares, "Modeling and testing of a bidirectional smart charger for distribution system EV integration," *IEEE Trans. Smart Grid*, vol. 9, no. 1, pp. 152–162, 2018.

[56] M. Kazerani, "ECE 663 lecture 6: Non-isolated dc/dc converter topologies and control techniques," University of Waterloo, Spring, 2015.

[57] A. Yazdani and R. Iravani, *Voltage-sourced converters in power systems: modeling, control, and applications*. John Wiley & Sons, 2010.

[58] B. Gao, C. Xia, N. Chen, K. M. Cheema, L. Yang, and C. Li, "Virtual synchronous generator based auxiliary damping control design for the power system with renewable generation," *Energies*, vol. 10, no. 8, p. 1146, 2017.

[59] Y. Yang, L. Hadjidemetriou, F. Blaabjerg, and E. Kyriakides, "Benchmarking of phase locked loop based synchronization techniques for grid-connected inverter systems," in *9th International Conference on Power Electronics and ECCE Asia (ICPE-ECCE Asia)*, Seoul, South Korea, July 2015, pp. 2167–2174.

[60] "TSAT transient security assessment tool model manual," Powertech Labs In., 2018. [Online]. Available: https://www.powertechlabs.com/

[61] P. M. Anderson and A. A. Fouad, *Power system control and stability*. John Wiley & Sons, 2008.

[62] "Wind energy RD park and storage system for innovation in grid integration," The Wind Energy Institute of Canada (WEICAN), 2020. [Online]. Available: https://www.nrcan.gc.ca/science-and-data/funding-partnerships/funding-opportunities/current-investments/wind-energy-rd-park-and-storage-system-innovation-grid-integration/4979

[63] C. Patsios, B. Wu, E. Chatzinikolaou, D. J. Rogers, N. Wade, N. P. Brandon, and P. Taylor, "An integrated approach for the analysis and control of grid connected energy storage systems," *Journal of Energy Storage*, vol. 5, pp. 48–61, 2016.

[64] T. Hiyama, "Rule-based stabilizer for multi-machine power system," *IEEE Trans. Power Systems*, vol. 5, no. 2, pp. 403–411, 1990.

[65] A. R. Borden and B. C. Lesieutre, "Variable projection method for power system modal identification," *IEEE Transactions on Power Systems*, vol. 29, no. 6, pp. 2613–2620, 2014.

[66] "Control System Toolbox Release Notes," Matlab, 2020. [Online]. Available: https://www.mathworks.com/help/control

[67] "California energy commission - tracking progress, energy storage," California Energy Commission, Aug. Tech. Report, 2018. [Online]. Available: https://www.energy.ca.gov/sites/default/files/2019-12/energy_storage_ada.pdf

[68] "Q3/Q4 2019: Solar industry update," National Renewable Energy Laboratory (NREL), Feb. Tech. Report, NREL/PR-6A20-76158, 2020.

[69] M. S. H. Lipu, M. A. Hannan, A. Hussain, M. H. Saad, A. Ayob, and F. Blaabjerg, "State of charge estimation for lithium-ion battery using recurrent NARX neural network model based lighting search algorithm," *IEEE access*, vol. 6, pp. 28 150–28 161, 2018.

[70] "Design time series NARX feedback neural networks," MathWorks, 2020. [Online]. Available: https://www.mathworks.com/help/deeplearning/ug/design-time-series-narx-feedback-neural-networks.html

[71] I. Goodfellow, Y. Bengio, and A. Courville, *Deep learning*. MIT press, 2016.

[72] Strunz et al., "Benchmark systems for network integration of renewable and distributed energy resources," Tech. report, Cigre Task Force C, Apr. 2014.

[73] S. McNally, "Distribution system voltage and power quality," Tech. guideline No. ECG0008, HydroOttawa, Mar. 2016.

[74] "Simscape model and simulate multidomain physical systems," MathWorks, 2020. [Online]. Available: https://www.https://www.mathworks.com/products/simscape.html

[75] F. Calero, C. A. Cañizares, and K. Bhattacharya, "Detailed and average battery energy storage model comparison," in *IEEE PES Innovative Smart Grid Technol. Europe (ISGT-Europe)*, Bucharest, Romania, Nov. 2019, pp. 1–5.

[76] F. Calero, C. A. Cañizares, and K. Bhattacharya, "Dynamic modeling of battery energy storage and applications in transmission systems," *IEEE Transaction on Smart Grid*, August 2020, 10 pages.

[77] ——, "Aggregated bess dynamic models for active distribution network studies," *IEEE Transaction on Smart Grid*, submitted May 2020, revised and resubmitted September 2020, 12 pages.